The kinematic signature of the Galactic warp in the Gaia era

ELOISA POGGIO

UNIVERSITÀ DEGLI STUDI DI TORINO
Scuola di Dottorato in Scienza ed Alta Tecnologia
Indirizzo di Fisica e Astrofisica

Supervisor: Dr. Alessandro Spagna (INAF-OATo)
Co-supervisors: Dr. Ronald Drimmel and Dr. Richard L. Smart (INAF-OATo)

26 - 10 - 2018

Abstract

In the *Gaia* era, the scientific community have had access for the first time to high-precision astrometric measurements of billions of stars. In the coming years, *Gaia* will presumably make a fundamental contribution to numerous open questions on the evolution of our Galaxy. We here focus on the long-standing debate on the origin and dynamical nature of the warp of our Galaxy, with particular attention to the warp-induced motions in stellar kinematics. In this Thesis, we present a kinematic study of the Galactic disc, aimed at detecting the kinematic signature of the Galactic warp. We first analyze a sample of OB stars in the *Hipparcos* subset in the first *Gaia* data release (*Gaia* DR1, Gaia Collaboration et al., 2016), and we find that their kinematics do not follow the trends expected from a long-lived stable warp (Poggio et al., 2017). Hence, these findings point to alternative scenarios, such as more sophisticated warp models and/or kinematic perturbations overwhelming the warp signature (Poggio et al., 2018b). To better understand the results obtained with *Hipparcos* OB stars in *Gaia* DR1, we consider a larger and fainter sample of OB stars from the TGAS catalogue in *Gaia* DR1, selected via a probabilistic approach. We apply statistical inference to the obtained dataset, modeling the warp as a precessing feature. From the obtained results, we conclude that our simple model doesn't appropriately describe the observed kinematic trends, and argue that the data contain additional kinematic perturbations, which are not included in our simple model. Alternatively, the precessing warp model might be not appropriate, as the warp might be a transient feature. The results obtained with *Gaia* DR1 are further confirmed by a sample of OB stars from the second *Gaia* data release (*Gaia* DR2, Gaia Collaboration et al., 2018a) within 3 kpc from the Sun, whose vertical vertical velocities do not present any evidence of warp signature (Gaia Collaboration et al., 2018b). In contrast, giant stars exhibit a mild gradient in vertical velocities with increasing Galactic radius, as expected from a warp signature (Gaia Collaboration et al., 2018b). We reconcile the discrepancy found in the two stellar populations by sampling over a larger volume of the Galactic disc (up to 7 kpc from the Sun), detecting in both samples the large-scale kinematic signature of the warp, apparent as an increase of 5-6 km/s in the vertical velocities from 8 to 14 kpc in Galactic radius (Poggio et al., 2018a). Considering that the warp generation mechanism must be common to both dynamically young and old stellar populations, we argue that the warp is principally a gravitational phenomenon, thus placing an important constraint on the possible formation scenario. Further analysis and modeling of the *Gaia* DR2 data will certainly reveal further details of the dynamical nature of the Galactic warp.

Sommario

Nell'era di *Gaia*, la comunità scientifica ha avuto accesso per la prima volta a misure di alta precisione astrometrica per miliardi di stelle. Presumibilmente, negli anni a venire, *Gaia* darà un importante contributo a molte questioni aperte sull'evoluzione della Via Lattea. Si volge qui l'attenzione sulla dibattuta origine e natura dinamica del warp presente nella nostra Galassia e, in particolare, sugli andamenti cinematici ad esso legati. In questa Tesi, viene presentato uno studio cinematico del disco Galattico, finalizzato a rilevare la traccia cinematica del warp. In primo luogo, si analizza la cinematica delle stelle OB nel sotto-campione *Hipparcos* della prima release dei dati di *Gaia* (*Gaia* DR1, Gaia Collaboration et al., 2016); si ottiene, come risultato, che la loro cinematica non segue gli andamenti di un warp statico (Poggio et al., 2017). Tali risultati, pertanto, fanno supporre scenari alternativi, come modelli di warp più sofisticati e/o perturbazioni cinematiche che sovrastano la traccia del warp (Poggio et al., 2018b). Per comprendere meglio i risultati ottenuti con le stelle OB di *Hipparcos* in *Gaia* DR1, si considera un campione più ampio e più debole di stelle OB nel catalogo TGAS in *Gaia* DR1, selezionato tramite un approccio probabilistico. Si studia la cinematica del warp con un'inferenza di tipo statistico, basata su un modello di warp in precessione. Dai risultati ottenuti, si deduce che il nostro modello non riproduce adeguatamente la cinematica delle stelle OB in TGAS; ciò può essere spiegato assumendo che i dati contengano ulteriori perturbazioni cinematiche non incluse nel nostro modello, o, alternativamente, che il warp sia una struttura instabile. I risultati ottenuti con la *Gaia* DR1 vengono ulteriormente confermati dalle velocità verticali di un campione di stelle OB nella seconda *Gaia* data release (*Gaia* DR2, Gaia Collaboration et al., 2018a), la cui cinematica, entro 3 kpc dal Sole, non presenta alcuna evidenza di traccia del warp (Gaia Collaboration et al., 2018b). Al contrario, le stelle giganti nella *Gaia* DR2 mostrano un lieve gradiente nelle velocità verticali al crescere del raggio galattico, come previsto dalla traccia cinematica del warp (Gaia Collaboration et al., 2018b). La discrepanza riscontrata nelle due popolazioni stellari viene superata campionando un volume maggiore del disco galattico (fino a 7 kpc dal Sole); si rileva in entrambi i campioni la traccia cinematica su larga scala del warp, che si manifesta come un aumento di 5-6 km/s nelle velocità verticali da 8 a 14 kpc in raggio Galattico (Poggio et al., 2018a). La presenza del segnale cinematico nei due campioni indica che il meccanismo di generazione del warp deve essere comune sia alle popolazioni stellari dinamicamente giovani sia a quelle vecchie; pertanto, si interpreta il warp come un fenomeno di natura prevalentemente gravitazionale, ponendo così un importante vincolo sul possibile scenario di formazione. Ulteriori analisi e modelli dei dati di *Gaia* DR2 riveleranno sicuramente ulteriori dettagli sulla natura dinamica del warp Galattico.

TABLE OF CONTENTS

Page

Part I

Introduction

CHAPTER 1

THE WARPED MILKY WAY

Since time immemorial our ancestors have been observing our home Galaxy as a stream of diffuse white light in the night sky. Due to its appearance, this band of light was designated in the Greek world as *galaxías kýklos* (milky circle), and in Latin *via lactea*, that we translate as *Milky Way* or simply the *Galaxy*. Speculations on the nature of the Milky Way date back to the Greek philosophers like Democritus, who already described it as a vast collection of stars. Actual proof had to wait until the invention of the Dutch telescope, and Galileo Galilei improving its magnifying power in 1610. By pointing his telescope to the Milky Way, he realized that it was constituted of myriads of faint stars, impossible to be distinguished by the naked eye. The first attempt to describe the shape of the Milky Way and the position of the Sun within it was carried out by William Herschel in 1785, by counting the number of stars in different regions of the sky. He produced a diagram (shown in Figure 1.1) of the shape of the Milky Way, with the Solar System close to the center. The picture suggested by Herschel evolved dramatically in the following centuries, due to the improvement of technical instrumentation and to important discoveries by various scientists. A considerable contribution was given by Harlow Shapley, after his studies on the distribution of the globular clusters around 1915. Originally assuming a Solar-centered Galaxy, he expected to observe a uniform distribution of globular clusters throughout the sky, but found an overdensity toward the constellation of the Sagittarius. He therefore identified that point as the direction to the center of the Galaxy. He also suggested that the so-called spiral nebulae (a term used to describe galaxies with a visible spiral structure, before it was understood that these objects were external galaxies) were part of the Galaxy; subsequently, our Milky Way was thought to contain all the stars in the Universe. In the same years, Heber Curtis supported a different scenario, based on his observations; while studying a sample of novae (bright stellar sources that appear for a short while before fading away) within

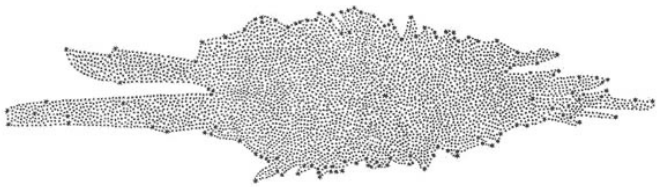

Figure 1.1: The shape of our Galaxy as deduced from star counts by William Herschel in 1785; the solar system was assumed near center. (Source: "Section of our sidereal system." Herschel, William. "On the Construction of the Heavens. By William Herschel, Esq. FRS." Philosophical Transactions of the Royal Society of London 75 (1785). Note: The image shown is flipped 180 degrees on the horizontal axis from the original, as first published in the Philosophical Transactions of the Royal Society in 1785; the bifurcated arms of the illustration should be on the left.).

the Great Nebula Andromeda (M31, today known as the Andromeda Galaxy), he noticed that these novae were, on average, very much fainter than those seen within the Milky Way. Hence, he deduced that they were much further away, and argued that the spiral nebulae were extragalactic objects. The disagreement between Shapley and Curtis led to the famous Great Debate in 1920. A few years later, observations from Edwin Hubble finally solved this dilemma. From the 100" Hooker telescope at Mount Wilson, he measured the distance to the Andromeda nebula using the period-luminosity relation for Cepheids stars, now called the Leavitt Law; the obtained distance, calculated to be around 300 kpc (Hubble 1929), was far too large for the Andromeda nebula to be part of the Milky Way. Therefore, those observations confirmed unambiguously that our Milky Way is one among a large variety of galaxies in the observable universe.

Modern studies reveal that our Milky Way is a barred spiral galaxy, typical of the large galaxies that today are in low density environments (Kormendy et al., 2010). In our own Galaxy, we can study the properties of individual stars in unusual detail, and use them as a benchmark for external galaxies. Our current view of the Milky Way is outlined in the schematic diagram of Figure 1.2. The Galaxy is typically dissected in several major components, which present different structural, kinematic and chemical properties, and were presumably generated at different stages of the formation process. In the following, we give a brief overview of the present-day knowledge of the halo (Section 1.1), the bulge (Section 1.2) and the disc (Section 1.3), with special attention to the warp of the Galactic disc and its highly debated formation scenario (Section 1.3.1). The present thesis (whose structure is outlined in Section 1.4) is aimed at contributing to the current understanding of the Galactic warp and its dynamical nature, taking advantage of the unprecedented quality of the astrometric measurements recently made available during the first and the second *Gaia* data releases (Gaia Collaboration et al., 2016, 2018a).

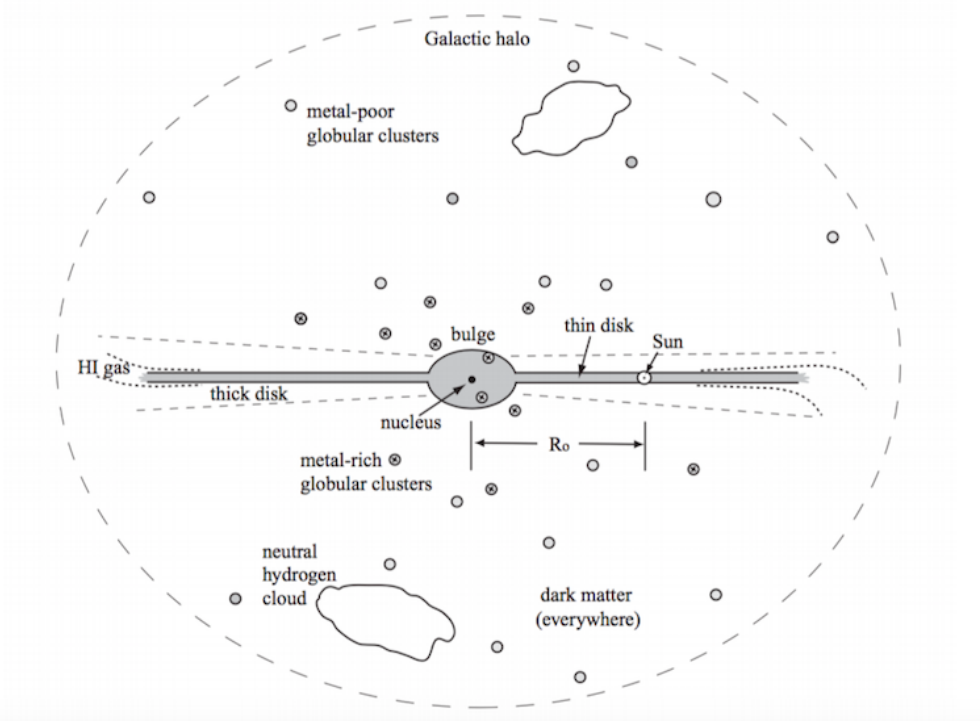

Figure 1.2: Schematic diagram of the Milky Way, showing different Galactic components (Sparke and Gallagher, 2006).

1.1 The halo

Notwithstanding the modest content of Galactic stellar mass (approximately 1 % of the total, Helmi, 2008), the stellar halo represents an important diagnostic for the Milky Way evolution. It contains the oldest stars we know of, not only in the field, but also in globular clusters (Jofré and Weiss, 2011). Early works suggested that the halo stars formed during the dissipative collapse of a single gas cloud, which gave rise to the Milky Way (Eggen et al., 1962). A few years later, Searle and Zinn (1978) proposed alternatively that the halo formed from an aggregation of several cloud fragments, based on their observation on globular clusters chemical abundances. According to the current picture, the two effects both contribute to the buildup of the halo: most of the halo stars accreted from smaller galaxies (Helmi and White, 1999), but a fraction formed *in situ* (Cooper et al., 2015), during the initial gas collapse (Samland and Gerhard, 2003) and/or was born in the disc, but was subsequently scattered on halo orbits (Purcell et al., 2010). The idea of a “dual" nature of the stellar halo was already indicated by the kinematics and metallicities of stars near the Sun (Carollo et al., 2007), showing two broadly overlapping components: an inner halo, with typical metallicities [Fe/H] ≈ -1.6 dex, flattened and slightly prograde, and an outer halo, peaking around [Fe/H] ≈ -2.2 dex, rounder and in net retrograde rotation. The transition between the

inner and the outer halo was measured to be at approximately 30 kpc from the Galactic center (Deason et al., 2011). A plausible explanation for this inner/outer halo duality is that the two components have a different assembly histories, namely, respectively, in situ/accretion origins (Bonaca et al., 2017). The stellar halo is therefore a complex structure with multiple components and unrelaxed substructures, continuously accreting matter (Helmi, 2008). Because of the long dynamical timescales in the halo, it constitues a natural reservoir of merger debris, which remain observable over Gyrs. The Sagittarius stream, originated from the Sagittarius dwarf galaxy, was the first ongoing accretion event to be discovered in the Milky Way halo (Ibata et al., 1994). Since then, numerous substructures of tidally interacting satellites and overdensities have been found, like the Monoceros stream (Rocha-Pinto et al., 2003), the Virgo stellar stream (Duffau et al., 2006), the Orphan stream (Belokurov et al., 2007), the Pisces overdensity (Watkins et al., 2009), amongst others. A complete list of tidal structures identified in the Milky Way has been compiled by Grillmair and Carlin (2016). The Sagittarius stream is by far the largest stream, extending for 360^o around the Galaxy; the geometry of the stream on the sky requires an oblate near-spherical dark matter halo (Ibata et al., 2001), possibly constraining the shape of the dark halo, for which no consistent picture has yet emerged. In modern cosmological models (dominated by cold dark matter), galaxies are embedded in large and massive halos of invisible dark matter, which can be detected only by its gravitational field. The dark halo of the Milky Way accounts for approximately 90% of the total mass of the Galaxy, and extends to at least 100 kpc from the Galactic center (Freeman and Bland-Hawthorn, 2002; Kochanek, 1996).

1.2 The bulge

The Galactic bulge contains approximately a quarter of the Milky Way stellar mass, $M_{bulge} = 2.0 \pm 0.3 \cdot 10^{10} M_{\odot}$ (Valenti et al., 2016), and covers around 500-600 square degrees in the sky. Numerous disc galaxies are observed to have bulges in their centers; however, these features are observed to be heterogeneous in luminosity, metallicity and spatial extension (see the review by Wyse et al., 1997), suggesting a complex nature, which is to date not fully understood. For many years, the bulge of our Galaxy was thought to be a classical bulge, namely a spheroidal remnant of mergers that took place during the hierarchical assembly of the Galaxy. The old ages of bulge stars supported this view (Ortolani et al., 1995), together with the presence of a vertical metallicity gradient (Friedli et al., 1994), which was thought at the time to exclude other formation scenarios. However, gas kinematics (Binney et al., 1991; Englmaier and Gerhard, 1999; Fux, 1999) and near-Infrared (NIR) photometry (Binney et al., 1997; Weiland et al., 1994) have shown that the Galactic bulge contains a triaxial bar structure. The presence of the bar was also confirmed by star counts (Babusiaux and Gilmore, 2005; López-Corredoira et al., 2005; Stanek et al., 1997) and COBE integrated NIR emission (Bissantz and Gerhard, 2002; Dwek et al., 1995). According to most authors, the bar extends to 2-3 kpc from the centre and its major

axis is inclined to the line of sight from 20^o to 30^o. More recently, it was discovered that close to the bulge minor axis, at Galactic latitude $|b| > 5^o$, the red clump giants (RCGs) present a bimodal distribution of stars along the line-of-sight (McWilliam and Zoccali, 2010; Nataf et al., 2010); this effect is caused by the line-of-sight passing through both arms of an X-shaped structure, which is characteristic of boxy/peanut bulges in barred galaxies (Ness et al., 2012; Wegg et al., 2015). Boxy/peanut bulges and X-shaped structures are the projection effects of the complex three-dimensional shape of the bar, when viewed edge-on (Athanassoula, 2016), as in the case of our Galaxy. N-body simulations show that the boxy/peanut morphology arise naturally in bar-forming disc galaxies (Athanassoula, 2016), where dynamical instabilities move stars towards the center, forming a bar, which later bends and buckles giving rise to the X-shape. This support a (at least partly) disc origin of the Galactic bulge, which would be composed of material from the innermost regions to the outer Lindblad resonance (OLR, Di Matteo et al., 2014); current estimates for the OLR range between ≈8-10 kpc (Bland-Hawthorn and Gerhard, 2016). This secular process explains the presence of the observed metal-rich stars in the wide metallicity distribution of the bulge; on the other hand, the observed metal-poor stars might be the product of an early dissipative collapse of a primordial cloud (Rojas-Arriagada et al., 2017). The innermost regions of the bulge contain a super massive black hole having mass of $\approx 4.2 \cdot 10^6 M_\odot$ (Ghez et al., 2008; Gillessen et al., 2009a,b), and a nuclear star cluster with a half-light radius of $\approx 4.2 \pm 0.4$ pc (Schödel et al., 2014).

1.3 The disc

The Solar System being embedded in the Galactic disc (see Figure 1.2), our perspective allows us to obtain large amounts of unique information about Galactic processes. Nevertheless, this benefit comes with a price: due to extinction effects in the visual band and source crowding when close to the Galactic plane, the de-projection of the disc structure is far from trivial. Using near- and far-infrared data from COBE/DIRBE data, Drimmel and Spergel (2001) modeled the three dimensional structure of the Galaxy, reconstructing the spiral structure of the Milky Way (shown in Figure 1.3) (for a more recent map of the spiral arms, see also Reid et al., 2014). The spiral arms are traditionally described as the product of quasi-stationary density waves that propagate around the disc (Lin and Shu, 1964; Lindblad, 1960).The presence of the spiral arms, together with the bar in the central region (Section 1.2) and warp of the outer disc (discussed in Section 1.3.1), reveals that the disc is a non-axysimmetric structure.

The Galactic disc contains a large variety of stars in a wide range of ages, masses and chemical abundances. It is usually described in terms of a thin and a thick disc, whose definition was originally based on geometrical properties, as evidenced by Gilmore and Reid (1983) and Yoshii (1982) from stellar number density profiles. The two components are usually modeled as double exponential discs, with the thin disc being dominant in terms of stellar density (Jurić

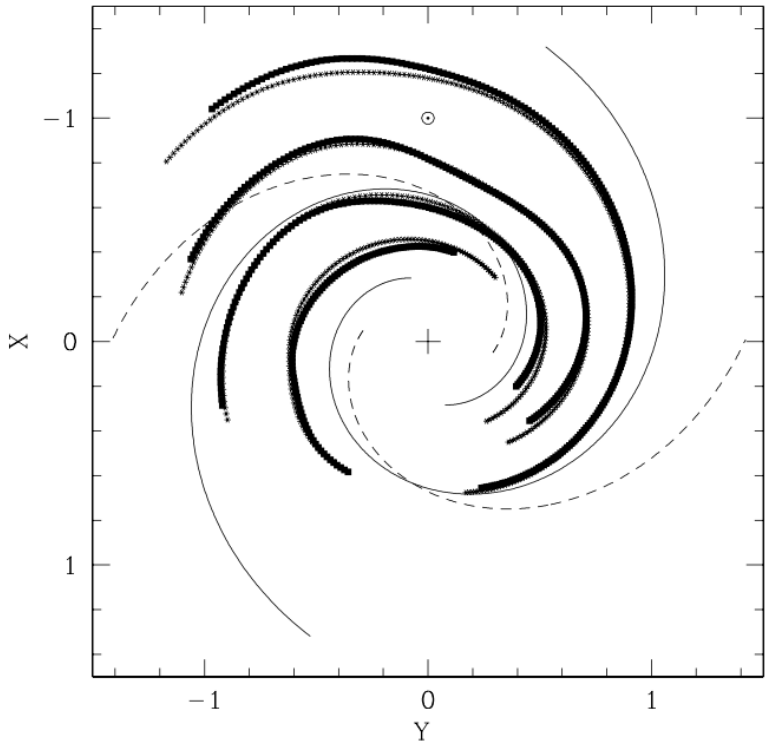

Figure 1.3: From Drimmel and Spergel (2001): Schematic view of the Galaxy showing the four spiral arms as mapped by H II regions and the dust (bold lines), the sheared arms in the K band (stars), and the arms in the two-arm logarithmic model for J- and K-band fit (dashed) and the K-band fit alone (solid) Drimmel and Spergel (2001). The H II spirals are incomplete on the opposite side of the Galaxy owing to lack of data.

et al., 2008). Studies of the age, kinematics, and chemical abundance revealed that the thick disc stars are on average older ($\approx$ 12 Gyr, Gilmore et al., 1995), more α-rich and metal-poor, and kinematically hotter than the those belonging to the thin disc (Bensby et al., 2003; Gilmore et al., 1989; Soubiran et al., 2003). In particular, the distinct trends in metallicity and age (Hayden et al., 2015; Haywood et al., 2013; Navarro et al., 2011) raise the question on how both discs formed and whether or not they share a common formation mechanism. A plausible cause for the thick disc is a minor merger experienced by our Galaxy not before than redshift $z \approx 2$, which caused the heating of a pre-existing thin disc (Villalobos and Helmi, 2008; Wyse, 2001; Wyse et al., 2006).

1.3.1 The Galactic warp

It has been known since the early HI 21-cm radio surveys that the outer gaseous disc of the Milky Way is warped with respect to its flat inner disc (Burke, 1957; Kerr, 1957; Oort et al., 1958; Westerhout, 1957). Later observations showed that our Galaxy is not peculiar with respect to

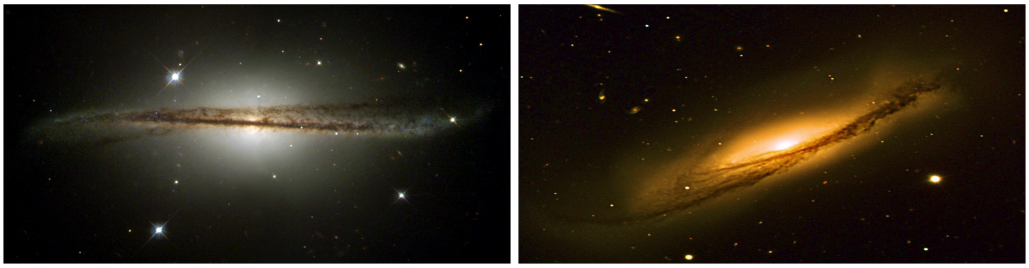

Figure 1.4: Examples of warps in external galaxies. *Left panel*: ESO 510-G13; Credits: NASA and The Hubble Heritage Team (STScI/AURA). *Right panel*: NGC 3190; Credits: ESO/VLT.

other disc galaxies: more than 50 percent of spiral galaxies are warped (Guijarro et al., 2010; Reshetnikov and Combes, 1998; Sanchez-Saavedra et al., 1990). Two examples of warped discs in external galaxies are reported in Figure 1.4. Briggs (1990) studied a sample of 12 warped galaxies with 21-cm data and empirically derived the following trends:

1. The HI layer is typically coplanar inside radius R_{25}[1] (that is inside the solar Galactocentric radius in our Milky Way), and the warp develops between R_{25} and $R_{26.5}$ (the Holmberg radius).

2. The line of nodes tends to be straight inside $R_{26.5}$.

3. Outside $R_{26.5}$, the line of nodes takes the form of a loosely-wound leading spiral, advancing in the direction of Galactic rotation.

As discussed by Kuijken and Garcia-Ruiz (2001), the third effect can be caused by differential rotation of the Galaxy overwhelming the self-gravity of the disc, or to the interaction between the disc and the environment at these radii.

The Galactic HI layer is observed to bend upward in the north (I and II Galactic quadrants) and downward in the south (III and IV Galactic quadrants). Burke (1957); Kerr (1957); Oort et al. (1958) and Westerhout (1957) found independently that the disc maximum deviation from planarity exceeds 300 pc at a Galactocentric distance of 12 kpc. Recently, Levine et al. (2006) re-examined the HI distribution of the outer disc (shown in Figure 1.5), describing the gaseous warp as a superposition of three Fourier modes of azimuthal frequency m =0, 1 and 2, all of which increase with Galactocentric radius. The $m = 0$ mode simply results in a vertical offset, while the $m = 1$ produces an integral-shaped warp. Finally, the $m = 2$ mode accounts for the observed large asymmetry between the northern (Galactic longitude $l \approx 90^o$) and southern ($l \approx 270^o$) warp.

The Galactic warp has since been detected in dust and stars (Drimmel and Spergel, 2001; Freudenreich et al., 1994; López-Corredoira et al., 2002b; Marshall et al., 2006; Miyamoto et al., 1988; Momany et al., 2006; Reylé et al., 2009; Robin et al., 2008). However, it has not been clearly

[1] The radius R_X is defined as the radius where the surface brightness in the B-band is X mag arcsec^{-2}

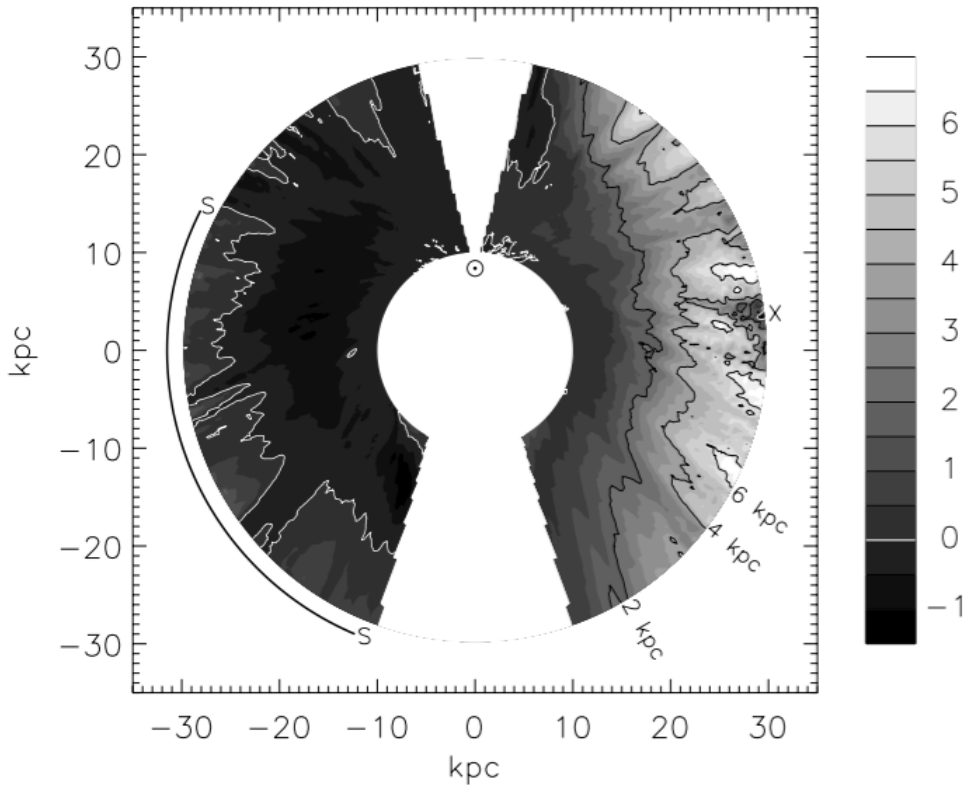

Figure 1.5: The mass-weighted mean height of the gaseous disc above the plane $b = 0^o$ (in kpc) from Levine et al. (2006). The Galactic center and the Sun are located, respectively, in (0,0) and (0,8.5) kpc. The map clearly shows the presence of the Galactic warp. The warp peaks at ≈ 5 kpc in the northern emisphere, while the southern warp only descends to ≈ 1.5 kpc.

established whether the stellar warp is similar or deviates from the gas structure. Miyamoto et al. (1988) found the warp in the OB stars to be consistent with the one observed in the HI disc. The existence of the warp was also confirmed in old stellar populations by López-Corredoira et al. (2002b) with 2MASS data (Skrutskie et al., 1997, 2006), which followed the gaseous warp measured by Burton (1988) (Figure 1.6, top left panel). Similarly, Momany et al. (2006) found an excellent agreement (see Figure 1.6, bottom panel) between the warp in 2MASS red giant stars, gas and dust (Freudenreich et al., 1994); their results also agreed well with the model from Yusifov (2004), based on the distribution of pulsars. In contrast, using COBE/DIRBE data, Drimmel and Spergel (2001) detected a larger amplitude for the warp in the dust than the one seen in stars. A few years later, a similar result was obtained by Reylé et al. (2009) and Robin et al. (2008), who found a less obvious warp in the stars (from 2MASS data) than the one in the gas, as measured by Levine et al. (2006); the amplitude of the warp in the dust from Marshall et al. (2006) was intermediate was intermediate between gas and stars (Figure 1.6, right panel). They also found that the warp in all of the three components appeared to be asymmetric and

with a similar line of nodes. As discussed by Reylé et al. (2009), similarities and/or differences of the warp structure in different Galactic components can shed some light on the dynamical nature of the warp of the Milky Way, which so far remains unkown. In the following, we give an overview of the possible warp formation scenarios.

In spite of the apparent simplicity of their structure, the origin and persistence of warps in disc galaxies represent a topic of ongoing research for the scientific community. The high occurrence of warps (Bosma, 1991), even in isolated galaxies, implies that either these features are easily and continuously generated, or that they are stable over long periods of time. Numerous theoretical models have been proposed to explain warps in disc galaxies (see the review by Binney, 1992; Sellwood, 2013). One of the first theories to be developed describes galactic warps as normal modes of oscillation (i.e. standing waves) of the galactic disc, caused by a persisting misalignment between the spin axis and the disc normal (Lynden-Bell, 1965). Before the discovery of dark matter halos, Hunter and Toomre (1969) found that discrete warp modes in razor-thin discs do not exist unless the edge is unrealistically sharp. Such modes can be realized by the superposition of outgoing and ingoing waves, provided that waves incident on the edge can be reflected. Sparke and Casertano (1988) obtained long-lived warps in rigid, slightly flattened dark haloes, which were insensitive to the details of the disc edge, and succesfully fitted the warps observed in NGC 4565 and NGC 4013. By relaxing the assumption of a rigid dark halo, Binney et al. (1998) and Nelson and Tremaine (1995) found that the response of the dark matter halo to the gravitational influence of the disc would cause the line-of-nodes to wind up within a few dynamical times. Nelson and Tremaine (1995) proposed, therefore, that warps are maintained by some continuos excitation mechanism. According to Battaner et al. (1990), a possible candidate for warp generation is the intergalactic magnetic field; to this scope, the orientation and the strength of the magnetic field is essential. Alternatively, accretion of intergalactic matter can also reproduce warped discs. Ostriker and Binney (1989) found that a gradual infall of material with angular momentum not aligned with the disc forces a flattened galactic halo to reorient; as a consequence, the disc warps so that torques from local self-gravity can balance those exterted by the slewing potential. Within this context, López-Corredoira et al. (2002a) explained the Galactic warp as the result of a torque produced by accretion of intergalactic medium onto the disc. Finally, Hunter and Toomre (1969) proposed that warps can be generated by tidal interaction with one or more satellite galaxies. Bailin (2003); Bailin and Steinmetz (2004) and Ibata and Razoumov (1998) showed that the Sagittarius dwarf galaxy (Sgr) represents a plausible candidate for the origin of the Galactic warp, considering its mass and orbit. Similar results were found for the Large Magellanic Cloud (LMC) by Weinberg and Blitz (2006), who explained most quantitative features of the outer HI layer identified by Levine et al. (2006). Recently, Laporte et al. (2018) confirmed these results for both the LMC and Sgr, and proposed a positive interference of the combined effects of the two satellites.

1.4 Motivation and outline of this thesis

While numerous possible mechanisms for generating warps in disc galaxies have been proposed (Section 1.3.1), which one is actually at work for our own Galaxy remains a mystery. This is due to the fact that, while the shape of the Galactic warp is roughly known, its dynamical nature is not. In this respect, kinematic data contain valuable information, as they trace the underlying forces of the Galaxy. In particular, the kinematic signature of the Galactic warp is expected to manifest itself toward the Galactic anticenter as large-scale systematic velocities perpendicular to the Galactic plane, as will be largely discussed throughout this Thesis. The exquisite quality of the recently available *Gaia* data is expected to improve our understanding of the Galaxy, including its warped disc. The purpose of this Thesis is to contribute to the current understanding of the Galactic warp, taking advantage of *Gaia* data. The present introductory Chapter (Part I) is followed by the kinematic analysis of a sample of OB stars from the *Hipparcos* subset (Part II, including Chapter 2, 3 and 4) and the TGAS catalogue in the first data *Gaia* release (Part III, including Chapter 5, 6 and 7). Then, we present a comparison of the kinematics of OB and giants stars from the second *Gaia* data release (Part IV, 8 and 9). Finally, we summarize the obtained results and outline the future perspectives (Part V, Chapter 10).

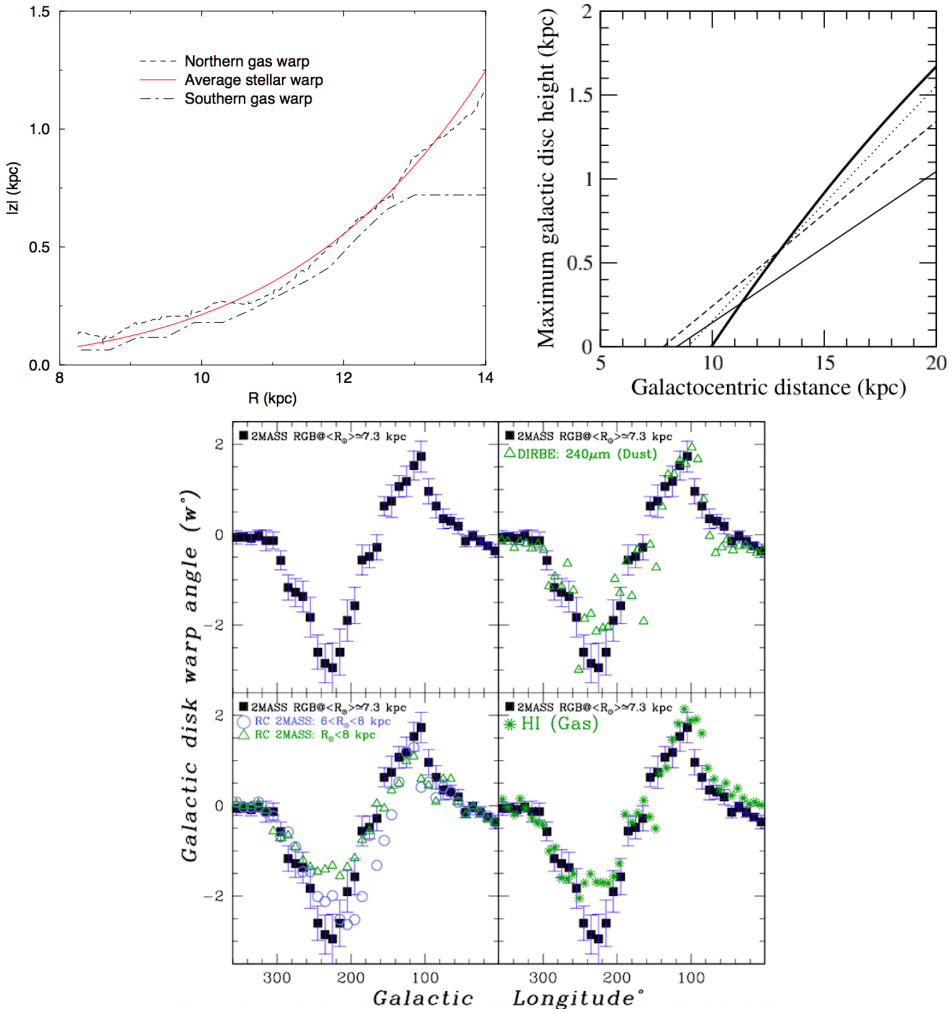

Figure 1.6: Comparison of measured warp amplitudea in different Galactic components according to the literature. *Top left panel*: maximum amplitude of the warp from 2MASS old stellar population in function of Galactocentric radius R, as calculated by López-Corredoira et al. (2002b) (solid line), compared to the one measured by Burton (1988) for the Northern and Southern warp in the gas (dashed and dot-dashed curves, respectively). Figure from López-Corredoira et al. (2002b). *Top right panel*: same as left panel, from Reylé et al. (2009). The thin solid line shows the stellar warp, as measured by Reylé et al. (2009) with the 2MASS catalogue. The thick solid line shows the $m = 1$ mode from Levine et al. (2006) (see text). The dashed and dotted line show, respectively, the dust model from Marshall et al. (2006) at positive and negative Galactic longitudes. *Bottom panel*: warp amplitude in function of Galactic longitude, as measured by Momany et al. (2006) for 2MASS red giants, for the dust (from DIRBE at 240 μm data) and neutral HI gas from Freudenreich et al. (1994).

Part II

The kinematic signature of the Galactic warp: the Hipparcos subset in *Gaia* DR1

CHAPTER 2

THE HIPPARCOS SUB-SAMPLE

Our Milky Way presents the opportunity for a unique case study of galactic warps, on the grounds that stellar motions can be studied in great detail. At present, there is no consensus on the mechanism responsible for the warp in our Galaxy, as discussed in Section 1.3.1. To have better knowledge of the warp dynamical nature, an important contribution would be kinematic information perpendicular to the galactic disc, in which the Galactic warp is expected to leave a signature. Being located within the disc of the Milky Way, disc systematic vertical motions associated with the Galactic warp will primarily manifest themselves to us in the direction perpendicular to our line-of-sight (LOS). However, vertical systematic motions are not evident in radio surveys, that only reveal the velocity component along the LOS. Recent studies of the neutral HI component (Kalberla et al., 2007; Levine et al., 2006) confirm that the Galactic warp is already evident at a galactocentric radius of 10 kpc, while the warp in the dust and stellar components are observed to start inside or very close to the Solar circle (Derriere and Robin, 2001; Drimmel and Spergel, 2001; Robin et al., 2008). If the warp is stable, we expect the associated vertical motions to be evident in the component of the stellar proper motions perpendicular to the Galactic disc.

A first attempt to detect a kinematic signature of the warp in the proper motions of stars was first made using OB stars (Miyamoto et al., 1988). More recently, a study of the kinematic warp was carried out by Bobylev (2010, 2013), claiming a connection between the stellar-gaseous warp and the kinematics of their tracers, namely nearby red clump giants from Tycho-2 and Cepheids with UCAC4 proper motions. Using red clump stars from the PPMXL survey, López-Corredoira et al. (2014) concluded that the data might be consistent with a long-lived warp, though they admit that smaller systematic errors in the proper motions are needed to confirm this tentative finding. Indeed, large-scale systematic errors in the ground-based proper motions compromise

efforts to detect the Galactic warp. The first real hopes of overcoming such systematics came with global space-based astrometry. However, using *Hipparcos* (ESA, 1997) data for OB stars, Smart et al. (1998) and Drimmel et al. (2000) found that the kinematics were consistent neither with a warp nor with a flat unwarped disc.

Before the recent arrival of the first *G*aia Data Release (*G*aia DR1 Gaia Collaboration et al., 2016), the best all-sky astrometric accuracy is found in the New Reduction of the *Hipparcos* catalogue (van Leeuwen, 2008), which improved the quality of the astrometric data by more than a factor of two with respect to the original *Hipparcos* catalogue. For the *Hipparcos* subsample, the *G*aia DR1 astrometry is improved further by more than an order of magnitude. Part II of this Thesis (Chapter 2, 3 and 4) is aimed at assessing whether either the New Reduction of the *Hipparcos* catalogue or the new *Gaia* astrometry for the OB stars in the *Hipparcos* subset shows any evidence of the systematics expected from a long-lived warp. The present Chapter is dedicated to the description of the data; Chapter 3 presents the model; finally, Chapter 4 describes the analysis and reports the obtained results. Chapter 2, 3 and 4 are partly based on Poggio et al. (2017).

A general introduction to the data from the first *Gaia* release is provided in Section 2.1, followed by a brief description of the catalogues used in Part II of this Thesis (Section 2.2). Finally, Section 2.3 is dedicated to the data selection process.

2.1 Introduction to Gaia DR1

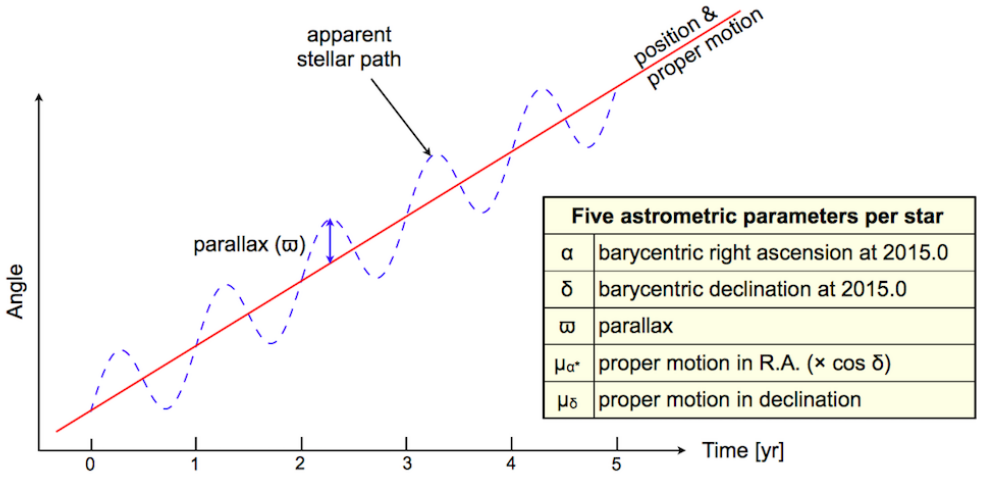

Figure 2.1: Schematic diagram for the astrometric model of a single star. From the presentation of L. Lindegren at IAU Symposium 330. (https://iaus330.sciencesconf.org/resource/page/id/27)

The first *Gaia* data release (*Gaia* DR1, Gaia Collaboration et al., 2016) is based on the data collected during the first 14 months of *Gaia*'s observations. This time interval is not long enough

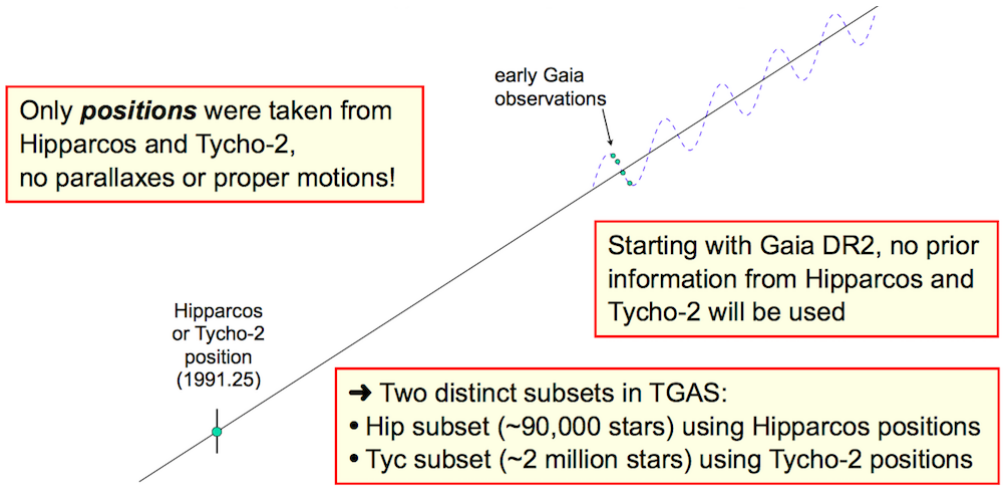

Figure 2.2: Schematic diagram of the TGAS astrometric process, using *Hipparcos* and *Tycho-2* positions are priors. From the presentation of L. Lindegren at IAU Symposium 330. (https://iaus330.sciencesconf.org/resource/page/id/27)

to successfully estimate all five astrometric parameters of each source (positions, parallax and proper motions, see Figure 2.1), as it would require at least 18 months of observations Lindegren (2018). Nevertheless, five-parameter astrometric solution was published for 2 057 050 sources in common between *Gaia* DR1 (containing 1 142 679 769 sources, Gaia Collaboration et al., 2016) and the two catalgoues *Hipparcos* (containing 117 955 sources, van Leeuwen, 2008) and *Tycho-2* (containing 2 539 913 sources, Høg et al., 2000), forming the *Gaia* DR1 primary sample, also called TGAS (*Tycho-Gaia astrometric solution*) catalogue (Michalik et al., 2015). For those stars, an astrometric non-degenerate solution was obtained by incorporating positions from the *Hipparcos* and *Tycho-2* catalogues at their epochs (around 1991.25), as shown in Figure 2.2. Following this procedure, the uncertainties of the TGAS proper motions strongly depend on the precision of the *Hipparcos* and *Tycho-2* positions, used as priors, as shown in Figure 2.3. On the contrary, parallax uncertainty are not drastically different between the *Hipparcos* and *Tycho-2* catalogues, with overall median uncertainty of 0.28 mas and 0.32 mas, respectively (Lindegren, 2018). As mentioned before, the kinematic signature of the warp will be analyzed using both the *Hipparcos* subset in *Gaia* DR1 (here, Part II) and the TGAS catalogue (Part III).

2.2 The Hipparcos subset in Gaia DR1

In Part II of this Thesis, we make use of the astrometric measurements from the *Hipparcos* sub-sample in *Gaia* DR1 (hereafter TGAS(HIP2)), as well as the pre-*Gaia* measurements from the New *Hipparcos* Reduction (hereafter HIP2). Because of the intrinsic connection, by construction, between the astrometry of TGAS(HIP2) and HIP2 (see Section 2.1), a study of the *Hipparcos* error

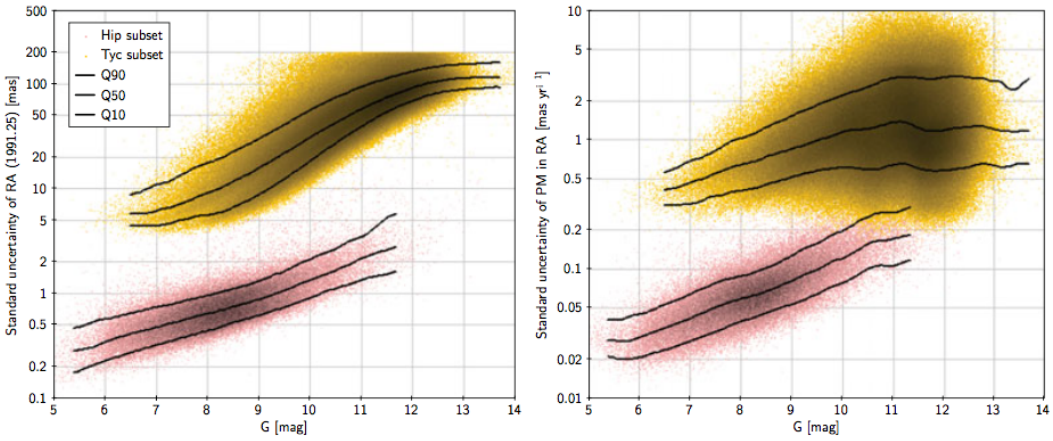

Figure 2.3: From Lindegren (2018): *Left:* Positional uncertainties at epochs around J1991.25 in the *Hipparcos* and *Tycho-2* catalogues. These positions are used as priors in the TGAS solution. *Right:* Uncertainties of the proper motions in the TGAS catalogue. In both diagrams the lower cloud shows the ≈ 93000 *Hipparcos* sources in TGAS, the upper cloud the ≈ 2 million *Tycho-2* sources. The curves are the quantiles at 10%, 50% (median) and 90%. Only the component in right ascension are shown.

properties is necessary for understanding the astrometric error properties of TGAS(HIP2), as discussed in Section 3.6. Finally, the two samples are complementary, as HIP2 can be considered more complete and is substantially larger (see Figure 2.4) than TGAS(HIP2), which present superior astrometry.

2.3 Data Selection

From the HIP2 catalogue, we select the OB stars, as they are intrinsically bright, thus can be seen to large distances. Moreover, being short-lived, they are expected to trace the warped gaseous component from which they were recently born. However, the spectral types in the HIP2 are simply those originally provided in the first *Hipparcos* release. In the hope that the many stars originally lacking luminosity class in the *Hipparcos* catalogue would have by now received better and more complete spectral classifications, we surveyed the literature of spectral classifications available since the *Hipparcos* release. Most noteworthy for our purposes is the Galactic O-star Spectroscopic Survey (GOSSS) (Maíz Apellániz et al., 2011; Sota et al., 2011, 2014), an ongoing project whose aim is to derive accurate and self-consistent spectral types of all Galactic stars ever classified as O type with B_J magnitude < 12. From the catalogue presented in Sota et al. (2014), which is complete to $B_J = 8$ but includes many dimmer stars, we imported the spectral classifications for the 212 stars that are present in the HIP2 catalogue. Thirteen of these HIP2 sources were matched to multiple GOSSS sources, from which we took the spectral classification

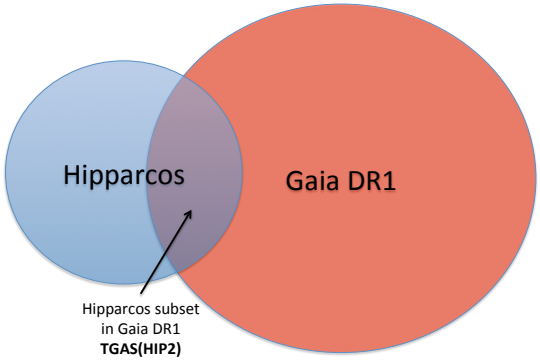

Figure 2.4: Venn diagram showing the *Hipparcos* subset in Gaia DR1 (TGAS(HIP2)) as the intersection of the New *Hipparcos* Reduction (van Leeuwen, 2008) and the Gaia DR1 primary sample (see text). For a detailed description of the completeness of TGAS(HIP2) see Section 3.4.

of the principle component. Also worth noting is the Michigan Catalogue of HD stars (Houk, 1993, 1994; Houk and Cowley, 1994; Houk and Smith-Moore, 1994; Houk and Swift, 2000), which with its 5th and most recent release now covers the southern sky ($\delta < 5°$), from which we found classifications for an additional 3585 OB stars. However, these two catalogues together do not cover the whole sky, especially for the B stars. We therefore had to resort to tertiary sources that are actually compilations of spectral classifications, namely the Catalogue of Stellar Spectral Classifications (4934 stars; Skiff (2014)), and the Extended Hipparcos Compilation (3216 stars; Anderson and Francis (2012)). In summary, we have spectral classifications for 11947 OB stars in *Hipparcos*.

We select from the HIP2 only those stars with spectral type earlier than B3, with an apparent magnitude $V_J \leq 8.5$, and with galactic latitude $|b| < 30^o$, resulting in 1848 OB stars. From this sample of HIP2 stars we define two subsamples: a HIP2 sample whose measured *Hipparcos* parallax is less than 2 mas, and a TGAS(HIP2) sample consisting of those HIP2 stars that appear in the *Gaia* DR1 whose measured TGAS parallax is less than 2 mas. The cut in parallax, together with the cut in galactic latitude, is done to remove local structures (such as the Gould Belt), and approximately corresponds to 500 pc in heliocentric distance. Our HIP2 sample contains 1088 stars (including 18 stars without luminosity class), while our TGAS(HIP2) sample contains only 788 stars. This lack of HIP2 in TGAS stars is largely due to the completeness characteristics of DR1, discussed further in Section 3.4 below.

Notwithstanding the parallax cut we found that there were HIP2 stars in our sample that are members of nearby OB associations known to be associated with the Gould Belt. We therefore removed from the HIP2 sample members of the Orion OB1 association (15 stars, as identified

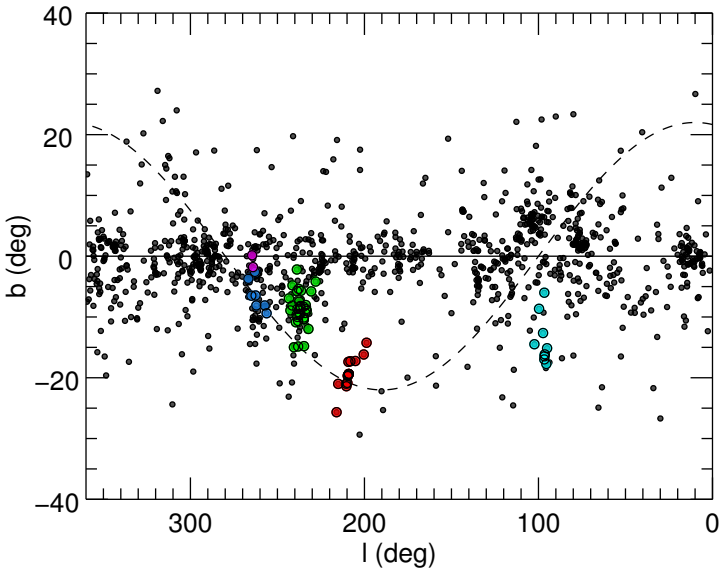

Figure 2.5: Our final sample of *Hipparcos* OB stars on the sky, plotted in galactic coordinates. The dashed line shows the orientation of the Gould belt according to Comeron et al. (1992). Colored points indicate the stars that are identified members of the OB associations Orion OB1 (red), Trumpler 10 (purple), Vela OB2 (blue), Collinder 121 (green) and Lacerta OB1 (cyan).

by Brown et al. (1994)) and, as according to de Zeeuw et al. (1999), members of the associations Trumpler 10 (2 stars), Vela OB2 (7 stars), Lacerta OB1 (9 stars), all closer than 500 pc from the Sun. We also removed 33 stars from the Collinder 121 association as it is thought to also be associated with the Gould Belt. With these stars removed we are left with a final HIP2 sample of 1022 stars. It is worth noting that the superior *Gaia* parallaxes already result in a cleaner sample of distant OB stars: only 21 members of the above OB associations needed to be removed from the TGAS(HIP2) sample after the parallax cut. Figure 2.5 shows the position of the stars in our two samples in Galactic coordinates.

Due to the above mentioned parallax cut, our sample mostly contains stars more distant than 500 pc. Though our analysis will only marginally depend on the distances, we use spectro-photometric parallaxes when a distance is needed for the HIP2 stars, due to the large relative errors on the trigonometric parallaxes. For this purpose, absolute magnitudes and intrinsic colors are taken from Martins et al. (2005) and Martins and Plez (2006) for the O stars, and from Humphreys and McElroy (1984) and Flower (1977) for the B stars (see Appendix A).

We note that the OB stars with $V_J \leq 7.5$ (approximately 90% complete) beyond the Solar Circle ($90^o < l < 270^o$) show a tilt with respect to the Galactic plane that is consistent with a Galactic warp: a robust linear fit in the l-b space (l normalized to $180^o - l$) yields a slope of

0.049 ± 0.007 (see Figure 2.6). However, given the possible effects of patchy extinction, it would be risky to make any detailed conclusions about the large scale geometry of the warp from this sample with heliocentric distances limited to a few kiloparsecs.

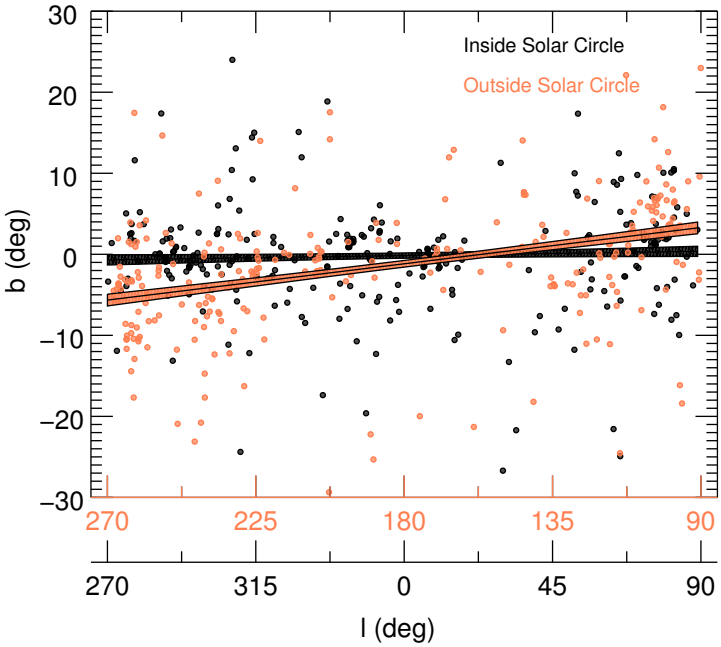

Figure 2.6: l, b distributions toward ($l < 90^o$ and $l > 270^o$, black) and away ($90^o < l < 270^o$, orange) from the Galactic center. The solid lines represent the robust linear fits for the two ditributions, together with the 1σ confidence bands.

CHAPTER 3

THE MODEL

In the present Chapter, we describe the model used to produce synthetic catalogues and probability distribution functions of the observed quantities, to be compared with our two samples of *Hipparcos* OB-stars described in Chapter 2, taking into account the error properties of the *Hipparcos* astrometry (for the HIP2 sample) and of the Hipparcos subsample in Gaia DR1 (for the TGAS(HIP2) sample), and applying the same selection criteria used to arrive at our two samples. The distribution on the sky and the magnitude distribution of the HIP2 sample to $V = 7.5$ (556 stars), assumed to be complete, are first reproduced in Sections 3.2 and 3.3, using models of the color-magnitude and spatial distribution of the stars, and a 3D extinction model. The completeness of *Hipparcos*, and of TGAS with respect to *Hipparcos*, is described in Section 3.4 and is used to model our two samples down to $V = 8.5$. Then a simple kinematic model for the OB stars is used to reproduce the observed distribution of proper motions (Section 3.5) of our two samples, including (or not) the expected effects of a stable (long-lived) non-precessing warp (Section 3.1). A comparison of the observed samples with the expectations from the different warp/no-warp models is presented in Chapter 4.

The model that we present here is purely empirical. Many parameters are taken from the literature, while a limited number have been manually tuned when it was clear that better agreement with the observations could be reached. We therefore make no claim that our set of parameters are an optimal set, nor can we quote meaningful uncertainties. The reader should thus interpret our choice of parameters as an initial "first guess" for a true parameter adjustment, which we leave for the future when a larger dataset from *Gaia* is considered. In any case, after some exploration, we believe that our model captures the most relevant features of the OB stellar distribution and kinematics at scales between 0.5 – 3 kpc.

3.1 Warp

The Galaxy can be modeled as a collisionless system in which the fundamental particles (the stars) move under the influence of a smooth potential $\Phi(\vec{x},t)$. The system can be fully described by the *phase-space density* $f(\vec{x},\vec{v},t)$, which is $f \geq 0$ everywhere in phase space. The Collisionless Boltzmann Equation (CBE)

$$\frac{df}{dt} = 0 \tag{3.1}$$

states that the flow of the points through the phase space is incompressible, or, in other words, there are no particles appearing or disappearing. We can rewrite Equation 3.1 by means of the phase space coordinates:

$$\frac{\partial f}{\partial t} + \sum_{i=1}^{3}\left(v_i \frac{\partial f}{\partial x_i} - \frac{\partial \Phi}{\partial x_i}\frac{\partial f}{\partial v_i}\right) = 0 \quad . \tag{3.2}$$

In general, it is not trivial to solve the CBE, because it is function of 7 variables. Therefore, it is convenient to take moments of this equation. Here we consider the 0^{th} moment equation, which corresponds to a continuity equation for a fluid. We integrate over all possible velocities, defining the spatial density of stars $\rho(\vec{x},t) \equiv \int f d^3\vec{v}$ and the mean velocities $\bar{v}_i = \frac{1}{\rho}\int f d^3\vec{v}$, obtaining the following equation:

$$\frac{\partial \rho}{\partial t} + \sum_{i=1}^{3}\frac{\partial(\rho \bar{v}_i)}{\partial x_i} = 0 \quad . \tag{3.3}$$

For our purposes, it is convenient to write Equation 3.3 in Galactocentric cylindrical coordinates (R,ϕ,z), assuming that we have no mean radial motions $\bar{v}_R = 0$ (i.e. that the disc is not expanding or collapsing along the radial direction):

$$\frac{\partial \rho}{\partial t} + \frac{1}{R}\frac{\partial(\rho \bar{v}_\phi)}{\partial \phi} + \frac{\partial(\rho \bar{v}_z)}{\partial z} = 0 \quad . \tag{3.4}$$

We can further simplify the above equation by assuming, to a first approximation, that the azimuthal velocity only depends on R and that the mean vertical velocity only depends on (R,ϕ):

$$\frac{\partial \rho}{\partial t} + \frac{\bar{v}_\phi}{R}\frac{\partial \rho}{\partial \phi} + \bar{v}_z \frac{\partial \rho}{\partial z} = 0 \quad . \tag{3.5}$$

To solve Equation 3.5, we need to define the stellar density ρ; we therefore construct a flat-disc distribution with vertical exponential profile ($\rho \propto e^{-\frac{|z|}{h_z}}$, with scale height h_z, see Section 3.3) then model the warp as a displacement of the z-coordinates by z_w ($\rho \propto e^{-\frac{|z'|}{h_z}}$, with $z' = z - z_w$), where:

$$z_w(R,\phi) = h(R)\sin(\phi + \phi_w) \quad . \tag{3.6}$$

The warp phase angle ϕ_w determines the position of the line-of-nodes of the warp with respect to the galactic meridian ($\phi = 0$). The increase of the warp amplitude with Galactocentric radius, $h(R)$, is described by the height function

$$h(R) = h_0 (R - R_w)^{\alpha_w} \quad , \tag{3.7}$$

where h_0 and R_w are the warp amplitude and the radius at which the Galactic warp starts, respectively. The exponent α_w determines the warp amplitude increase. Table 3.1 reports three different sets of warp parameters taken from the literature and used later in our analysis in Chapter 4.

Table 3.1: Comparison of warp parameters for the models of Drimmel and Spergel (2001) and Yusifov (2004). The radius R_w was scaled to account for different assumptions about the Sun - Galactic center distance in this work and in the considered papers.

	R_w (kpc)	α_w	h_0(kpc$^{\alpha_w - 1}$)	ϕ_w(^{o})
Drimmel and Spergel (2001), dust	7	2	0.073	0
Drimmel and Spergel (2001), stars	7	2	0.027	0
Yusifov (2004)	6.27	1.4	0.037	14.5

For a given set of spatial parameters, we are able to predict the expected mean vertical velocity $\bar{v}_z(R, \phi)$ for a warped disc by solving Equation 3.5:

$$\bar{v}_z(R, \phi) = \frac{\bar{v}_\phi}{R} h(R) \cos(\phi + \phi_w) \quad . \tag{3.8}$$

Equations 3.6, 6.8 and 3.8 assume a perfectly static warp. It is of course possible to construct a more general model by introducing time dependencies in Equations 3.6 and 6.8, which will result in additional terms in Equation 3.8, including precession or even an oscillating (i.e. "flapping") amplitude. For our purpose here, to predict the expected systematic vertical velocities associated with a warp, such time dependencies are not considered.

This above model we refer to as the *warp model*, with three possible sets of parameters reported in Table 3.1. Our alternative model with $z_w = 0$ will be the *no-warp model*, where Equation 3.8 reduces to the trivial $\bar{v}_z = 0$.

Figure 3.1 shows the modeled spatial warp (left panel) and its kinematic signature (right panel) according to Equations 3.6 and 3.8, respectively. The corresponding plot for the mean proper motions μ_b in the Galactic plane is shown in Figure 3.2, right plot, compared to the expectation for the no-warp model (Figure 3.2, left plot). In the latter case, we expect to have negative μ_b values symmetrically around the Sun as the reflex of the vertical component of Solar motion, progressively approaching 0 with increasing heliocentric distance. For a warp model, a variation of μ_b with respect to galactic longitude is introduced (see also Figure 3.3), with a peak toward the anti-center direction ($l = 180^o$). Figure 3.3 also shows that a variation of the warp

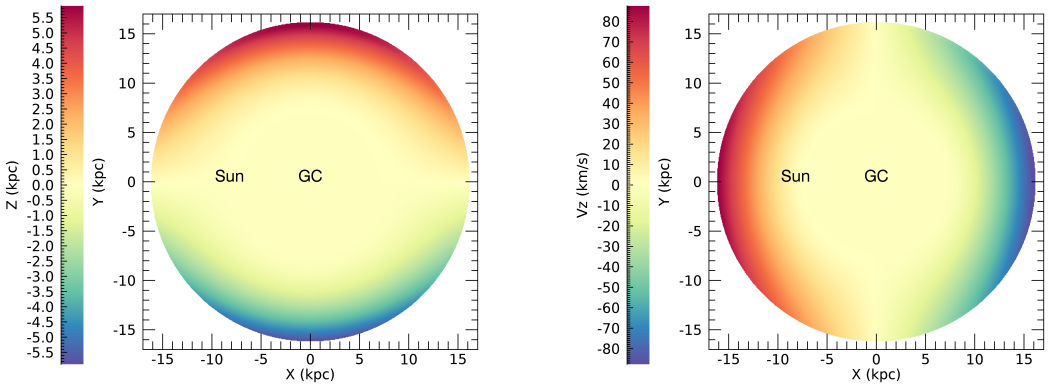

Figure 3.1: *Left:* The spatial model of the warp, according to Equations 3.6 and 6.8, adopting the dust parameters from Drimmel and Spergel (2001) (dust). *Right:* The corresponding kinematic signature in the mean vertical velocities, according to Equation 3.8. The Galactic Center (GC) is located in the center (X,Y)=(0.0) kpc. For the Sun-GC distance, we adopt $R_\odot = 8.2$ kpc (Bland-Hawthorn and Gerhard, 2016, see Section 3.3), so that the Sun is at (X,Y)=(0,-8.2) kpc. The Galaxy is rotating clockwise.

phase angle has a rather minor effect on the kinematic signature, nearly indistinguishable from a change in the warp amplitude.

3.2 Luminosity function

There are different initial luminosity functions (ILF) in the literature for the upper main sequence (Bahcall and Soneira; Bahcall et al., 1987; Humphreys and McElroy, 1984; Reed, 2001; Scalo, 1986). Given the uncertainties in the ILF for intrinsically bright stars (absolute magnitude $M < -3$), we assume $N(M) \propto 10^{\alpha M}$, and use the value $\alpha = 0.72$ that we find reproduces well the apparent magnitude distribution (Figure 3.8) with the spatial distribution described in Section 3.3. We use a main sequence Color-Magnitude relation consistent with the adopted photometric calibrations (see Chapter 2 and Appendix A). The procedure described in the following is partly based on previous works (for example Smart et al., 1997). Absolute magnitudes M are randomly generated consistent with this ILF; then, for a given absolute magnitude, stars are assigned an intrinsic color generated uniformly inside a specified width about the main sequence (Figure 3.4), which linearly increases as stars get fainter. According to an assumed giant fraction (see below), a fraction of the stars are randomly labelled as giant. The absolute magnitude of these stars are incremented by -0.5 mag, and their color is generated uniformly between the initial main sequence color and the reddest value predicted by our calibrations, $(B-V)_0 = -0.12$. The

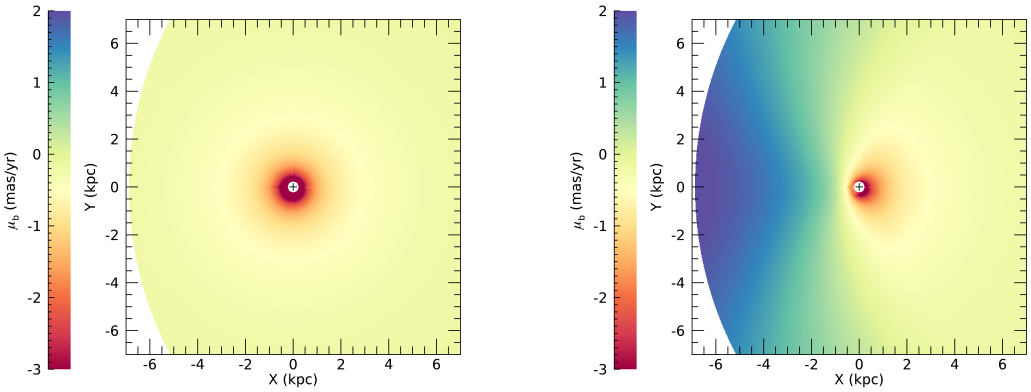

Figure 3.2: *Left:* The expected proper motions μ_b (without considering measurement errors) in the Galactic plane $b = 0^o$ for a flat disc (i.e. our *no-warp model*). The only evident feature is the reflex of the motion of the Sun, which is located at (X,Y)=(0,0) kpc (black cross). The Galactic center is at (X,Y)=(0,8.2) kpc, towards the right, outside the borders of the plot. *Right:* Same as left panel, but for our *warp model*. The warp kinematic signature is apparent as the systematic motions (blue region) toward the Galactic anticenter direction ($l = 180^o$, left side of the plot). Proper motions are calculated assuming the Solar motion $v_\odot = (U_\odot, V_\odot, W_\odot) = (11.1, 12.24, 7.25)$ km s^{-1} from Schönrich et al. (2010) (see Section 3.5).

giant fraction f_g has been modelled as a function of the absolute magnitude as follows:

$$f_g(M) = \begin{cases} 1, & \text{if } M \leq -7 \\ -0.25M - 0.75, & \text{if } -7 \leq M \leq -4 \\ 0.25, & \text{if } M \geq -4 \end{cases} ,$$

in order to roughly reproduce the fraction of giants in the observed catalogue. We caution that this procedure is not intended to mimic stellar evolution. Instead, we simply aim to mimic the intrinsic color-magnitude distribution (i.e. Hess diagram) of our sample. The simple luminosity function model presented here will be improved on when considering the complete TGAS sample (see Section 6.1.2).

3.3 Spatial distribution and extinction

Since we wish to model the distribution of OB stars on scales larger than several hundred parsecs, we use a mathematical description of this distribution that smooths over the inherent clumpy nature of star formation, which is especially evident if we consider the distribution of young stars within 500 pc of the Sun. On these larger scales it is nevertheless evident that the OB stars are far from being distributed as a smooth exponential disc, but rather trace out the spiral arms of

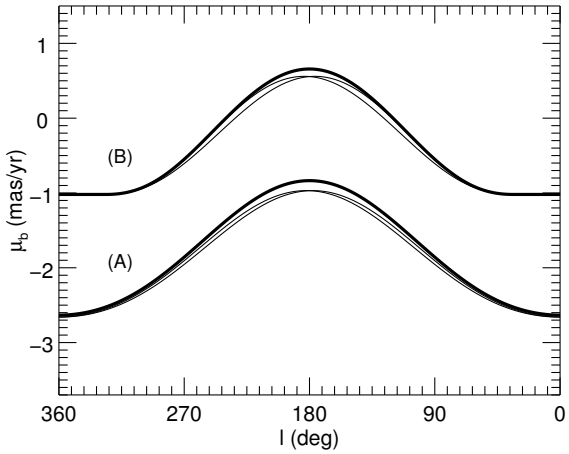

Figure 3.3: According to the warp model, the true μ_b in the Galactic plane as a function of Galactic longitude at heliocentric distances of 0.5 kpc (A) and 1.5 kpc (B). For each set of curves, the thick line represents the case with warp phase $\phi_w = 0^o$ and the two thin curves show $\phi_w = \pm 20^o$.

the Galaxy, being still too young to have wondered far from their birth-places. In our model we adopt $R_0 = 8.2$ kpc as the Sun's distance from the Galactic center, and a solar offset from the disc midplane of $z_0 = 25$ pc, for Galactocentric cylindrical coordinates (R, ϕ, z), as recommended by Bland-Hawthorn and Gerhard (2016). For the spiral arm geometry we adopt the model of Georgelin and Georgelin (1976), as implemented by Taylor and Cordes (1993), rescaled to $R_0 = 8.2$ kpc, with the addition of a local arm, modelled as a logarithmic spiral segment whose location is described by

$$R_{Loc} = R_{Loc,0} \exp -(\tan p\phi) \quad ,$$

p being the arm's pitch angle. The surface density profile across an arm is taken to be gaussian, namely: $\rho \propto \exp(-d_a^2/w_a^2)$, where d_a is the distance to the nearest arm in the R, ϕ plane, and $w_a = c_w R$ is the arm half-width, with $c_w = 0.06$ (Drimmel and Spergel, 2001). An "overview" of the modelled surface density distribution is shown in Figure 3.5. The stars are also given an exponential vertical scale height $\rho \propto \exp(-|z'|/h_z)$, where h_z is the vertical scale height and $z' = z - z_w - z_{Loc}$, $z_w(R, \phi)$ being the height of the warp as described in section 3.1, and z_{Loc} is a vertical offset applied only to the local arm.

We generate the above spatial distribution in an iterative Monte-Carlo fashion. Ten thousand positions in (x, y) coordinates are first generated with a uniform surface density to a limiting heliocentric distance of 11 kpc, and with an exponential vertical profile in $|z'|$. The relative surface density $\Sigma(x, y)$ is evaluated at each position according to our model described above, and positions are retained if $u < \Sigma(x, y)/max(\Sigma)$, where u is a uniform random deviate between 0 and 1. Each retained position is assigned to a $(M_V, (B-V)_0)$ pair, generated as described in the

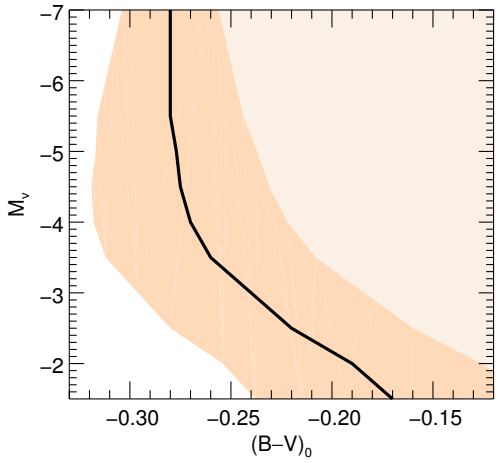

Figure 3.4: Color-Magnitude diagram used to generate synthetic intrinsic colors. The dark and light orange regions shows, respectively, the main sequence and the giant regions. The density of the two regions (here not shown) depends on the ILF and on the giant fraction.

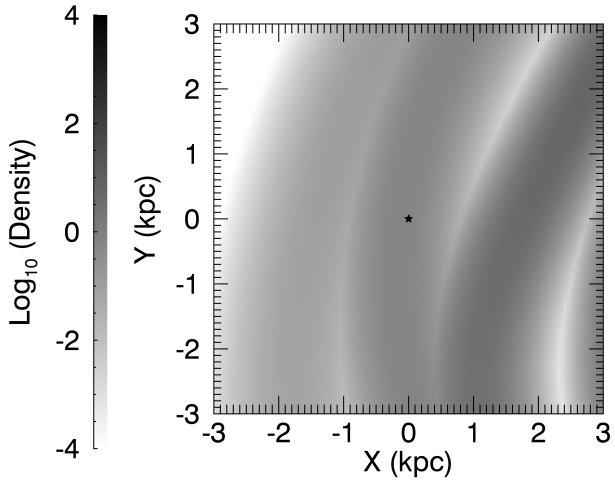

Figure 3.5: Modelled Surface density of the OB stars. Sun's position is indicated by the star.

previous section. The extinction to each position is then calculated using the extinction map from Drimmel et al. (2003) and the apparent magnitude is derived. Based on the apparent magnitude, a fraction of the stars with $V \leq 8.5$ are randomly retained consistent with the completeness model of *Hipparcos* (see Section 3.4), while for a TGAS-like catalogue an additional random selection of stars is similarly made as a function of the observed apparent magnitude and color, as described in the following Section. This procedure is iterated until a simulated catalogue of

stars is generated matching the number in our observed sample.

Good agreement with the HIP2 distribution in galactic latitude was found adopting a vertical scale height $h_z = 70$ pc and assuming $z_{Loc} = 25$ pc, as shown in Figure 3.6. Figure 3.7 compares the modelled and observed distributions in galactic longitude, which is dominated by the local arm. This observed distribution is reproduced by placing the local arm at a radius of $R_{Loc,0} = 8.3$ kpc, with a pitch angle of 6.5° and a half-width of 500 pc. (The curves in Figures 3.6 and 3.7 are non-parametric fits to the distributions obtained through kernel density estimation with a gaussian kernel, as implemented by the generic function *density* in R [1]. The smoothing bandwith is fixed for all the curves in the same figure, with values of 2.5° and 15° for the latitude and the longitude distribution, respectively.)

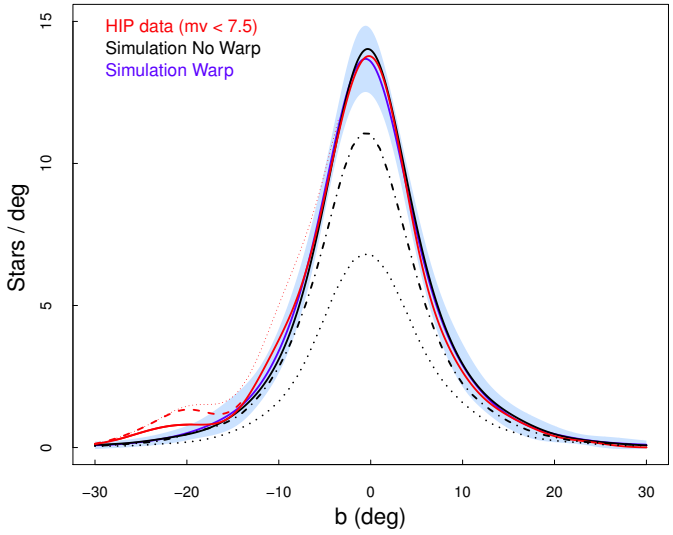

Figure 3.6: Latitude distribution of the HIP2 OB stars. The red curve is a non-parametric fit to the selected HIP2 sample, the red dashed curve shows the additional contribution of the Orion OB1 association, while the red dotted the added contributions of the Trumpler 10, Vela OB2, Collinder 121 and Lacerta OB1 associations. The blue curve and light-blue shaded area shows the average and 2 σ confidence band of the simulated longitude distribution, based on 30 simulated instances of the sample. The black dotted and dash-dot curves show the relative contributions of the major spiral arms (Sagittarius-Carina and Perseus) and the local arm, respectively, while the additional black solid curve is for a model without a warp.

Figure 3.8 shows the resulting apparent magnitude distribution, as compared to the HIP2 sample. Comparing the observed and the simulated longitude distributions in Figure 3.7, we note that our model fails to reproduce well the observed distribution in the longitude range $l = 300-360$ degrees. This is probably revealing a deficit in the geometry adopted for the Sagittarius-Carina arm, which we have not attempted to modify as we are primarily interested in the kinematics

[1] https://www.r-project.org

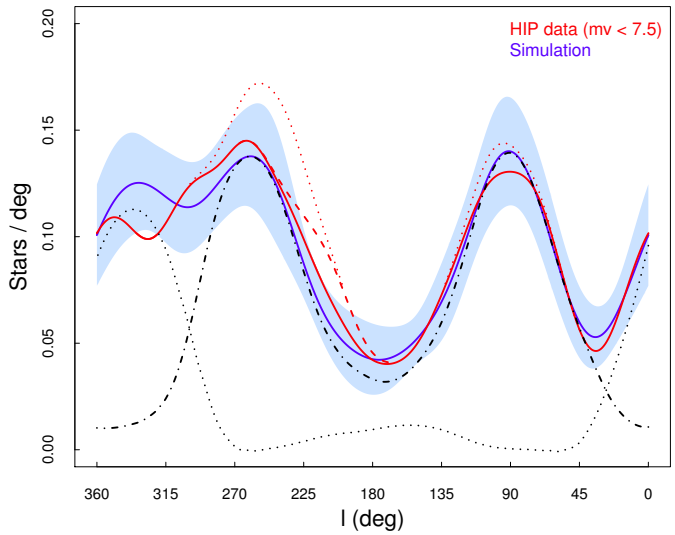

Figure 3.7: Longitude distribution of the HIP2 OB stars. Meaning of the curves are as in the previous figure .

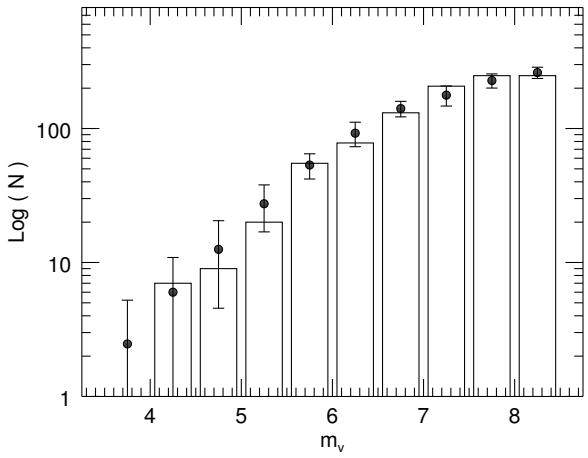

Figure 3.8: Apparent magnitude distribution for the data (histogram) and the simulations (black dots). The error bars show 2 σ uncertainty, calculated with 30 simulated samples.

toward the Galactic anti-center. It should also be noted that, for both the longitude and latitude distributions, the presence or absence of a warp (modelled as described in Section 3.1) has very little effect.

The careful reader will note that our approach assumes that the Hess diagram is independent of position in the Galaxy. We recognize this as a deficit in our model, as the spiral arms are in fact star formation fronts, in general moving with respect to galactic rotation. We thus expect

offsets between younger and older populations, meaning that the Hess diagram will be position dependent. However, if the Sun is close to co-rotation, as expected, such offsets are minimal.

3.4 Completeness

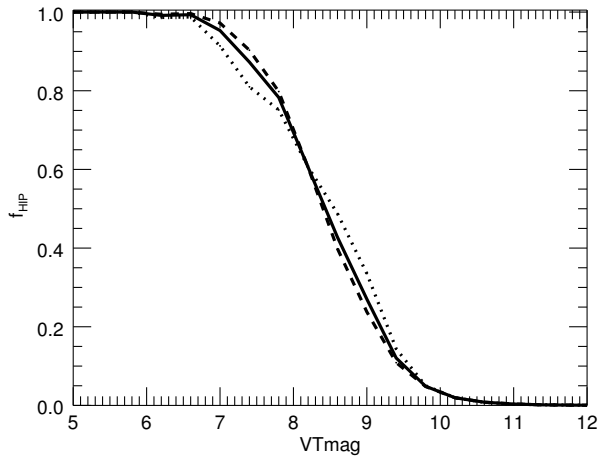

Figure 3.9: Fraction of *Hipparcos* completeness in function of apparent magnitude V_T with respect to the Tycho-2 catalogue. The dashed and the dotted line represent, respectively, the *Hipparcos* fraction for the stars above and below $\delta = -30^o$.

The completeness of the *Hipparcos* catalogue decreases with apparent magnitude, as shown by the fraction of Tycho-2 stars in the *Hipparcos* catalogue (Figure 3.9). At $V_T \leq 7.5$ the HIP2 catalogue is approximately 90% complete, reaching approximately 50% completeness at $V_T = 8.5$. The fact that the *Hipparcos* catalogue was based on an input catalogue built from then extant ground-based surveys results in inhomogenous sky coverage. In particular we find a north/south dichotomy at Declination $\delta \approx -30^o$. We assume that the completeness fraction of *Hipparcos* stars in function of V_T decreases in a similar way for the Johnson magnitude, i.e. $f_{HIP}(V_T) \approx f_{HIP}(V_J)$.

As already noted in Section 2, TGAS contains only a fraction of the stars in *Hipparcos*. We find that the completeness of TGAS with respect to *Hipparcos* is strongly dependent on the observed magnitude and color of the stars: 50% completeness is reached at $V_J = 6.5$ mag and $B - V = 0$, with the brightest and bluest stars missing from TGAS. This incompleteness is a result of the quality criteria used for constructing TGAS and of the difficulty of calibrating these stars due to their relative paucity. Figure 3.10 shows a map of the TGAS(HIP2) completeness as a function of apparent magnitude and color. The completeness reaches a maximum plateau of about 80%, however this is not uniform across the sky. Due to the scanning strategy of the *Gaia* satellite, and limited number of months of observations that have contributed to the DR1, some parts of

the sky are better covered than others. This results in a patchy coverage, which we have not yet taken into account. However, this random sampling caused by the incomplete scanning of the sky by *Gaia* is completely independent of the stellar properties, so that our TGAS(HIP2) sample should trace the kinematics of the stars in an unbiased way.

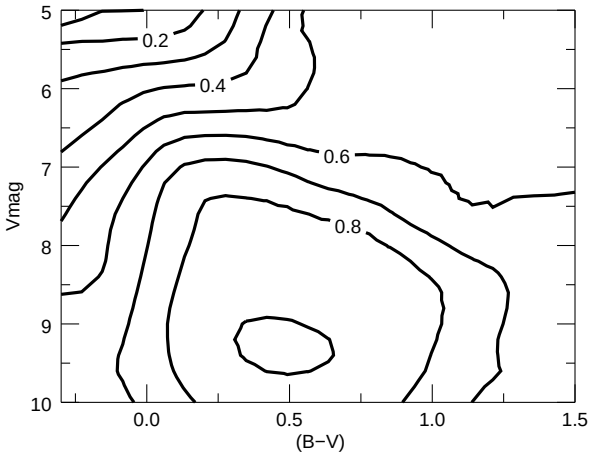

Figure 3.10: Fraction of HIP2 OB stars present in HIP-TGAS as a function of the observed color and the apparent magnitude.

3.5 Kinematics

Now that the spatial distribution has been satisfactorily modelled, we can address the observed distribution of proper motions. We point out that the kinematic model described in this Section is independent from the inclusion (or not) of the warp-induced offset in latitude proper motions (Section 3.1). We adopt a simple model for the velocity dispersions along the three main axes of the velocity ellipsoid: $\sigma_{(1,2,3)} = \sigma^0_{(1,2,3)} exp\Big((R_\odot - R)/2h_R\Big)$, where $h_R = 2.3$ kpc is the radial scale length and $\sigma^0_{(1,2,3)} = (14.35, 9.33, 5.45)$km s^{-1} are the three velocity dispersions in the solar neighborhood for the bluest stars (Dehnen and Binney, 1998). A vertex deviation of $l_v = 30^o$ is implemented, as measured by Dehnen and Binney (1998) for the bluest stars, although we find that it has no significant impact on the proper motion trends.

As recommended by Bland-Hawthorn and Gerhard (2016), we adopted $\Theta_0 = 238$km s^{-1} for the circular rotation velocity at the Solar radius R_0. Given that current estimates of the local slope of the rotation curve varies from positive to negative values, and that our data is restricted to heliocentric distances of a few kpc, we assume a flat rotation curve. In any case, we have verified that assuming a modest slope of ±5 km/s/kpc does not significantly impact the expected

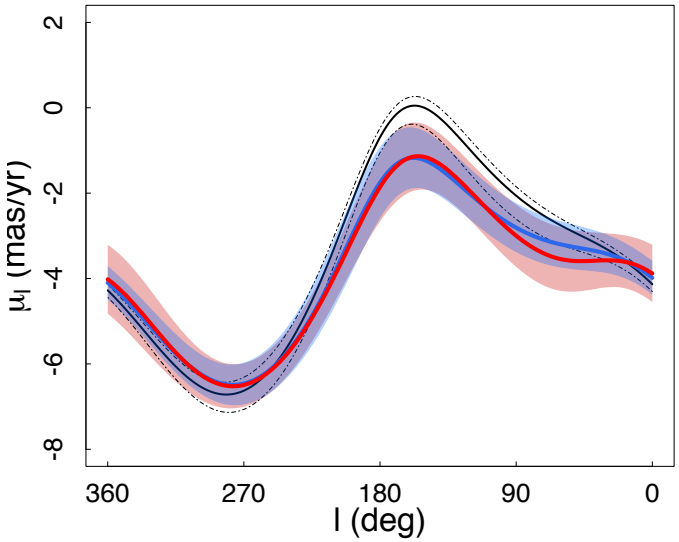

Figure 3.11: μ_l in function of Galactic longitude for the data (red curve) together with the 95% bootstrap confidence band (pink shaded area). The three black dotted curved show the trend obtained with simulations with circular velocity 260, 238 and 220 km/s, respectively, from the lowest to the highest curve. Simulations with an additional velocity to the Local Arm (see text) produce the blue curve, for which the light blue shaded area shows the 2 σ confidence band, calculated with 30 simulated catalogues.

trend in proper motions. We assume no asymmetric drift with respect to the Local Standard of Rest, given that we are modeling young objects.

After local stellar velocities (U,V,W) of the stars are generated, proper motions are calculated assuming a Solar velocity of $v_\odot = (U_\odot, V_\odot, W_\odot) = (11.1, 12.24, 7.25)\,\mathrm{km\ s^{-1}}$ (Schönrich et al., 2010). Observed proper motions in (α,δ) are derived by adding random errors as per an astrometric error model, described in the Section 3.6. Finally, the proper motions in equatorial coordinates are converted to galactic coordinates, ie. (μ_l*, μ_b), where $\mu_l* = \mu_l \cos b$.

Figure 3.11 shows the derived proper motions in galactic longitude for both the data and simulations; the curves in the plot are obtained using the bivariate local-constant (i.e. Nadaraya-Watson) kernel regression implemented by the *npregbw* routine in the *np* R package with bandwidth $h = 45^o$. The solid black line shows the trend obtained for the simulation with the above listed standard parameters. Our simple model of Galactic rotation fails to reproduce the observations, even if we assume Θ_0 = 220 or 260 $\mathrm{km\ s^{-1}}$ (upper and lower dash-dotted black lines, respectively). We also tried modifying the $(U_\odot, V_\odot, W_\odot)$ components of the solar motion (equivalent to adding a systematic motion to the LSR), but without satisfactory results (see Section 3.5.1). We finally obtained a satisfactory fit by assigning to the stars associated with the Local Arm an additional systematic velocity of $\Delta V_C = 6\,\mathrm{km\ s^{-1}}$ in the direction of Galactic rotation and $\Delta V_R = 1\,\mathrm{km\ s^{-1}}$ in the radial direction. Such a systematic velocity could be inherited

from the gas from which they were born, which will deviate from pure rotation about the galactic center thanks to post-shock induced motions associated with the Local Arm feature. Similar, but different, systematics may be at play for the other major spiral arms, which we have not tried to model given the limited volume that is sampled by this *Hipparcos* derived dataset. In any case, the addition (or not) of these systematic motions parallel to the Galactic plane does not significantly influence the proper motions in galactic latitude, as discussed in Chapter 4.

The International Celestial Reference Frame (ICRF) is the practical materialization of the International Celestial Reference System (ICRS) and it is realized in the radio frequency bands, with axes intended to be fixed with respect to an extragalactic intertial reference frame. The optical realization of the ICRS is based on *Hipparcos* catalogue and is called *Hipparcos* Celestial Reference Frame (HCRF). van Leeuwen (2008) found that the reference frame of the new reduction of *Hipparcos* catalogue was identical to the 1997 one, aligned with the ICRF within 0.6 mas in the orientation vector (all 3 components) and within 0.25 mas/yr in the spin vector ω (all 3 components) at the epoch 1991.25. It is evident that a non-zero residual spin of the HCRF with respect to the ICRF introduces a systematic error in the *Hipparcos* proper motions. Depending on the orientation and on the magnitude of the spin vector, the associated systematic proper motions can interfere or amplify a warp signature and must therefore be investigated and taken into account (Abedi et al., 2015; Bobylev, 2010, 2015). In the following section, when modelling the HIP2 sample, we consider the effects of such a possible spin, adding the resulting systematic proper motions to the simulated catalogues following Equation 18 of Lindegren and Kovalevsky (1995), and using the residual spin vector $(\omega_x, \omega_y, \omega_z) \simeq (-0.126, +0.185, +0.076)\,\mathrm{mas\,yr^{-1}}$ as measured by *Gaia* (Lindegren, L. et al., 2016).

3.5.1 Additional tests to reproduce the observed trends in μ_l vs l

In this Subsection, we present some tests that we performed to reproduce with our model the observed trends in the proper motions μ_l as a function of Galactic longitude l. To that end, we assumed different values for the slope of the rotation curve of the Galaxy (see Figure 3.12) and the values of the Solar motion (see Figure 3.13). Moreover, as already reported in Section 3.5, we also tested the impact of different values of circular velocity (see Figure 3.11). Notwithstanding our efforts in tuning the parameters of our model, we failed to reproduce the data with our simulated catalogues. However, the observed trends are satisfactorily reproduced if we assign to the stars of the Local Arm an additional systematic velocity, as explained in Section 3.5.

3.6 Error model

Our approach to confronting models with observations is to perform this comparison in the space of the observations. Fundamental to this approach is having a proper description (i.e. model) of the uncertainties in the data. For this purpose we construct an empirical model of the astrometric

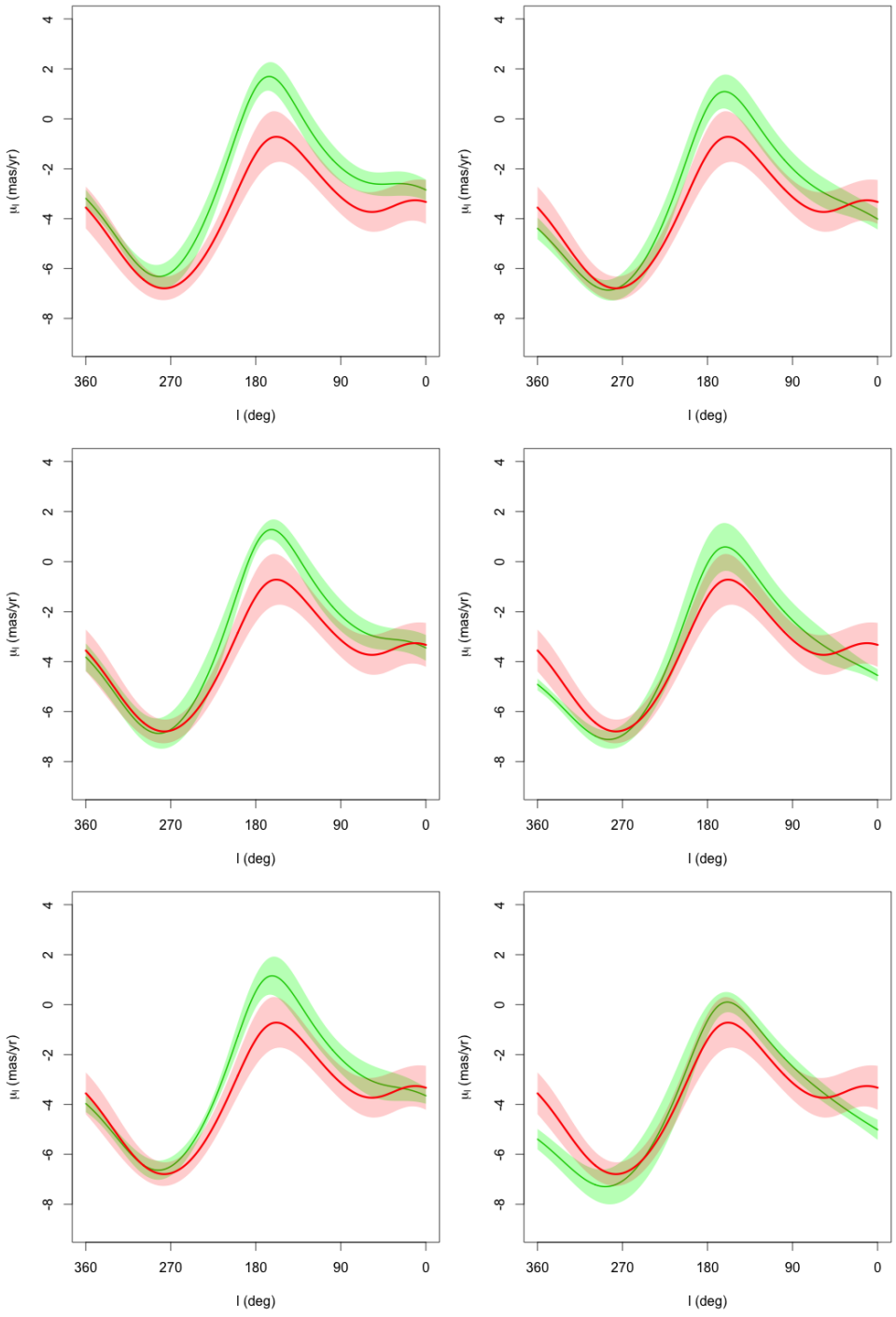

Figure 3.12: μ_l in function of Galactic longitude for the data (red curve) together with the 95% bootstrap confidence band (pink shaded area). The different panels present some examples of the obtained trends with the simulated catalogues (green curve) assuming different slopes of the Galactic rotation curve, namely: *left column, from top to bottom*: $-7, -4, -3$ km/s/kpc; *right column, from top to bottom*: $0, +3, +7$ km/s/kpc.

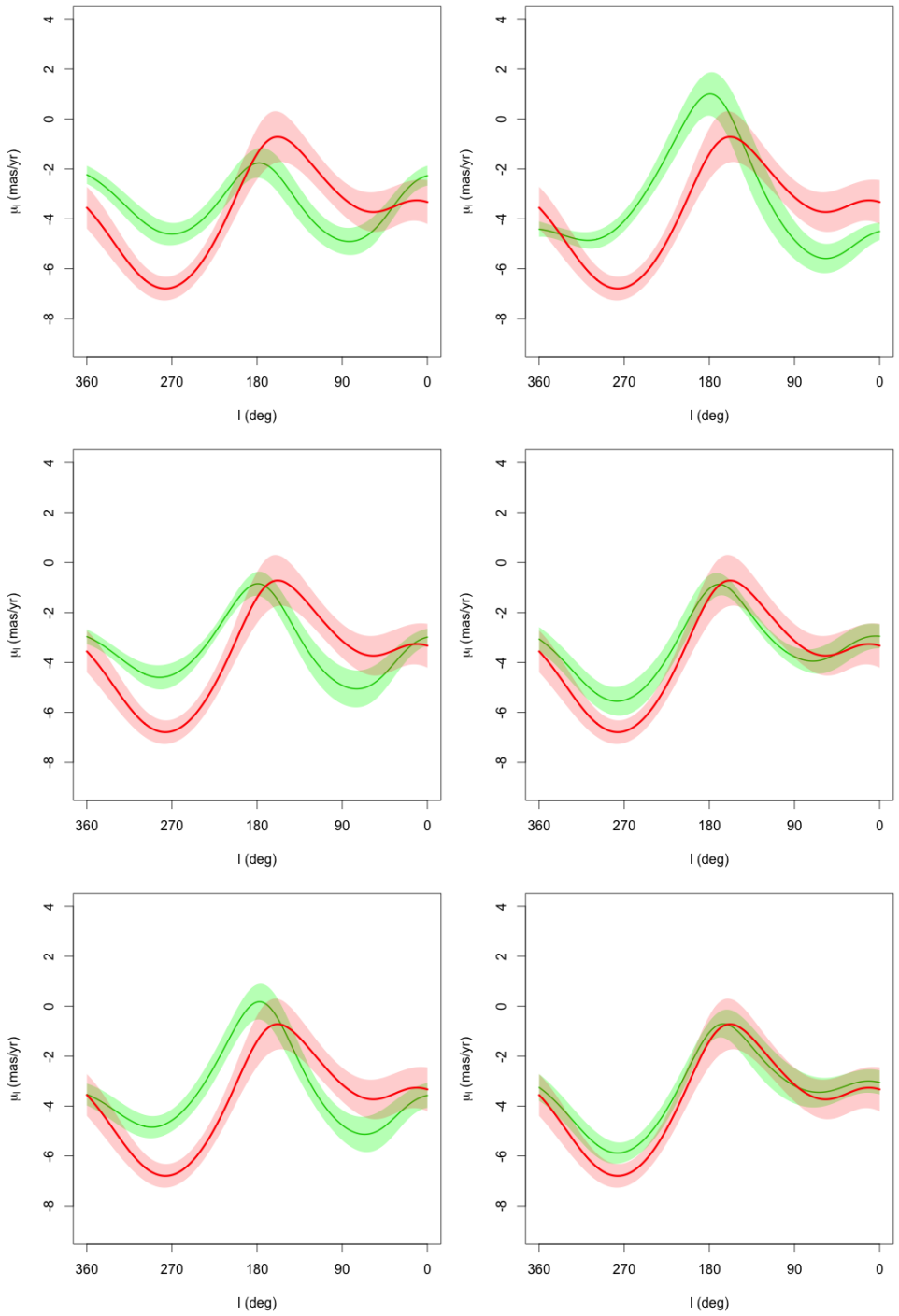

Figure 3.13: Same as Figure 3.12, but varying the values of the Solar motion in the Galactic plane. *Left column, from top to bottom*: $(U_\odot, V_\odot) = (0,0)$ km/s, $(U_\odot, V_\odot) = (0,5)$ km/s, $(U_\odot, V_\odot) = (0,10)$ km/s. *Right column, from top to bottom*: $(U_\odot, V_\odot) = (0,15)$ km/s, $(U_\odot, V_\odot) = (5,5)$ km/s, $(U_\odot, V_\odot) = (7,5)$ km/s.

uncertainties in our two samples from the two catalogues themselves. Below we first describe the astrometric error model for the HIP2 sample, based on the errors in the HIP2 catalogue, and then that of the TGAS(HIP2) sample based on the error properties of the *Hipparcos* subsample in *Gaia* DR1. We note that, while we are here principally interested in the proper motions, we must also model the uncertainties of the observed parallaxes ϖ since we have applied the selection criteria $\varpi < 2$ mas to arrive at our OB samples, and this same selection criteria must therefore be applied to any synthetic catalogue to be compared to our sample.

3.6.1 *Hipparcos* error model

It is known that the *Hipparcos* astrometric uncertainties mainly depend on the apparent magnitude (i.e. the S/N of the individual observations) and on the ecliptic latitude as a result of the scanning law of the *Hipparcos* satellite, which determined the number of times a given star in a particular direction on the sky was observed. These dependencies are not quantified in van Leeuwen (2008), which only reports the *formal* astrometric uncertainties for each star. To find the mean error of a particular astrometric quantity as a function of apparent magnitude and ecliptic latitude we selected the stars with $(B-V) < 0.5$ from the HIP2 catalogue, consistent with the color range of our selected sample of OB stars. We then bin this sample with respect to apparent magnitude and ecliptic latitude and find, for each bin, the median errors for right ascension α, declination δ, parallax ϖ, proper motions $\mu_{\alpha*}$ and μ_δ. The resulting Tables (Table 3.2, 3.3, 3.4, 3.5 and 3.6) are described in Section 3.6.1.1, which gives further details on their construction.

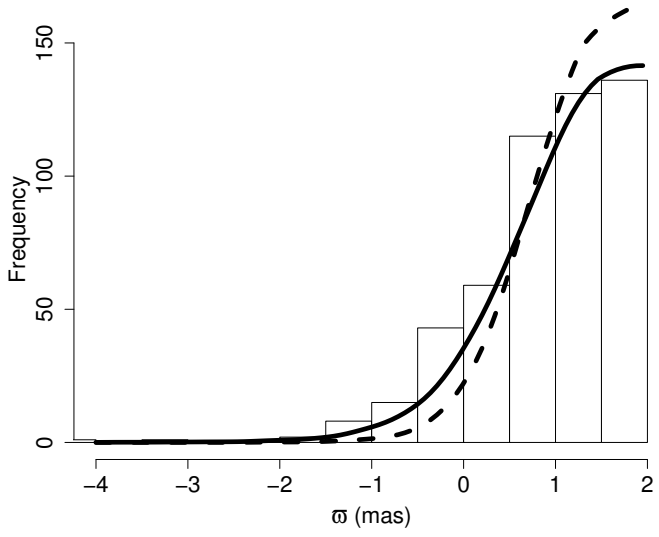

Figure 3.14: The histogram shows the observed parallax distribution. The dashed and the solid curves show, respectively, the synthetic distributions with F=1 and 1.5 (see text for explanation).

However, before using these formal HIP2 uncertainties to generate random errors for our simulated stars, we first evaluate whether the formal errors adequately describe the actual

accuracy of the astrometric quantities. For this purpose the distribution of observed parallaxes is most useful, and in particular the tail of the negative parallaxes, which is a consequence of the uncertainties since the true parallax is greater than zero. In fact, using the mean formal uncertainties in the parallax to generate random errors, we are unable to reproduce the observed parallax distribution in our sample (see Figure 3.14). Assuming that our model correctly describes the true underlying distance distribution, we find that the formal HIP2 uncertainties must be inflated by a factor of $F = 1.5$ to satisfactorily reproduce the observed distribution. This factor F is then also applied to the mean formal uncertainties of the other astrometric quantities. We note that this correction factor is larger than that implied from an analysis of the differences between the *Hipparcos* and *Gaia* DR1 parallaxes. (See Appendix B of Lindegren, L. et al. (2016).)

To better fit the HIP2 proper motion distributions we also take into consideration stellar binarity. Indeed, approximately $f_b \approx 20\%$ of stars of our sample has been labelled as binary, either resolved or unresolved, in the HIP2 catalogue. For these stars, the uncertainties are greater than for single stars. Therefore, we inflate the proper motion errors for a random selection of 20% of our simulated stars by a factor of $f_{bin} = 1.7$ to arrive at a distribution in the errors comparable to the observed one. Finally, we also performed similar statistics on the correlations in the HIP2 astrometric quantities published by van Leeuwen (2008), using the four elements of the covariance matrix relative to the proper motions (see Appendix B of Michalik et al., 2014). We find that the absolute median correlations are less than 0.1, and therefore we do not take them into account.

3.6.1.1 Hipparcos astrometric errors

Tables 3.2, 3.3, 3.4, 3.5 and 3.6 show the median formal errors of right ascension α, declination δ, parallax ϖ, proper motion components μ_α and μ_δ in function of apparent magnitude and ecliptic latitude for the HIP2 stars. They were obtained considering the entire HIP2 catalogue (as given by van Leeuwen, 2008) excluding the stars redder than $(B-V) = 0.5$. We also excluded stars for which there was a claim of binarity in van Leeuwen (2008), taking account for binary systems after the single stars errors are generated, as described in the text. To construct the tables, we binned the resulting sample of 15197 HIP2 stars with respect to apparent magnitude and ecliptic latitude and found the median errors for each bin. Table 3.7 shows the number of objects in each bin.

3.6.2 TGAS(HIP2) error model

A detailed description of the astrometric error properties of the TGAS subset in *Gaia* DR1 is described in Lindegren, L. et al. (2016). However, on further investigation we found that the error properties of the subset of 93635 *Hipparcos* stars in *Gaia* DR1 are significantly different with respect to the larger TGAS sample. In particular, we find that the zonal variations of the median uncertainties seen with respect to position on the sky are much less prominent for the

Table 3.2: Median formal uncertainties for σ_α.

	Ecliptic latitude ($\|\beta\|$, (deg))						
m_V	0-10	10-20	20-30	30-40	40-50	50-60	60-90
3-4	0.22	0.19	0.40	0.23	0.12	0.11	0.20
4-5	0.24	0.25	0.25	0.20	0.15	0.16	0.15
5-6	0.34	0.32	0.31	0.27	0.21	0.19	0.20
6-7	0.49	0.46	0.44	0.37	0.29	0.29	0.29
7-8	0.66	0.64	0.60	0.51	0.40	0.39	0.40

Table 3.3: Median formal uncertainties for σ_δ.

	Ecliptic latitude ($\|\beta\|$, (deg))						
m_V	0-10	10-20	20-30	30-40	40-50	50-60	60-90
3-4	0.16	0.12	0.31	0.19	0.12	0.13	0.26
4-5	0.16	0.18	0.18	0.17	0.17	0.17	0.16
5-6	0.23	0.22	0.23	0.24	0.23	0.21	0.21
6-7	0.32	0.32	0.33	0.32	0.32	0.31	0.29
7-8	0.44	0.44	0.44	0.44	0.45	0.42	0.40

Table 3.4: Median formal uncertainties for σ_ϖ.

	Ecliptic latitude ($\|\beta\|$, (deg))						
m_V	0-10	10-20	20-30	30-40	40-50	50-60	60-90
3-4	0.20	0.19	0.19	0.21	0.16	0.13	0.14
4-5	0.25	0.26	0.25	0.23	0.24	0.19	0.16
5-6	0.36	0.34	0.35	0.34	0.33	0.26	0.22
6-7	0.51	0.51	0.49	0.47	0.47	0.38	0.31
7-8	0.71	0.70	0.69	0.66	0.66	0.53	0.45

Hipparcos stars in DR1, and are only weakly dependent on ecliptic latitude. The parallax errors with respect to ecliptic latitude are shown in Figure 3.15. The TGAS(HIP2) parallax errors show no apparent correlation with respect to magnitude or color. Figure 3.16 shows the distribution of parallax uncertainties for three ecliptic latitude bins, which we model with a gamma distribution having the parameters reported in Table 3.8. However, Lindegren, L. et al. (2016) has warned that there is an additional systematic error in the parallaxes at the level of 0.3 mas. In this work we only use the parallaxes to split our sample in two subsets, and we have verified that adding an additional systematic error of 0.3 mas to account for these possible systematic errors does not affect our results.

The errors for the proper motions also show a weak dependence on ecliptic latitude, as well as

Table 3.5: Median formal uncertainties for $\sigma_{\mu_{\alpha*}}$.

	Ecliptic latitude ($\|\beta\|$, (deg))						
m_V	0-10	10-20	20-30	30-40	40-50	50-60	60-90
3- 4	0.24	0.22	0.18	0.19	0.13	0.12	0.15
4-5	0.28	0.29	0.26	0.21	0.17	0.17	0.16
5-6	0.41	0.37	0.35	0.30	0.24	0.22	0.23
6-7	0.58	0.55	0.50	0.43	0.33	0.32	0.32
7-8	0.80	0.77	0.70	0.60	0.47	0.44	0.45

Table 3.6: Median formal uncertainties for σ_{μ_δ}.

	Ecliptic latitude ($\|\beta\|$, (deg))						
m_V	0-10	10-20	20-30	30-40	40-50	50-60	60-90
3-4	0.16	0.16	0.16	0.18	0.13	0.13	0.15
4-5	0.19	0.20	0.19	0.17	0.18	0.17	0.16
5-6	0.27	0.27	0.26	0.26	0.26	0.24	0.23
6-7	0.37	0.38	0.38	0.36	0.36	0.34	0.33
7-8	0.53	0.53	0.52	0.52	0.52	0.48	0.46

Table 3.7: Number of stars in each bin.

	Ecliptic latitude ($\|\beta\|$, (deg))						
m_V	0-10	10-20	20-30	30-40	40-50	50-60	60-90
3-4	20	20	20	12	17	15	18
4-5	69	65	63	57	61	51	61
5-6	209	193	209	169	167	183	196
6-7	565	550	581	538	522	514	577
7-8	1274	1287	1416	1372	1355	1321	1447

additional dependence with respect to magnitude. Indeed, we find that the proper motion errors for the *Hipparcos* subset in *Gaia* DR1 are strongly correlated with the *Hipparcos* positional errors, as one would expect, given that the *Hipparcos* positions are used to constrain the *Gaia* DR1 astrometric solutions (Michalik et al., 2015) (see Section 2.1). We use this correlation to model the proper motion errors of the *Hipparcos* subsample in DR1. Figure 3.17 show the agreement which results when we take as our model $\sigma_{\mu_\alpha} = C_\alpha \left[F\,\sigma_\alpha^H(m,\beta)/\Delta t\right]$, where F is the correction factor applied to the *Hipparcos* astrometric uncertainties, as described in Section 3.6.1, $\sigma_\alpha^H(m,\beta)$ is the *Hipparcos* error in right ascension, interpolated from table 3.2 in the Appendix, and Δt is the difference between the *Gaia* (J2015) and *Hipparcos* (J1991.25) epoch. The adopted coefficient $C_\alpha = 1.42$ is the median of $\sigma_{\mu_\alpha}/\left[F\,\sigma_\alpha^H(m,\beta)/\Delta t\right]$ for the stars of the TGAS(HIP2) sample. An

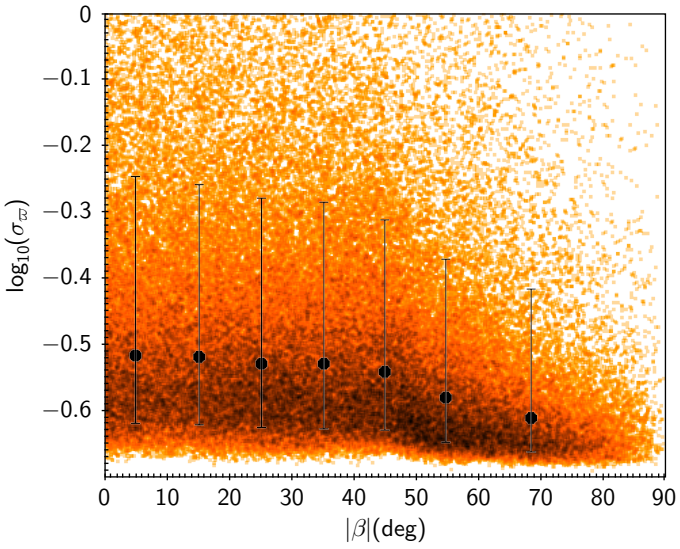

Figure 3.15: Logarithm of the parallax errors (mas) in function of ecliptic latitude for the *Hipparcos* subsample in TGAS. The point show the medians, while the error bars show the 10^{th} and the 90^{th} percentiles of the distribution.

Table 3.8: The shape parameter k and the scale parameter θ of the gamma distributions used to model the $\log_{10}(\sigma_\varpi)$ distributions shown in Figure 3.15). An additional offset is required in order to fit the distributions.

Ecliptic latitude $\lvert\beta\rvert$ (deg)	k	θ	offset
0-40	1.5	0.113	−0.658
40-60	1.2	0.115	−0.658
60-90	1.1	0.08	−0.67

analogous model is used for σ_{μ_δ}, with $C_\delta = 1.44$.

Finally, in contrast to the correlations in the HIP2 sample, we find that the correlations in DR1 between the astrometric quantities of the *Hipparcos* subsample vary strongly across the sky, but are significantly different from the complete TGAS sample, shown in Figure 7 of Lindegren, L. et al. (2016). Figure 3.18 shows the variation across the sky of the correlations between the parallaxes and the proper motions for the *Hipparcos* subset in TGAS. As we can see, the correlations between proper motion components are relevant. To take this into account, we generate the synthetic proper motion errors from a bivariate gaussian distribution with a covariance matrix which includes the σ_{μ_α} and σ_{μ_δ} predicted by the above described model and the correlations from the first map in Figure 3.18, using the simulated (α, δ) positions.

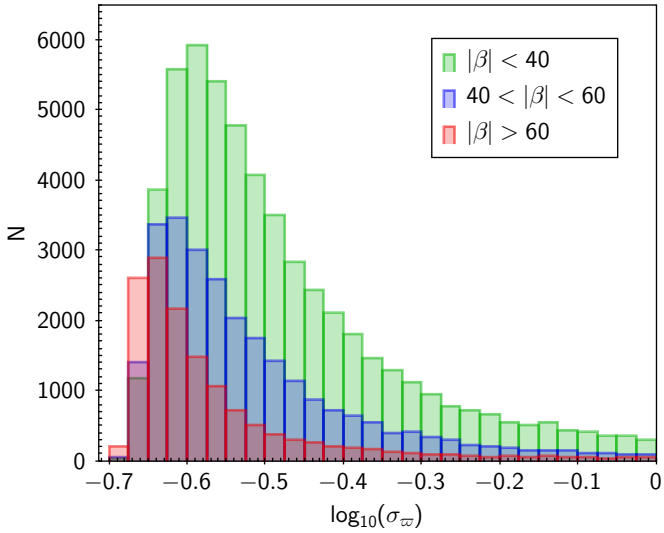

Figure 3.16: Distribution of the logarithm of the parallax uncertainties **(mas)** for the HIP-TGAS stars. Three subsets with different ecliptic latitude are shown.

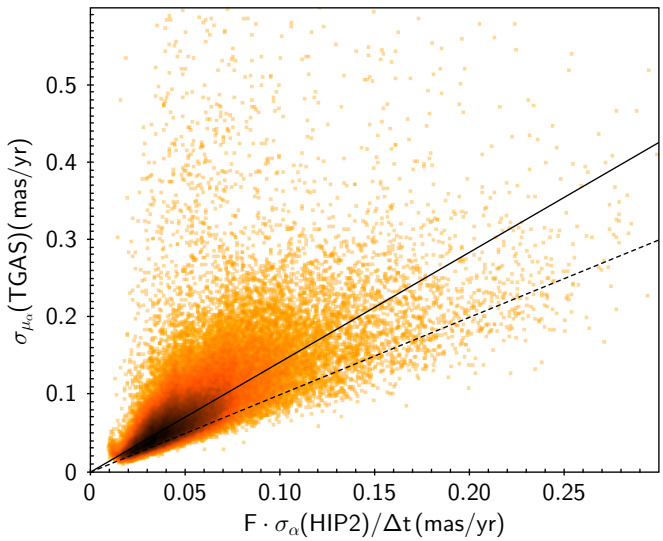

Figure 3.17: For each star of the *Hipparcos* subset in TGAS, the published error $\sigma_{\mu_{\alpha*}}$(TGAS) is compared to the prediction based on *Hipparcos* uncertainties $F\,\sigma_\alpha^H(m,\beta)/\Delta t$ (see text). The dashed line represents the bisector. The solid line has null intercept and coefficient $C_\alpha = 1.42$, which is used to calibrate our error model (see text).

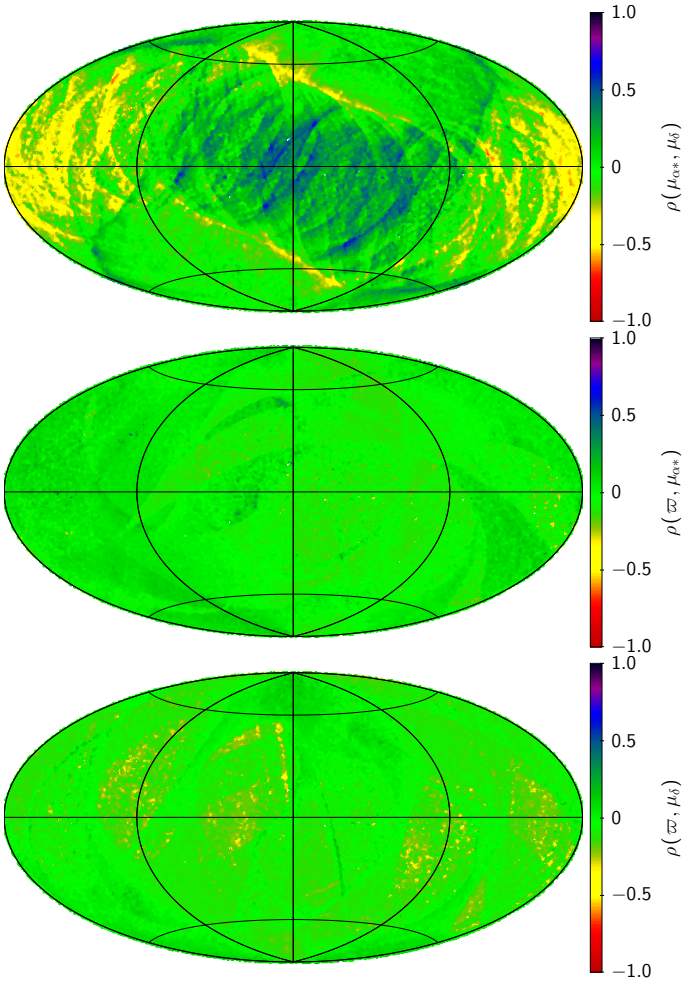

Figure 3.18: Median correlations between parallaxes ϖ and proper motions μ_α, μ_δ in HIP-TGAS.

CHAPTER 4

COMPARING THE MODEL WITH THE DATA

In this Chapter, we compare the observed proper motions of our two samples TGAS(HIP2) and HIP2 with the proper motion distributions derived from models with and without a warp (Section 4.1), with the purpose of determining whether the warp kinematic signature is present in either of our two samples (as discussed in Section 4.2). We adopt a proper motion based analysis, in order to avoid the bias in the systematic vertical motions due to large uncertainties in the distance estimates (as discussed in Appendix B).

4.1 Proper motion μ_b in function of Galactic longitude

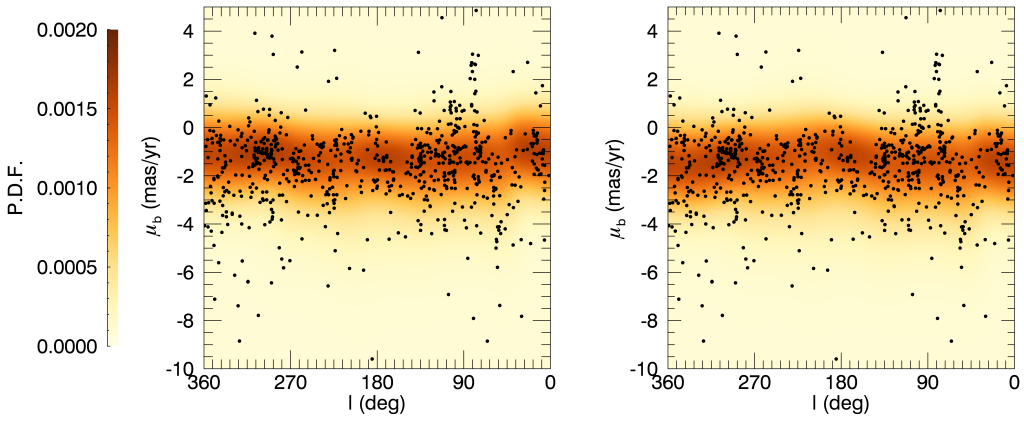

Figure 4.1: Distribution of the TGAS-HIP data in the l-μ_b plane (black dots), together with the Probability Density Function $P(\mu_b|l)$ predicted by the no-warp model (left panel) and the warp model of Yusifov (2004) (right panel).

The aim of the present work is to determine whether a warp is favored over a no-warp model in either of our *Hipparcos* or *Gaia* DR1 samples. In Section 3.1 we showed that the Galactic warp, if stable, results in a distinct trend in the proper motions perpendicular to the galactic plane μ_b with respect to galactic longitude, with higher (i.e. more positive) proper motions toward the Galactic anti-center (see Figure 3.3). Our approach is to compare the distribution of the observed proper motions with the expectations derived from a warp model and a no-warp model, taking into full account the known properties of the astrometric errors. To achieve this we adopt the approach of calculating the likelihood associated with a given model as the probability of the observed data set arising from the hypothetical model (as described in Peacock, 1983).

Given an assumed model (i.e. parameter set), we generate 500 thousand stars and perform a two-dimensional kernel density estimation in $l - \mu_b$ space to derive the conditional Probability Density Function (PDF), $P(\mu_b|l)$, the probability of observing a star with proper motion μ_b at a given galactic longitude, where $P(\mu_b|l)$ is constrained to satisfy $\int P(\mu_b|l)\mathrm{d}\mu_b = 1$. The motivation for using $P(\mu_b|l)$ is that we want to assign the probability of observing a given value of μ_b independent of the longitude distribution of the stars, which is highly heterogeneous. That is, we wish to quantify which model best reproduces the observed trend of the proper motions with respect to longitude. In any case, we also performed the below analysis using $P(l, \mu_b)$, imposing the normalization $\int P(l, \mu_b)\mathrm{d}l\,\mathrm{d}\mu_b = 1$, and obtain similar results. Figure 4.1 shows the conditional PDFs for the warp/no-warp models for the TGAS(HIP2) sample. The PDFs for the HIP2 sample (not shown) are very similar, as the proper motion distribution is dominated by the intrinsic velocity dispersion of our sample rather than by the proper motion errors.

Once the PDFs for the two different models are constructed, we found the probability $P(\mu_{b,i}|l_i)$ associated with each i-th observed star according to each PDF. The likelihood associated with the model is $L = \prod_{i=1}^{N} P(\mu_{b,i}|l_i)$, where N is the total number of stars in our dataset; for computational reasons, we used instead the log-likelihood $\ell = ln(L) = \sum_{i=1}^{N} ln(P(\mu_{b,i}|l_i)$. Also for practical reasons we applied a cut in μ_b, considering only the range $(-10 < \mu_b < 5)$ mas/yr when calculating ℓ, reducing our HIP2 dataset to 989 stars, and our TGAS(HIP2) sample to 791 stars. Below we will confirm that this clipping of the data does not impact our results by considering alternative cuts on μ_b.

For a given sample, the difference between the log-likelihoods of a warp model and the no-warp model (i.e. the ratio of the likelihoods), $\Delta \equiv \ell_{WARP} - \ell_{NOWARP}$, is found as a measure of which model is more likely. We performed a bootstrap analysis of the log-likelihood to quantify the significance level of the obtained Δ. Bootstrap catalogues were generated by randomly extracting stars N times from the observed set of N stars of the dataset (resampling with replacement). As suggested by Feigelson and Babu (2012), $N_B \approx N(\ln N)^2$ bootstrap resamples were generated. For each bootstrap resample, the log-likelihood was computed for the two models and the log-likelihood difference Δ was calculated. Finally, after N_B resamples, the standard deviation σ_Δ of the distribution of Δ is determined, while the integral of the normalized Δ distribution for $\Delta > 0$

gives $P(\Delta > 0)$, the probability of the warp model being favoured over the no-warp model.

Table 4.1: Difference of the log-likelihoods of the warp and nowarp models $\Delta \equiv \ell_{WARP} - \ell_{NOWARP}$ according to the warp parameters reported in Drimmel and Spergel (2001) (dust and stellar model) and Yusifov (2004). Log-likelihoods are calculated with the TGAS(HIP2) sample ($\varpi < 2$ mas), containing 758 stars. The standard deviation σ_Δ and the probability $P(\Delta > 0)$ are calculated using bootstrap resamples (see text).

	$\varpi < 2$ mas		
Warp model	Δ	σ_Δ	$P(\Delta > 0)$
Drimmel and Spergel (2001), dust	-41.24	9.72	0.00
Drimmel and Spergel (2001), stars	-5.47	3.93	0.09
Yusifov (2004)	-2.69	6.99	0.35

Table 4.2: Difference of the log-likelihoods of the warp and nowarp models $\Delta \equiv \ell_{WARP} - \ell_{NOWARP}$ according to the warp parameters reported in Drimmel and Spergel (2001) (dust and stellar model) and Yusifov (2004). Log-likelihoods are calculated for the nearby ($(1 < \varpi < 2)$ mas, 296 objects) and for the distant ($\varpi < 1$ mas, 462 objects) TGAS(HIP2) stars. The standard deviation σ_Δ and the probability $P(\Delta > 0)$ are calculated using bootstrap resamples (see text).

	$(1 < \varpi < 2)$ mas			$\varpi < 1$ mas		
Warp model	Δ	σ_Δ	$P(\Delta > 0)$	Δ	σ_Δ	$P(\Delta > 0)$
Drimmel and Spergel (2001), dust	-2.94	5.04	0.28	-60.35	10.90	0.00
Drimmel and Spergel (2001), stars	3.13	1.92	0.95	-22.54	16.79	0.04
Yusifov (2004)	13.93	3.47	1.00	-10.48	25.81	0.32

Tables 4.1 and 4.2 collects the results for the TGAS(HIP2) dataset for the three different warp models whose parameters are given in Table 3.1, for the full dataset as well as for the two subsets of distant ($\varpi < 1$ mas) and nearby ($2 > \varpi > 1$ mas) stars. For the full dataset none of the warp models are favored over a no-warp model, though the model of Yusifov (2004) cannot be excluded. However, on splitting our sample into distant and nearby subsamples, we find some of the warp models are clearly favoured over the no-warp model for the nearby stars.

In Tables 4.3, 4.4 and 4.5 we show the results of our analysis, for both the HIP2 and TGAS(HIP2) samples, considering various subsamples with alternative data selection criteria to test for possible effects due to incompleteness and outliers. Separate PDFs were appropriately generated for the selections in magnitude and parallax. Here we show the results using the Yusifov (2004) model, as it is the most consistent with the data, as indicated by the the maximum likelihood measurements shown in Tables 4.1 and 4.2. Again, the chosen warp model is not clearly favored nor disfavored until we split our sample into distant and nearby subsamples.

Table 4.3: Difference of the log-likelihoods of the warp (Yusifov, 2004) and nowarp models $\Delta \equiv \ell_{WARP} - \ell_{NOWARP}$ for the TGAS(HIP2) sample. Results are shown for the whole sample (*All*, $m_v < 8.5$) and for the bright sample ($m_v < 7.5$). We also report the results obtained removing the objects with high ΔQ, where ΔQ is the difference between the TGAS and *Hipparcos* proper motion (Lindegren, L. et al., 2016). $\Delta Q_{95\%} = 23$ and $\Delta Q_{90\%} = 11$ are the percentiles the ΔQ distribution for all the *Hipparcos* subset in TGAS. We also present the results excluding the stars labelled as binaries in van Leeuwen (2008). The 95% (90%) Confidence Interval is obtained considering the stars with proper motions μ_b between the 2.5^{th} and the 97.5^{th} (the 5^{th} and the 95^{th}) percentiles of the whole μ_b distribution (with 767 stars), without restricting to the range ($-10 < \mu_b < 5$) mas/yr (see text). The standard deviation σ_Δ and the probability $P(\Delta > 0)$ are calculated using bootstrap resamples (see text).

	$\varpi < 2$ mas			
sample	N_{stars}	Δ	σ_Δ	$P(\Delta > 0)$
All	758	-2.69	6.99	0.35
$m_v < 7.5$	310	0.68	4.44	0.57
$\Delta Q < \Delta Q_{95\%}$	749	-3.73	6.90	0.30
$\Delta Q < \Delta Q_{90\%}$	690	-7.35	6.56	0.13
No HIP2 binaries	672	-2.75	6.81	0.34
95% Conf. Int.	730	-0.86	5.94	0.44
90% Conf. Int.	692	2.79	4.91	0.72

Various selection criteria were applied to investigate the role of possible outliers in biasing the outcome. We tried to remove the stars identified as binaries in the *Hipparcos* catalogue (van Leeuwen, 2008) and, for the TGAS subset, the objects with a high difference between the *Gaia* and *Hipparcos* proper motion (Lindegren, L. et al., 2016). We also removed the high-proper motion stars (i.e. the tails in the μ_b distributions), to exclude possible runaway stars or nearby objects with significant peculiar motions. As shown in Tables 4.3, 4.4 and 4.5, the exclusion of these possible outliers doesn't change our findings, confirming that the warp model (Yusifov, 2004) is preferred for the nearby objects, but rejected for the distant stars.

A further test was performed, removing the most obvious clumps in the l, b and in the l, μ_b space (for example the one centered on $l \approx 80^o$ and $\mu_b \approx 2.5$ mas/yr, see Figure 4.1), to study the effect of the intrinsic clumpiness of the OB stars. We also removed the stars part of the known OB association Cen OB2 according to de Zeeuw et al. (1999). The obtained results (here not shown) are very similar to the ones in Tables 4.3, 4.4 and 4.5.

Table 4.4: Same as Table 4.4, but dividing the data into distant ($\varpi < 1$ mas) and nearby ($2 > \varpi > 1$ mas) stars.

	$(1 < \varpi < 2)$ mas				$\varpi < 1$ mas			
sample	N_{stars}	Δ	σ_Δ	$P(\Delta > 0)$	N_{stars}	Δ	σ_Δ	$P(\Delta > 0)$
All	296	13.93	3.47	1.00	462	-10.48	25.81	0.32
$m_v < 7.5$	129	4.59	2.09	0.99	181	-0.47	4.03	0.45
$\Delta Q < \Delta Q_{95\%}$	293	13.86	3.50	1.00	456	-11.54	25.89	0.31
$\Delta Q < \Delta Q_{90\%}$	257	10.97	3.07	1.00	433	-12.18	25.93	0.30
No HIP2 binaries	267	15.03	3.40	1.00	405	-11.85	26.27	0.31
95% Conf. Int.	289	10.30	3.23	1.00	444	-13.99	5.23	0.00
90% Conf. Int.	273	9.11	2.71	1.00	420	-10.85	4.13	0.00

Table 4.5: Difference of the log-likelihoods of the warp (Yusifov, 2004) and nowarp models $\Delta \equiv \ell_{WARP} - \ell_{NOWARP}$ for the HIP2 sample. Results are shown for the whole sample (*All*, $m_v < 8.5$) and for the bright sample ($m_v < 7.5$). We also present the results obtained removing the stars labelled as binaries in van Leeuwen (2008). The standard deviation σ_Δ and the probability $P(\Delta > 0)$ are calculated using bootstrap resamples (see text).

HIP2 subset	N_{stars}	Δ	σ_Δ	$P(\Delta > 0)$
All	989	-14.99	6.50	0.01
All No HIP2 binaries	838	-11.86	5.74	0.02
$m_v < 7.5$	498	-1.68	4.47	0.35
$m_v < 7.5$ No HIP2 binaries	404	-2.29	4.21	0.29

4.2 Discussion

We have used models of the distribution and kinematics of OB stars to find the expected distribution of proper motions, including astrometric uncertainties, for two samples of spectroscopically identified OB stars from the New *Hipparcos* Reduction and *Gaia* DR1. The resulting PDFs of the proper motions perpendicular to the galactic plane produced by models with and without a warp are compared to the data via a likelihood analysis. We find that the observed proper motions of the nearby stars are more consistent with models containing a kinematic warp signature than a model without, while the more distant stars are not. Given that the warp signal in the proper motions is expected to remain evident at large distances (see Section 3.1), this result is difficult to reconcile with the hypothesis of a stable warp, and we are forced to consider alternative interpretations.

Keeping in mind that our sample of OB stars is tracing the gas, one possibility is that the warp in the gas starts well beyond the Solar Circle, or that the warp amplitude is so small that no signal is detectable. However, most studies to date suggest that the warp in the stars and in the

dust starts inside or close to the Solar circle, (Derriere and Robin, 2001; Drimmel and Spergel, 2001; Momany et al., 2006; Robin et al., 2008; Yusifov, 2004), while the warp amplitude in the gas at R≈10 kpc (Levine et al., 2006) is consistent with warp models of sufficiently small amplitudes. Indeed, Momany et al. (2006) found an excellent agreement between the warp in the stars, gas and dust using the warp model of Yusifov (2004), the same model that we used in Section 4.1. Another possible scenario is that the warp of the Milky Way is a short-lived/transient feature, and that our model of a stable warp is not applicable. This hypothesis would be consistent with the finding that the warp structure may not be the same for all Milky Way components, as argued in Robin et al. (2008), but in contradiction to the findings of Momany et al. (2006) cited above. Finally, our expected kinematic signature from a stable warp could be overwhelmed, or masked, by other systematic motions. Evidence has been found for vertical oscillations (Widrow et al., 2012; Xu et al., 2015), suggesting the presence of vertical waves, as well kinematic evidence of internal breathing modes (Williams et al., 2013) in the disc. Both have been attributed as being possibly caused by the passage of a satellite galaxy (Gómez et al., 2013; Laporte et al., 2016; Widrow et al., 2014), while breathing modes could also be caused by the bar and spiral arms (Monari et al., 2015, 2016). If such effects as these are present, then sampling over a larger volume of the Galactic disc will be necessary to disentangle the kinematic signature of the large-scale warp from these other effects. Also, a comparison of the vertical motions of young stars (tracing the gas) and a dynamically old sample could also confirm whether the gas might possess additional motions due to other effects.

We have compared the proper motions of our two samples with the expectations from three warp models taken from the literature. Among these the model based on the FIR dust emission (Drimmel and Spergel, 2001) can be excluded based on the kinematic data from *Gaia* DR1 that we present here. In addition, the Drimmel and Spergel (2001) dust warp model also predicts a vertical motion of the LSR of 4.6 km s^{-1}, which would result in a vertical solar motion that clearly inconsistent the measured proper motion of Sag A^* (Reid, 2008). This calls into question the finding of Drimmel and Spergel (2001) that the warp in the dust and stars are significantly different. However, the proper motion data does not strongly favor the other two warp models, that of Yusifov (2004) and Drimmel and Spergel (2001) based on the stellar NIR emission: As pointed out in Section 3.1, the local kinematic signature produced by a warp model with $\phi_w \neq 0$ is quite similar to that of a warp model with $\phi_w = 0$ of smaller amplitude. In short, the parameters of even a simple symmetric warp cannot be constrained from local kinematics alone. In any case, we stress that the observed kinematics of the most distant OB stars are not consistent with any of the warp models.

Our search for a kinematic signature of the Galactic warp presented here is a preliminary study that adopts an exploratory approach, aimed at determining whether there is evidence in the *Gaia* DR1 and/or in the pre-*Gaia* global astrometry of the New *Hipparcos* Reduction. While unexpected, our finding that distant OB stars do not evidence the kinematic signature of the

warp is in keeping with the previous results of Smart et al. (1998) and Drimmel et al. (2000), who analyzed the original *Hipparcos* proper motions using a simpler approach than employed here.

We point out that this work only considers a small fraction of the *Gaia* DR1 data with a full astrometric solution, being restricted to a subset of Hipparcos stars in DR1 brighter than $m_{V_T} = 8.5$. *Gaia* DR1 TGAS astrometry is complete to about $m_{V_T} = 11$, and potentially will permit us to sample a significantly larger volume of the disc of the Milky Way than presented here. In future work we will expand our sample to a fainter magnitude limit, using selection criteria based on multi-waveband photometry from other catalogues. We will also compare the kinematics of this young population to an older population representative of the relaxed stellar disc.

Understanding the dynamical nature of the Galactic warp will need studies of both its structural form as well as its associated kinematics. *Gaia* was constructed to reveal the dynamics of the Milky Way on a large scale, and we can only look forward to the future *Gaia* data releases that will eventually contain astrometry for over a billion stars. We expect that *Gaia* will allow us to fully characterize the dynamical properties of the warp, as suggested by Abedi et al. (2014, 2015), and allow us to arrive at a clearer understanding of the nature and origin of the warp. At the same time, *Gaia* may possibly reveal other phenomenon causing systematic vertical velocities in the disc of the Milky Way.

Part III

The kinematic signature of the Galactic warp: the TGAS catalogue

CHAPTER 5

OB STARS IN THE TGAS CATALOGUE

Being intrinsically bright, OB stars can be seen to large distances. Therefore, they can be conveniently used to explore of the large scale structures of the disc, such as the Galactic warp. Since they are short-lived, OB stars are expected to trace the motions of the warped gaseous disc (Section 1.3.1), from which they were recently born. In Part II of this Thesis, we searched for the kinematic signature of the Galactic warp using OB stars from the Hipparcos-subset in *Gaia* DR1, whose identification was based on spectral classification (see Section 2.3). We now (Part III of this Thesis, including Chapter 5, 6 and 7) take into consideration the larger and deeper TGAS catalogue (see the introductory Section 2.1). Unfortunately, the selection of OB stars from the TGAS catalogue is far from trivial. Indeed, estimates of stellar parameters (such as effective temperature $T_{\rm eff}$ and surface gravity $\log g$) or spectral classifications are available in the literature only for a small fraction of TGAS stars, and not for the whole sky. We therefore developed a technique that identifies OB star candidates by combining astrometric and photometric measurements via a probabilistic approach, which is described in detail in Section 5.1. With the obtained sample, we perform bayesian inference on the warp kinematic parameters, implementing the fitting routine described in Chapter 6. We present and discuss the results in Chapter 7.

5.1 Selection of OB star candidates in TGAS

We here identify OB star candidates using photometric information (*Gaia* G magnitudes, together with J,H,K_S bands from 2MASS, the 2-Micron All Sky Survey, Skrutskie et al., 2006) as well as astrometric measurements (Galactic latitude b, parallax ϖ and parallax error σ_ϖ). The procedure consists of two main parts, described in the following.

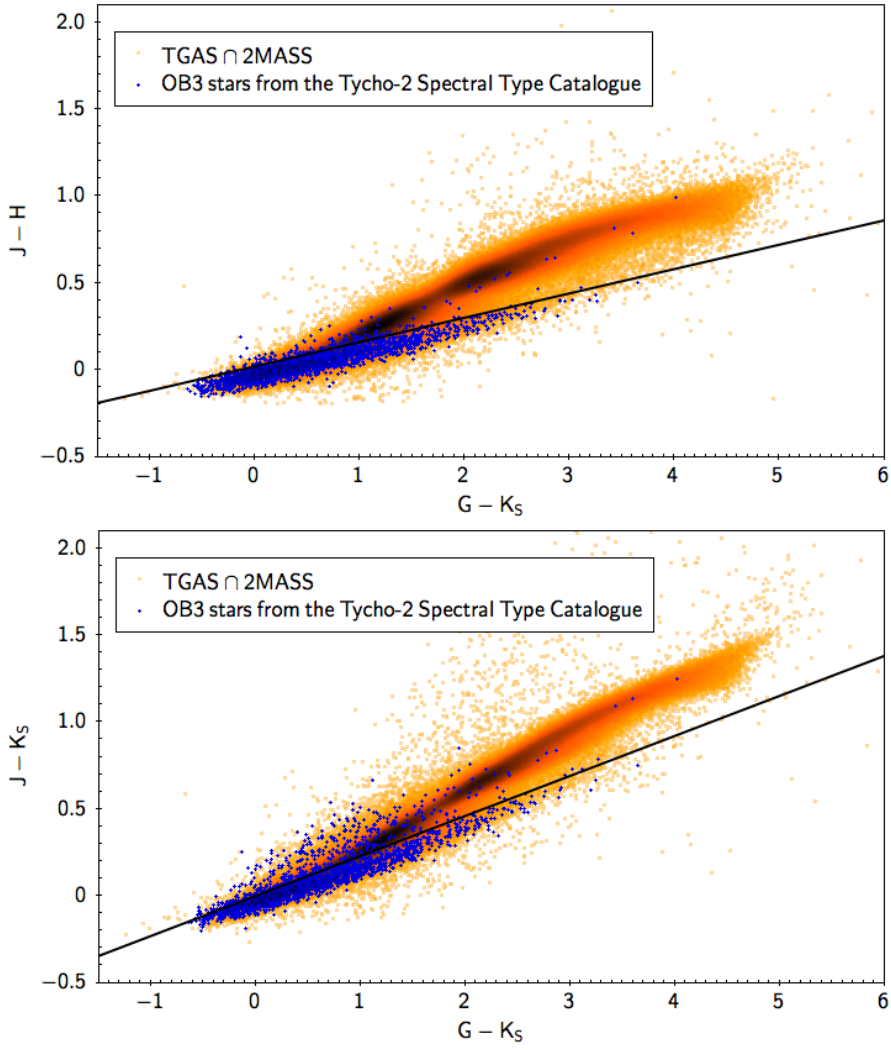

Figure 5.1: The *color-color selection*: TGAS∩2MASS stars (orange dots, darkness proportional to the density) located below the line are selected. To pass the selection, stars must satisfy this criterium on both the plots shown above. This condition is fulfilled for 95% of the OB3 stars (blue crosses) in the Tycho-2 Spectral Type Catalogue (T2STC Wright et al., 2003).

Color-color selection. The first part of the selection process is only based on measured 2MASS/*Gaia* colors. Figure 9.1 shows the 2 054 444 TGAS stars with available magnitudes in J,H,K_S band from 2MASS. Overplotted, OB3 stars from the Tycho-2 Spectral Type Catalogue (hereafter T2STC, Wright et al., 2003). As we can see, the OB stars lie along a sequence that is a consequence of interstellar reddening, and below the primary sequence of stars belonging to other stellar populations. This can be further confirmed by the sources also found in LAMOST (Zhao et al., 2012) and classified as OB stars and K giants from Liu et al. (2014) (shown in Figure 5.2). For instance, the dense region centered at $G - K_S \approx 2.2$, $J - H \approx 0.5$ (upper panel in Figure

9.1 and 5.2) and $G-K_S \approx 2.2$, $J-K \approx 0.7$ (lower panel in Figure 9.1 and 5.2) corresponds to the red clump. Based on these considerations, we select the stars below the black line in both plots of Figure 9.1, i.e. the stars satisfying both $(J-H) < 0.14 \cdot (G-K_S) + 0.02$ (upper panel in Figure 9.1) and $(J-K_S) < 0.23 \cdot (G-K_S)$ (lower panel in Figure 9.1), namely 312 472 TGAS∩2MASS stars. The two color-color criteria adopted here are combined in order to minimize the contamination due to photometric noise. Moreover, stars with bad photometric measurements are removed according to the criterium of Drimmel et el. (in prep.), namely $(J-H) < -0.2$ or $(H-K_S) < -0.2$, obtaining 312 119 stars. From this point on, we will refer to this first part as *color-color selection*.

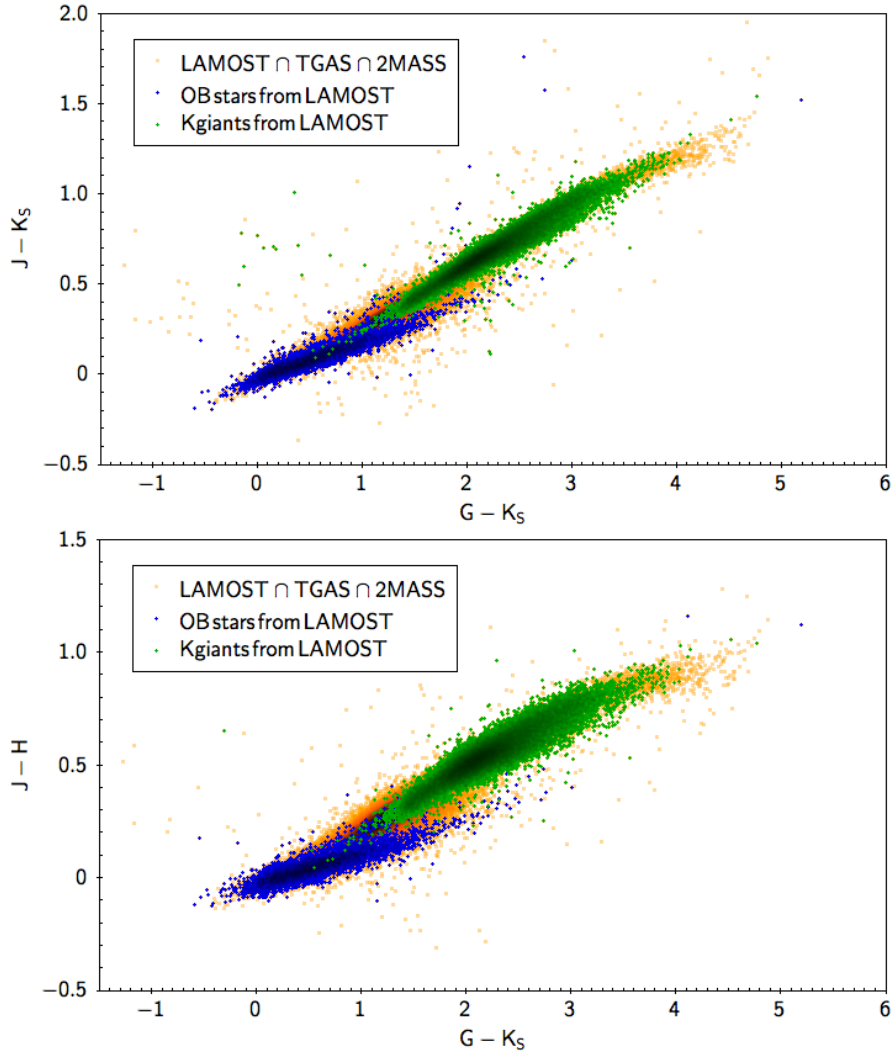

Figure 5.2: For illustrative purposes, we show LAMOST OB and K giant stars (Liu et al., 2014) on the same color-color plots as Figure 9.1.

Parallax criterium. A second selection procedure is then followed using astrometric information. We adopt a probabilistic approach aimed at picking the *color-color selected* stars for which

the inferred absolute magnitude is consistent with being an OB star. To this end, we first calculate the probability density function (pdf) of the heliocentric distance r for each *color-color selected* star. We adopt a simple prior [1] which assumes an exponential scale height and an exponential fall-off with heliocentric distance (similarly to that suggested by Bailer-Jones, 2015)

$$P(r|b) \propto \begin{cases} r^2 e^{-|r\sin b|/h_z} e^{-(r\cos b)/L_R}, & \text{if } r > 0 \\ 0, & \text{otherwise} \end{cases} \tag{5.1}$$

having two different scale lengths for the two directions perpendicular and parallel to the Galactic plane, namely $z = r\sin b$ and $R = r\cos b$. For our selection we assume $h_z = 150$ pc and $L_R = 3.5$ kpc. Our choice for h_z here is larger than the known scale height for this population (see Chapter 3), but is such to remove only the stars whose parallaxes and apparent magnitudes are obviously not consistent with the star being an OB star, though not so small as to condition the distribution of selected stars on the sky. According to Bayes' theorem

$$p(r|b,\varpi,\sigma_\varpi) \propto P(r|b) \cdot P(\varpi|r,\sigma_\varpi) \quad , \tag{5.2}$$

we obtain the unnormalized posterior probability distribution for the heliocentric distance $p(r|b,\varpi,\sigma_\varpi)$ as a product of the prior $P(r|b)$ in Equation 9.1 and a gaussian likelihood

$$P(\varpi|r,\sigma_\varpi) = \frac{1}{\sqrt{2\pi}\sigma_\varpi} \exp\left[\frac{1}{2\sigma_\varpi^2}\left(\varpi - \frac{1}{r}\right)^2\right] \quad . \tag{5.3}$$

From the pdf of the heliocentric distance $p(r|b,\varpi,\sigma_\varpi)$ we can derive for each star the pdf for the extincted absolute magnitude $M_G + A_G$, where M_G is the absolute magnitude and A_G the extinction in the G band, performing the following change of variable:

$$p(M_G + A_G|b,\varpi,\sigma_\varpi,G) = p(r|b,\varpi,\sigma_\varpi)\left|\frac{d(r|G)}{d(M_G+A_G)}\right| \quad , \tag{5.4}$$

where $M_G + A_G = G - 5\log r_{pc} + 5$ (see Figure 5.3). The Jacobian of the transformation can be written only when the G magnitude is fixed. We define the probability of the source being an OB star as follows:

$$p(OB\,|\,b,\varpi,\sigma_\varpi,G) = \int_{-\infty}^{(M_G+A_G)_{lim}} p(M_G + A_G|b,\varpi,\sigma_\varpi,G)\,d(M_G+A_G) \quad , \tag{5.5}$$

which is the probability of the star being brighter than a fixed limit $(M_G + A_G)_{lim}$, as shown in Figure 5.3. After numerically imposing the normalization condition

$$\int_{-\infty}^{+\infty} p(M_G + A_G|b,\varpi,\sigma_\varpi,G)\,d(M_G+A_G) = 1 \quad , \tag{5.6}$$

we select the stars for which $p(OB\,|\,b,\varpi,\sigma_\varpi,G) > 50\%$. The limit $(M_G + A_G)_{lim}$ represents the faintest extincted magnitude that we are willing to tolerate for an OB star candidate, and is

[1] A more sophisticated prior will be explored in Chapter 9.

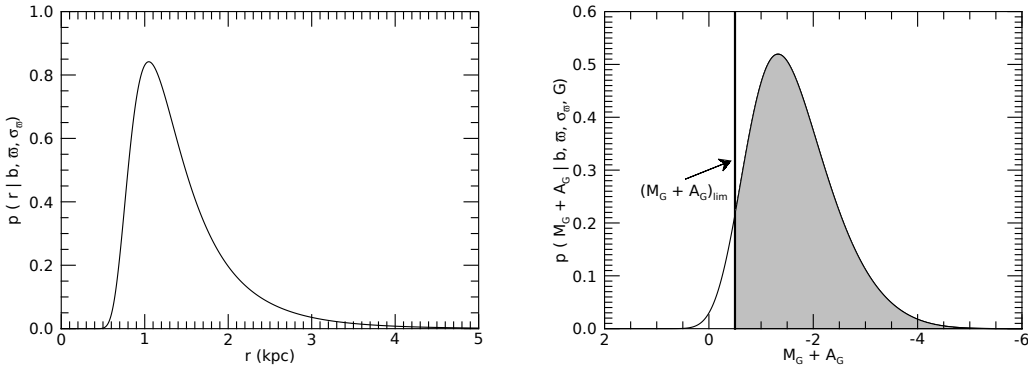

Figure 5.3: An illustrative example on the application of the *parallax criterium* to a star with ϖ=1 mas, σ_{ϖ} = 0.3 mas, $b = 0^o$ and $G = 9$. *Left panel*: The obtained pdf for the heliocentric distance r as described in the text. *Right panel*: The corresponding pdf for the extincted absolute magnitude $M_G + A_G$, obtained applying Equation 5.4. In this case, the source is identified as OB star candidate, given that more than 50% of the pdf is brighter than the tolerance limit $(M_G + A_G)_{lim}$ (as shown by the gray shaded area, i.e. the integral in Equation 9.2).

set for each star as described in the following. We use as a benchmark a fictitious star with age log(age/yr) = 6, log(T_{eff}) = 4.27 and solar metallicity [M/H] = 0, which roughly corresponds to a main sequence B1.5 stars (e.g. Flower, 1977; Humphreys and McElroy, 1984). The fictitious star is shown as a black circle in the left panel of Figure 9.2, and becomes a line in the color-magnitude diagram (CMD) on the right panel because of extinction. The plots in Figure 9.2 were obtained using the PARSEC Isochrones[2] (Bressan et al., 2012; Chen et al., 2014, 2015; Tang et al., 2014), which allow us to relate the intrinsic stellar parameters (such as effective temperature, age, luminosity, etc.) to Gaia and 2MASS photometric system once extinction is fixed. In case of no extinction (i.e. $A_v = 0$), the limit defined by our fictitious star corresponds to $(M_G + A_G)_{lim} = -1.3$ and $(G - K_S) = -0.6$. When extinction is present (i.e. for a given value of A_v), the PARSEC Isochrones web interface provides the corresponding values of $(M_G + A_G)_{lim}$ and $(G - K_S)$ using the extinction curve from Cardelli et al. (1989); O'Donnell (1994) with $R_V = 3.1$. If we assume that the PARSEC synthetic photometry is correct, and that the uncertainties on photometric measurements are small compared to other measured quantities involved in this process (for instance, astrometric parallax ϖ), a tolerance limit $(M_G + A_G)_{lim}$ is finally set for each star by interpolating the dashed line in Figure 9.2 (right panel) given the measured (G-K) of the star.

In addition to the above described selection, we apply a parallax cut at $\varpi < 2$ mas, in order to remove local structures. Furthermore, we apply an apparent magnitude cut, $G < 9$, according to TGAS completeness limit (Drimmel et al., in prep.), ending up with 3200 OB star candidates. We

[2]web inteface http://stev.oapd.inaf.it/cmd

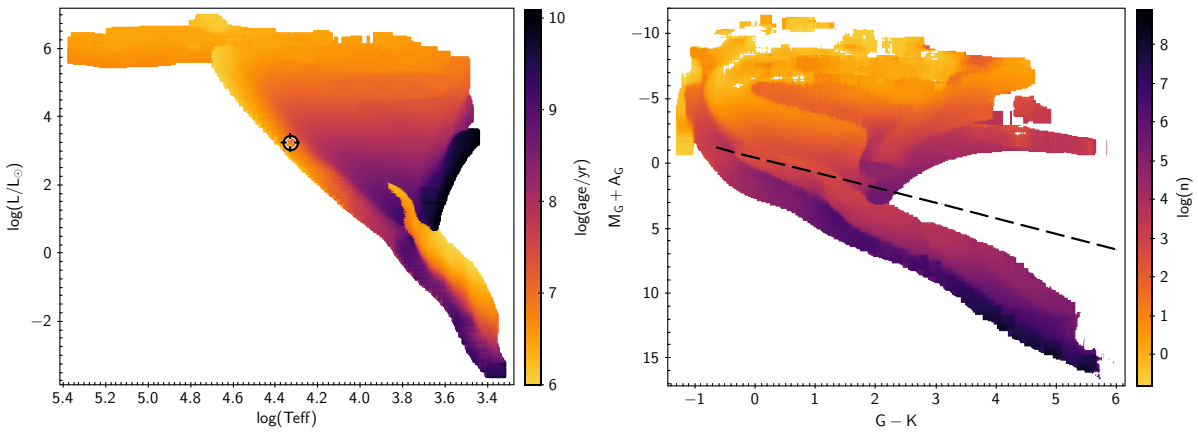

Figure 5.4: *Left plot:* The intrinsically faintest object that the procedure is aimed at selecting (black circle) compared to the Herzsprung-Russel diagram colored by stellar ages. *Right plot:* The variation of the tolerance limit in presence of extinction (dashed line) for Gaia and 2MASS photometric system, overplotted with the expected unreddened color-magnitude diagram (colored points). The colors are proportional to predicted number of stars n, obtained assuming a star formation rate constant with time, the canonical two-part power law IMF corrected for unresolved binaries (Kroupa, 2001, 2002), and solar constant metallicity. The details can be found in Section 6.1.2. These plots were made using the PARSEC Isochrones, version 1.2s (see text for references).

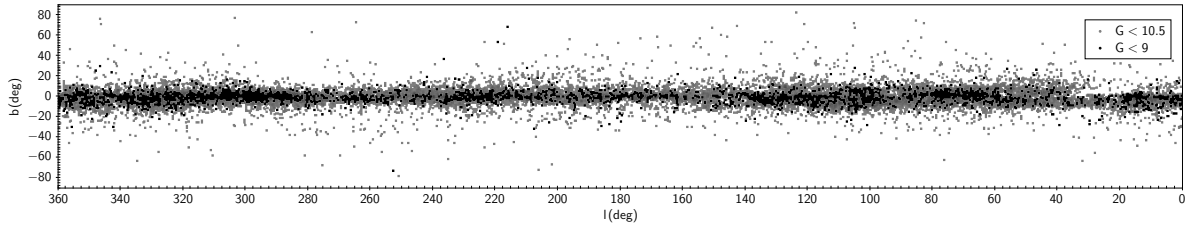

Figure 5.5: The selected OB star candidates on the sky, according to two different apparent magnitude cuts.

also consider a fainter sample with $G < 10.5$, containg 24 570 stars, taking account of the TGAS selection function according to Drimmel et al. (in prep.), as described in Section 6.3. Figure 5.5 shows the two samples distributed on the sky.

To test the content of our selected sample, we apply the selection procedure to the above mentioned T2STC, in which spectral types are provided. Assuming that the spectral classification provided by the T2STC is 100% correct, it turns out that the contamination from non-OB stars reaches approximately 33%, while the quantity of OB stars that we miss through the procedure amounts to 11%. If we apply a further cut at $\varpi < 1$ mas, the contamination decreases to 23% and the missed OB stars to 8%. By varying the adopted prior in Equation 9.1, i.e. choosing different values for h_z and L_R, we verified that the composition of the selected sample is not severely

sensitive to this choice. Most of the non-OB stars present in our sample are classified as upper main sequence A stars. Such stars, being young, still serve our purpose here, and we can in any case consider our selected stars as being a sample of young upper main sequence stars.

CHAPTER 6

THE MODEL

To explore the warp kinematic signal, we constructed a statistical tool, aimed at inferring the kinematic parameters of our model from the data. In the present Chapter, we describe in detail the tool, giving an overview of the adopted model of our Galaxy, as well as the adopted statistical approach. Considering previous results (see Chapter 4), we are motivated to relax the assumption made in Section 3.1 of a static warp; instead, we model the warp as a precessing feature. In Chapter 7, we will fit for the warp precession rate ω_p (Section 7.3.1) using the OB star candidates selected from the TGAS∩2MASS catalogue in Section 5.1. In order to infer the warp precession rate from our dataset, we need a model for the spatial distribution, color-magnitude diagram, extinction and kinematics of the OB stars in the Galaxy. We will collect all these elements into the symbol $\mathbf{\Theta}_{Gal}$ (which represents the model and its parameters), and describe each of them individually in Section 6.1. According to Bayes' theorem, we can calculate the probability of the model parameters $\mathbf{\Theta}_{Gal}$ given the data

$$p(\mathbf{\Theta}_{Gal}|\text{data}) = \frac{p(\text{data}|\mathbf{\Theta}_{Gal})\,p(\mathbf{\Theta}_{Gal})}{p(\text{data})} \quad , \tag{6.1}$$

where $p(\mathbf{\Theta}_{Gal}|\text{data})$ is the posterior, $p(\text{data}|\mathbf{\Theta}_{Gal})$ is the likelihood, $p(\mathbf{\Theta}_{Gal})$ is the prior and $p(\text{data})$ is the normalization constant. From the data, we use the astrometric measurement $\hat{\boldsymbol{\tau}} = (\hat{l}, \hat{b}, \hat{\varpi}, \hat{\mu_b})$[1] and the photometry $\hat{\mathbf{\Phi}} = (\hat{G}, \hat{J}, \hat{H}, \hat{Ks})$ from *Gaia* and 2MASS, with their respective covariance matrices $\mathbf{\Sigma}_{\hat{\boldsymbol{\tau}}}$ and $\mathbf{\Sigma}_{\hat{\mathbf{\Phi}}}$. Throughout this Chapter, the symbol $\hat{}$ characterizes the observed quantities, allowing us to distinguish them from the integration variables. The bold font is used

[1] We here consider only the Galactic latitude proper motion μ_b, given that the kinematic signature of the Galactic warp is expected to manifest itself in the component perpendicular to the Galactic plane, as discussed in the previous chapters.

for vectors and matrices. Equation 6.1 can be therefore rewritten as

$$p(\boldsymbol{\Theta}_{Gal}\,|\,\{\hat{\boldsymbol{\tau}},\hat{\boldsymbol{\Phi}},\boldsymbol{\Sigma}_{\hat{\boldsymbol{\tau}}},\boldsymbol{\Sigma}_{\hat{\boldsymbol{\Phi}}}\}_{data}) = \frac{p(\{\hat{\boldsymbol{\tau}},\hat{\boldsymbol{\Phi}}\}_{data}\,|\,\{\boldsymbol{\Sigma}_{\hat{\boldsymbol{\tau}}},\boldsymbol{\Sigma}_{\hat{\boldsymbol{\Phi}}}\}_{data},\boldsymbol{\Theta}_{Gal})\,p(\boldsymbol{\Theta}_{Gal})}{p(\{\hat{\boldsymbol{\tau}},\hat{\boldsymbol{\Phi}}\}_{data}\,|\,\{\boldsymbol{\Sigma}_{\hat{\boldsymbol{\tau}}},\boldsymbol{\Sigma}_{\hat{\boldsymbol{\Phi}}}\}_{data})} \quad . \tag{6.2}$$

While Equation 6.2 in general applies to the statistical inference of any parameter included in our Galactic model $\boldsymbol{\Theta}_{Gal}$, we here only consider the specific case of the fit for the warp precession rate ω_p (see Section 7.3.1), or for both ω_p and the solar motion in the vertical direction $V_{z,\odot}$ (see Section 7.3.2). To this end, the posterior probability distribution (as will be shown in Chapter 7) must be obtained by combining the elements at the right hand side of Equation 6.2, namely: the prior (that we decide to adopt as uniform, see the discussion in Section 7.3.1), the normalization constant (we here impose the normalization condition numerically) and the likelihood

$$p(\{\hat{\boldsymbol{\tau}},\hat{\boldsymbol{\Phi}}\}_{data}\,|\,\{\boldsymbol{\Sigma}_{\hat{\boldsymbol{\tau}}},\boldsymbol{\Sigma}_{\hat{\boldsymbol{\Phi}}}\}_{data},\boldsymbol{\Theta}_{Gal}) = \Pi_i^N\, p(\hat{\boldsymbol{\tau}}_i,\hat{\boldsymbol{\Phi}}_i\,|\,\boldsymbol{\Sigma}_{\hat{\boldsymbol{\tau}},\boldsymbol{i}},\boldsymbol{\Sigma}_{\hat{\boldsymbol{\Phi}},\boldsymbol{i}},\boldsymbol{\Theta}_{Gal}) \quad , \tag{6.3}$$

where the product is over the N stars present in the catalogue. For the i-th star of the catalogue, the likelihood can be written as

$$p(\hat{\boldsymbol{\tau}}_i,\hat{\boldsymbol{\Phi}}_i\,|\,\boldsymbol{\Sigma}_{\hat{\boldsymbol{\tau}},\boldsymbol{i}},\boldsymbol{\Sigma}_{\hat{\boldsymbol{\Phi}},\boldsymbol{i}},\boldsymbol{\Theta}_{Gal}) = \int S(\hat{\boldsymbol{\tau}}_i,\hat{\boldsymbol{\Phi}}_i)\,p(\hat{\boldsymbol{\tau}}_i,\hat{\boldsymbol{\Phi}}_i\,|\,\boldsymbol{\Sigma}_{\hat{\boldsymbol{\tau}},\boldsymbol{i}},\boldsymbol{\Sigma}_{\hat{\boldsymbol{\Phi}},\boldsymbol{i}},\boldsymbol{\tau},\boldsymbol{\Phi})\,p(\boldsymbol{\tau},\boldsymbol{\Phi}\,|\,\boldsymbol{\Theta}_{Gal})\,d\boldsymbol{\tau}\,d\boldsymbol{\Phi} \quad , \tag{6.4}$$

including the full model of the Galaxy $p(\boldsymbol{\tau},\boldsymbol{\Phi}\,|\,\boldsymbol{\Theta}_{Gal})$ (Section 6.1), the noise model $p(\hat{\boldsymbol{\tau}}_i,\hat{\boldsymbol{\Phi}}_i\,|\,\boldsymbol{\Sigma}_{\hat{\boldsymbol{\tau}},\boldsymbol{i}},\boldsymbol{\Sigma}_{\hat{\boldsymbol{\Phi}},\boldsymbol{i}},\boldsymbol{\tau},\boldsymbol{\Phi})$ (Section 6.2) and the selection function $S(\hat{\boldsymbol{\tau}},\hat{\boldsymbol{\Phi}})$ (Section 6.3). For the sake of simplicity, we will omit the i-th subscript from this point on.

6.1 The model of the Galaxy

The term $p(\boldsymbol{\tau},\boldsymbol{\Phi}\,|\,\boldsymbol{\Theta}_{Gal})$ in Equation 6.4 represents our *noise-free* model of the Galactic OB stellar population, and can be written as the combination of the modeled spatial distribution $\boldsymbol{\Theta}_{SP}$ (Section 6.1.1), the assumed color-magnitude diagram and extinction map $\boldsymbol{\Theta}_{CMD}$ (Section 6.1.2) and the kinematic model $\boldsymbol{\Theta}_{KIN}$ (Section 6.1.3):

$$p(\boldsymbol{\tau},\boldsymbol{\Phi}\,|\,\boldsymbol{\Theta}_{Gal}) = p(\mu_b\,|\,l,b,r,\boldsymbol{\Theta}_{KIN})\,p(\boldsymbol{\Phi}\,|\,l,b,r,\boldsymbol{\Theta}_{CMD})\,p(l,b,r\,|\,\boldsymbol{\Theta}_{SP}) \quad . \tag{6.5}$$

6.1.1 Spatial model

The probability $p(l,b,r\,|\,\boldsymbol{\Theta}_{SP})$ of finding a star at a given *true* position in the Galaxy (l,b,r) (with $r=\frac{1}{\varpi}$, being r and ϖ the *true* heliocentric distance and parallax of the star, respectively) is proportional to the density of stars predicted by our spatial model $\boldsymbol{\Theta}_{SP}$, which was already described in detail in Section 3.3 and 3.1, and that we briefly outline here for the sake of clarity. The collection of the spatial parameters can be found in Table 6.1, together with the adopted values and the corresponding references. For convenience, the equations of this Section are reported in Galactocentric cylindrical coordinates (R,ϕ,z).

Being traditionally considered the most relevant spiral tracers, we model the distribution of the OB stars in the Galactic plane as a superposition of four principle spiral arms, according to the map from Georgelin and Georgelin (1976); Taylor and Cordes (1993), though only the two nearby arms (i.e. the Perseus and Sagittarius-Carina arms) will be relevant here, due to the selection function (see Section 6.3). The pattern provided by the map coincides with the sites of maximum density parallel to the Galactic plane. We model the density to decrease across each arm with a gaussian profile, whose width increases linearly with Galactocentric radius. In addition to the four major spiral arms, we include a local arm, modeled as a logarithmic spiral segment located at

$$R_{Loc} = R_{Loc,0} \exp -(\tan p_{la} \phi) \quad , \tag{6.6}$$

p_{la} being the arm's pitch angle and $R_{Loc,0}$ the radius of the local arm at the Sun's position. Across the local arm, the density decreases as a gaussian with constant width w_{la}. Along the direction perpendicular to the Galactic plane, the density profile is exponential $\propto \exp(-|z|/h_z)$, with scale height h_z. Moreover, the stars belonging to the local arm are shifted vertically by an offset z_{Loc}. Finally, the Galactic disc is warped according to a time-dependent shift. Hence, the warp is not static (as opposed to Section 3.1), but we let it precess at a constant rate ω_p. The Galactic midplane is warped along the z-coordinate by

$$z_w(R,\phi,t) = h(R) \sin(\phi + \phi_w - \omega_p t) \quad , \tag{6.7}$$

where ϕ_w is the phase angle of the warp at $t = 0$ (i.e. today), ω_p is the precession rate (see below) and $h(R)$ is the height function

$$h(R) = h_0 (R - R_w)^{\alpha_w} \tag{6.8}$$

for $R > R_w$, where R_w is the radius at which the warp starts, α_w is the exponent determining the amplitude increase with radius, and h_0 is the amplitude normalization. According to this model, the warp of the Galactic disc is precessing in the direction of Galactic rotation for positive values of ω_p. As expected, this assumption has no impact on the assumed spatial warp (at the present time $t = 0$, Equation 6.7 coincides with the static warp of Equation 3.6 in Section 3.1), but only affects the kinematics (see Section 6.1.3).

6.1.2 Color-magnitude diagram

For a given position in the Galaxy (l,b,r), the probability $p(\mathbf{\Phi}\,|\,l,b,r,\mathbf{\Theta}_{CMD})$ of having a star with photometry $\mathbf{\Phi}$ is predicted by our model for the color-magnitude diagram $\mathbf{\Theta}_{CMD}$. The model $\mathbf{\Theta}_{CMD}$ is based on several elements, such as the Initial Mass Function (IMF), the Star Formation History (SFH), the adopted set of stellar isochrones and the extinction model, as described in

[2]The normalization is relative to the local arm, which has n_{LA}=1 by definition.

Table 6.1: Adopted spatial parameters.

Parameter	Adopted value	Source
Sun - Galactic center distance	$R_\odot = 8.2$ kpc	Bland-Hawthorn and Gerhard (2016)
Height of the Sun above $z = 0$	$z_\odot = 25$ pc	Bland-Hawthorn and Gerhard (2016)
Spiral arm pattern	map in (R, ϕ)	Georgelin and Georgelin (1976); Taylor and Cordes (1993); Bland-Hawthorn and Maloney (2002)
Increase of the arm width with R	$c_w = 0.06$	Drimmel and Spergel (2001)
Normalization of the Sag-Car arm[2]	n_{SC}=3.3	Poggio et al. (2017)
Normalization of the Perseus arm[2]	n_{Per}=0.27	Poggio et al. (2017)
Radius of the local arm at $\phi = 0$	$R_{Loc,0} = 8.3$ kpc	Poggio et al. (2017)
Local arm pitch angle	$p_{la} = 6.5°$	Poggio et al. (2017)
Local arm half-width	$w_{la} = 500$ pc	Poggio et al. (2017)
vertical offset of the local arm	$z_{Loc} = 25$ pc	Poggio et al. (2017)
Scale height of the OB stars	$h_z = 70$ pc	Poggio et al. (2017)
Warp starting radius (scaled to $R_\odot$)	$R_w = 6.27$ kpc	Yusifov (2004)
Exponent of the warp height function	$\alpha_w = 1.4$ kpc	Yusifov (2004)
Normalization of the warp height function	$h_0 = 0.037(\text{kpc}^{0.4})$ kpc	Yusifov (2004)
Warp phase angle	$\phi_w = -14.5^o$ kpc	Yusifov (2004)

the following. We here adopt the PARSEC isochrones (Bressan et al., 2012; Chen et al., 2014, 2015; Tang et al., 2014), assuming the canonical two-part power law IMF corrected for unresolved binaries (Kroupa, 2001, 2002), a SFH constant with time and solar constant metallicity. Hence, we calculate the predicted number of stars n with intrinsic color $(G-K)$ and magnitude M_G for $A_v = 0$, as shown by the right panel of Figure 9.2. Once properly normalized, the quantity n can be interpreted as the probability of having a star with intrinsic color $(G-K_S)$ and magnitude M_G when $A_v = 0$; we will refer to this as to our *intrinsic* model for the CMD. For any value of A_v, a similar CMD can be constructed using the tables provided by the PARSEC isochrones web interface[3], where the extinction curve from Cardelli et al. (1989); O'Donnell (1994) with $R_v = 3.1$ is applied to the photometric band of interest. Assuming that the intrinsic CMD is the same throughout the Galaxy (see Section 3.3 for a discussion on this assumption), the *observed* CMD is calculated as follows. We adopt the extinction map from Drimmel and Spergel (2001), which provides one value of A_v for every position (l,b,r). However, for a sample of stars in a given volume element, we expect to have an intrinsic dispersion in A_v. The intrinsic scatter is modeled as a lognormal distribution in A_v, having the median coincident with the value provided by the extinction map and standard deviation $\sigma_{A_v} = 0.2$ mag. For every position (l,b,r), we therefore have a collection of possible values of A_v. Hence, we associate to each position a list of observed CMDs. As mentioned before, the PARSEC isochrones allows us to construct the CMD with the extincted absolute magnitude in the G band $M_G + A_G$, once A_v is set. Then, we translate the y-axis of Figure 9.2 (right) according to the distance modulus equation $G = M_G + A_G - 5\log r + 5$, i.e. we substitute the extincted absolute magnitude $M_G + A_G$ with the apparent magnitude G. We finally marginalize over A_v, so that the uncertainty in the extinction map is incorporated in the final probability $p(G\,|\,l,b,r,\mathbf{\Theta}_{CMD})$. For the sake of simplicity, we have here only considered the probability of the star to have a given measured apparent magnitude G; the remaining magnitudes J, H, K from 2MASS are here only considered when incorporating the selection function into the observed CMD, by modelling the selection process of the OB candidates (see Section 5.1), as explained in Section 6.3.

6.1.3 Kinematics

The kinematic term $p(\mu_b\,|\,l,b,r,\mathbf{\Theta}_{KIN})$ includes the simple model described in Section 3.5, of which we now provide a brief overview, and for which the adopted parameters are listed in Table 6.2. The velocity dispersions are modeled to decrease exponentially with Galactocentric radius, and are normalized to the values of the solar neighborhood for the bluest stars. The model incorporates vertex deviation and a flat rotation curve. An additional systematic motion in the Galactic plane is added to the stars belonging to the local arm (see Section 3.5 for details). Finally, we add the systematic vertical signal induced by the warp, assumed to be precessing

[3] web interface http://stev.oapd.inaf.it/cmd

with constant rate ω_p, as anticipated in Section 6.1.1

$$\bar{V}_{z,prec}(R,\phi,t) = \left(\frac{\bar{V}_\phi}{R} - \omega_p\right) h(R)\cos(\phi + \phi_w + \omega_p\, t) \quad , \tag{6.9}$$

which is derived by applying the collisionless Boltzmann equation to the Galactic disc, warped according to Equations 6.7 and 6.8. If we consider the present time, i.e. $t = 0$, Equation 6.9 simply becomes

$$\bar{V}_{z,prec}(R,\phi) = \left(\frac{\bar{V}_\phi}{R} - \omega_p\right) h(R)\cos(\phi + \phi_w) \quad . \tag{6.10}$$

As expected, by setting ω_p = 0 km s^{-1} kpc, the warp model of Equation 6.10 coincides with the static warp of Equation 3.8 (presented in Poggio et al., 2017). In order to explore the warp kinematic nature, we will adopt the warp spatial parameters from the literature (reported in Table 6.1) and fit for the kinematic parameter ω_p (see Section 7.2). We will also discuss the variation of the results by adopting different sets of warp parameters (see Section 7.4).

6.2 The noise model

The term $p(\hat{\boldsymbol{\tau}}, \hat{\boldsymbol{\Phi}} \,|\, \Sigma_{\hat{\boldsymbol{\tau}}}, \Sigma_{\hat{\boldsymbol{\Phi}}}, \boldsymbol{\tau}, \Phi)$ models the noise of the measurement process for both the astrometry $\hat{\boldsymbol{\tau}} = (\hat{l}, \hat{b}, \hat{\varpi}, \hat{\mu_b})$ and photometry $\hat{\boldsymbol{\Phi}} = (\hat{G}, \hat{J}, \hat{H}, \hat{Ks})$. With regards to the astrometric measurements, we here assume, to a first approximation, that the uncertainties on the position (l, b) are insignificant compared to the ones on the other two astrometric quantities ϖ and μ_b, so that the non-trivial elements of the astrometric covariance matrix $\Sigma_{\hat{\boldsymbol{\tau}}}$ are

$$\Sigma_{\hat{\boldsymbol{\varpi}},\hat{\boldsymbol{\mu}}_{\boldsymbol{b}}} = \begin{pmatrix} \sigma^2_\varpi & \rho_{\varpi\mu_b}\sigma_\varpi\sigma_{\mu_b} \\ \rho_{\varpi\mu_b}\sigma_\varpi\sigma_{\mu_b} & \sigma^2_{\mu_b} \end{pmatrix} \quad , \tag{6.11}$$

which uniquely defines the bivariate gaussian

$$p(\hat{\varpi}, \hat{\mu}_b \,|\, \sigma_\varpi, \sigma_{\mu_b}, \rho_{\mu_b,\varpi}, 1/r, \mu_b) = \frac{1}{2\pi\sigma_\varpi\sigma_{\mu_b}\sqrt{1-\rho^2_{\mu_b,\varpi}}} e^{-\frac{1}{2}\left[\frac{(\mu_b-\hat{\mu}_b)^2}{(1-\rho^2_{\mu_b,\varpi})\sigma^2_{\mu_b}} - \frac{2\rho_{\mu_b,\varpi}(\mu_b-\hat{\mu}_b)(1/r-\hat{\varpi})}{(1-\rho^2_{\mu_b,\varpi})\sigma_{\mu_b}\sigma_\varpi} + \frac{(1/r-\hat{\varpi})^2}{(1-\rho^2_{\mu_b,\varpi})\sigma^2_\varpi}\right]} \quad , \tag{6.12}$$

which models the noise on $\varpi = 1/r$ and μ_b. We remind the reader that the symbol $\hat{}$ defines the measured quantities, as opposed to the *true* quantities. The elements of the covariance matrix $\sigma_{\mu_b}, \rho_{\mu_b,\varpi}$ are obtained by converting in Galactic coordinates the ones provided by the *Gaia* catalogue for the proper motions in equatorial coordinates. Similarly to the astrometric component, approximations are made also for the measured photometry $\hat{\boldsymbol{\Phi}} = (\hat{G}, \hat{J}, \hat{H}, \hat{Ks})$. We assume that the uncertainty associated with the extinction map (modeled in Section 6.1.2) has much more impact on our assumed CMD than the uncertainties on measured magnitudes, so that we can write - to a first approximation- $\hat{G} \simeq G, \hat{J} \simeq J, \hat{H} \simeq H, \hat{Ks} \simeq Ks$. As mentioned before,

Table 6.2: Adopted kinematic parameters. Some parameters are taken from the literature, others are taken from Paper I.

Parameter	Adopted value	Source
velocity dispersions in the solar neighborhood	$\sigma_{(1,2,3)} = (14.35, 9.33, 5.45)$km s^{-1}	Dehnen and Binney (1998)
Radial scale length	h_R=2.3 kpc	Drimmel and Spergel (2001)
vertex deviation	$l_v = 30°$	Dehnen and Binney (1998)
Circular rotation velocity at the Solar radius	$\Theta = 238$ km s^{-1}	Bland-Hawthorn and Gerhard (2016)
Rotation curve	Flat	Reid et al. (2014)
Solar motion	$(U_\odot, V_\odot, W_\odot) = (11.1, 12.24, 7.25)$km s^{-1}	Schönrich et al. (2010)
Systematic velocity of the Local Arm	$(\Delta V_C, \Delta V_R) = (6, 1)$km s^{-1}	Poggio et al. (2017)

a similar approximation was for the measured positions, so that we can write $\hat{l} \simeq l, \hat{b} \simeq b$. Hence, our noise model simply reduces to

$$p(\hat{\boldsymbol{\tau}}, \hat{\boldsymbol{\Phi}} \,|\, \boldsymbol{\Sigma}_{\hat{\boldsymbol{\tau}}}, \boldsymbol{\Sigma}_{\hat{\boldsymbol{\Phi}}}, \boldsymbol{\tau}, \boldsymbol{\Phi}) = p(\hat{\boldsymbol{\tau}} \,|\, \Sigma_{\hat{\boldsymbol{\tau}}}, \boldsymbol{\tau}) = p(\hat{\varpi}, \hat{\mu}_b \,|\, \sigma_\varpi, \sigma_{\mu_b}, \rho_{\mu_b,\varpi}, 1/r, \mu_b) \quad , \tag{6.13}$$

which is the bivariate gaussian in Equation 6.12.

6.3 The selection function

Equation 6.4 contains the selection function $S(\hat{\boldsymbol{\tau}}, \hat{\boldsymbol{\Phi}})$, which includes both the intrinsic selection function of the TGAS∩2MASS catalogue and the selection criteria used in Section 5.1. We first describe the selection function, as modeled by Drimmel et al. (in prep.). The selection function of TGAS∩2MASS can be written as $S((J-K_s), G, \vec{r})$, which is function of observed color $J-K_S$, apparent magnitude G and direction vector $\vec{r} = (l, b)$. For $G \leq 9$, the TGAS selection function has very little spatial dependence, so that we can approximately ignore the scanning law of the Gaia satellite, assuming that the selection is dependent on photometry only $S((J-K_s), G)$. For the sample with $G < 10.5$, we adopted a more sophisticated approach, using the completeness map shown in Figure 6.2. Due to the limited number of bright stars, it is not possible to accurately measure the completeness as a function of magnitude for specific directions. A practical way forward is to use the map of the completeness between magnitudes $9 < G < 10$ is the follwing:

$$S((J-K_s), G, \vec{r}) = S(J-K_s) S(G) \left(\frac{C_{map}(\vec{r})}{C_{all-sky}(G=10)} \right), \tag{6.14}$$

where $C_{map}(\vec{r})$ is the map in Figure 6.2 and $C_{all-sky}(G=10)$ is the value of the all-sky completeness at G=10, while $S(J-K_S)$ and $S(G)$ are, respectively, the selection function of TGAS∩2MASS in function of the observed color $J-K_s$ (Table 6.4) and apparent magnitude G (Table 6.3). In Equation 6.14, the dependency of the selection function from magnitude and color has been separated, as the magnitudedependence of the selection function in *Gaia* is a consequence of the astrometric processing, while the color dependence is a consequence of the photometric processing, and these two data processing pipelines were independent of one another.

In addition to the TGAS∩2MASS catalogue selection function, we also model the selection process performed in Section 5.1. The color-color selection is modeled by setting to 0 the probability $p(G \,|\, l, b, \varpi, \boldsymbol{\Theta}_{CMD})$ of the regions of the CMD (see Section 6.1.2) excluded by the color-color cuts applied in Section 6.1.2, as well as those that have $G > 9$ (or $G > 10.5$, depending on the adopted sample).

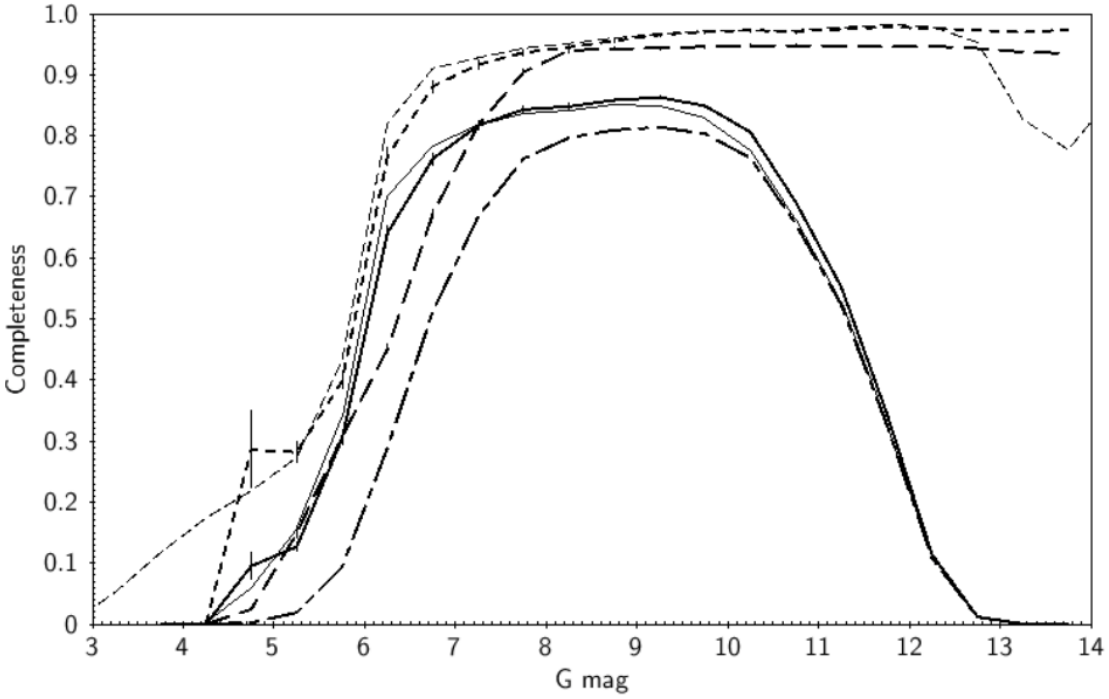

Figure 6.1: From Drimmel et al. (in prep): Completeness of TGAS (solid line), Gaia DR1 (short-dashed line), 2MASS (long-dashed line) and of a TGAS∩2MASS catalogue (dash-dot line) with respect to G magnitude for $(J-K_s) < 1.2$. Thin solid and dashed lines show the TGAS and DR1 completeness derived from Tycho2.

Table 6.3: Selection function of TGAS∩2MASS in function of the G magnitude according to Drimmel et al. (in prep).

G	Selection function
4.25	0.0
4.75	0.003681762
5.25	0.020732425
5.75	0.102041525
6.25	0.301079902
6.75	0.528321792
7.25	0.680886988
7.75	0.776955671
8.25	0.813259288
8.75	0.822268507
9.25	0.82146163
9.75	0.799458104

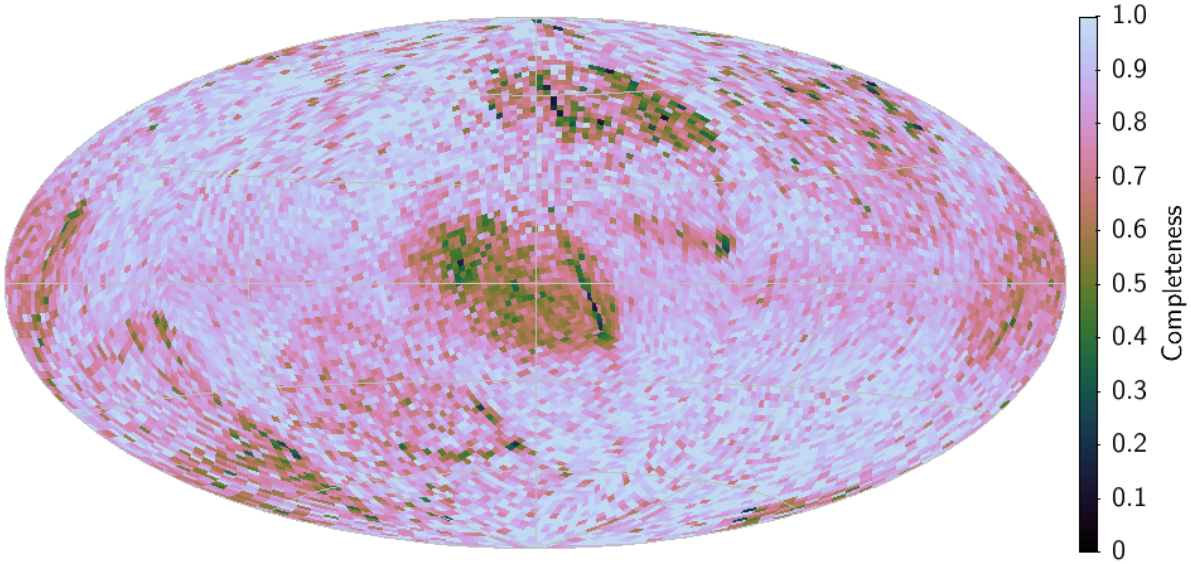

Figure 6.2: From Drimmel et al. (in prep): Sky maps (Aitoff projection, galactic coordinates, HEALPix level 5) of the completeness of TGAS between the 9^{th} and 10^{th} G magnitude using the crossmatch between *Gaia* DR1 and 2MASS.

Table 6.4: Selection function of TGAS∩2MASS in function of observed color $J-K_S$ according to Drimmel et al. (in prep).

$J-K_S$	Selection function
-0.45	0.0
-0.35	0.0
-0.25	0.176276557
-0.15	0.460232842
-0.05	0.870011372
0.05	0.990030004
0.15	1.0
0.25	1.0
0.35	1.0
0.45	1.0
0.55	1.0
0.65	1.0
0.75	1.0
0.85	1.0
0.95	1.0
1.05	1.0
1.15	1.0
1.25	0.957177528
1.35	0.727530759
1.45	0.454644225
1.55	0.238788132
1.65	0.085374086
1.75	0.044678708
1.85	0.051414923
1.95	0.06608412
2.05	0.067233301
2.15	0.076284971
2.25	0.090516919
2.35	0.11733663
2.45	0.211236554
2.55	0.374045657
2.65	0.670064585
2.75	0.963450934
2.85	1.025609059
2.95	1.025609059
3.05	1.025609059

CHAPTER 7

RESULTS

As previously outlined, the intent of Part III of this Thesis is to investigate the kinematic signature of the warp with a subset of OB stars candidates from the TGAS∩2MASS catalogue, selected in Chapter 5. In the present Chapter, we describe the practical implementation of the statistical approach described in Chapter 6, providing details on how the inference is performed (Section 7.1). A routine validation test is presented in Section 7.2, followed by the results obtained with the data (Section 7.3) by fitting for the warp precession rate ω_p (Section 7.3.1) and studying its degeneracy with the solar motion in the vertical direction (Section 7.3.2). Finally, we comment and discuss our results in Section 7.4.

7.1 Inferring the warp precession from the data

We here describe the details on how the statistical inference from Chapter 6 is performed. Let's now consider the case of Section 7.3.1, where, as already anticipated, we fit for the warp precession rate ω_p (a similar procedure will be applied in Section 7.3.2, where we will fit for both ω_p and the vertical component of the solar motion $V_{z,\odot}$). Bayes' theorem (Equation 6.2) allows us to determine how likely is a value of ω_p given the data. Hence, we consider a list of possible values of ω_p, and determine how likely they are, according to the dataset. For a fixed value of $\omega_{p,0}$, Equation 6.10 predicts the mean vertical velocity $\bar{V}_{z,prec,0}$ in a given position of the Galaxy (l, b, r). For every star, we calculate the likelihood of Equation 6.4 - i.e. the probability of measuring

$\hat{l},\hat{b},\hat{\omega},\hat{\mu_b},\hat{G},\hat{J},\hat{H},\hat{Ks}$ given the set of model parameters -

$$p(\hat{l},\hat{b},\hat{\omega},\hat{\mu_b},\hat{G},\hat{J},\hat{H},\hat{Ks}|\sigma_{\mu_b},\sigma_{\omega},\rho_{\mu_b,\omega},\mathbf{\Theta}_{Gal,0}) = \int S(\hat{l},\hat{b},\hat{G},\hat{J},\hat{H},\hat{Ks})\cdot p(\hat{\omega},\hat{\mu_b}|\sigma_{\omega},\sigma_{\mu_b},\rho_{\mu_b,\omega},1/r,\mu_b)\cdot \cdot p(\mu_b|l,b,r,\mathbf{\Theta}_{KIN,0})\cdot p(G,J,H,Ks|l,b,r,\mathbf{\Theta}_{CMD})\cdot p(l,b,r|\mathbf{\Theta}_{SP})drd\mu_b \quad , \tag{7.1}$$

where the Galactic model term $\mathbf{\Theta}_{Gal,0}$ includes $\omega_{p,0}$, and collects the spatial and CMD model $\mathbf{\Theta}_{SP},\mathbf{\Theta}_{CMD}$ (for which the parameter ω_p is irrelevant) and the kinematic term $\mathbf{\Theta}_{KIN,0}$ (which includes the mean vertical velocity $\bar{V}_{z,prec,0}$, see above). Once the likelihood is calculated for each star, and therefore the integral of Equation 7.1 is solved (as explained in the following), we calculate the product of the likelihoods (see Equation 6.3). By assuming a broad uniform prior (see the discussion in Section 7.3.1), the obtained value is proportional to the posterior probability $p(\mathbf{\Theta}_{Gal}|\{\hat{\boldsymbol{\tau}},\hat{\mathbf{\Phi}},\mathbf{\Sigma}_{\hat{\boldsymbol{\tau}}},\mathbf{\Sigma}_{\hat{\mathbf{\Phi}}}\}_{data})$, that we here, for simplicity, rewrite as $p(\omega_{p,0}|\text{data})$. We repeat a similar process for the values $\omega_{p,1},...,\omega_{p,n}$, calculating $p(\omega_{p,1}|\text{data}),...,p(\omega_{p,n}|\text{data})$, so that we construct a pdf for the parameter ω_p. When adjusting more than two parameters (which is not our case), the parameter space would be more efficiently explored by an MCMC algorithm rather than simple tabulated values.

We now describe the calculation of the integral in Equation 7.1. As a consequence of the assumptions made in Section 6.2, Equation 6.4 simply reduces to the double integral in Equation 7.1, that we want to solve for each star. We calculate numerically the integral on r via Monte Carlo integration. For each resample on r, we calculate analytically the term relative to μ_b, which is

$$I_{\mu_b}(r) = \int_{-\infty}^{\infty} p(\hat{\omega},\hat{\mu_b}|\sigma_{\omega},\sigma_{\mu_b},\rho_{\mu_b,\omega},1/r,\mu_b)\,p(\mu_b|l,b,r,\mathbf{\Theta}_{KIN})d\mu_b \quad , \tag{7.2}$$

which includes both the kinematic model and the noise model for the measured $\hat{\mu_b}$ and $\hat{\omega}$, i.e. the bivariate gaussian of Equation 6.12. Hence, the final integral to solve is

$$I_r = \int_0^{\infty} S(\hat{l},\hat{b},\hat{G},\hat{J},\hat{H},\hat{Ks})\cdot p(G,J,H,Ks|l,b,r,\mathbf{\Theta}_{CMD})\cdot p(l,b,r|\mathbf{\Theta}_{SP})\cdot I_{\mu_b}(r)dr \quad , \tag{7.3}$$

The details on the analytic integration of the integral $I_{\mu_b}(r)$ are given in Section 7.1.1, while the Monte Carlo integration of I_r is described in Section 7.1.2. The reader not interested in such details should move directly to Section 7.2.

7.1.1 Analytic integration of the kinematic term

For a given position (l,b,r), our kinematic model predicts gaussian distribution of the velocities V_x,V_y and V_z around the mean values $\bar{V}_{x,th},\bar{V}_{y,th}$ and $\bar{V}_{z,th}$. Our predicted $\bar{V}_{z,th}$ is given by Equation 6.10, while $\bar{V}_{x,th},\bar{V}_{y,th}$ are calculated based on the rotation curve of the Galaxy and the systematic velocity associated to the local arm (see Table 6.2, Sections 3.5 and 6.1.3). The

amplitude of the gaussian is calculated as follows. We start from the velocity dispersions in the three components $\epsilon_{0,vx}, \epsilon_{0,vy}, \epsilon_{0,vz}$, with

$$\epsilon_{0,vx} = \sigma_{\odot,x} \exp(R_\odot - R)/(2\,h_R) \quad ,$$

where $\sigma_{\odot,x}$ is the velocity dispersion near the Sun for the OB stars (see Section 3.5 and Table 6.2) along the x-axis, pointing toward the Galactic Center, and the radial factor models the variation of the velocity dispersions in function of the Galactic radius R (the parameters $R_\odot$ and h_R are taken from Table 6.1 and 6.2, respectively). In a similar way, we construct the other two components $\epsilon_{0,vy}$ (toward Galactic rotation) and $\epsilon_{0,vz}$ (perpendicular to the Galactic plane). Finally, we apply the vertex deviation, which consists in a clockwise rotation of $\theta = 30^o$ (see Table 6.2) of the velocity ellipsoid in the xy plane; the rotation has no impact on the mean values $\bar{V}_{x,th}, \bar{V}_{y,th}$, but only affects the intrinsic dispersions calculated sofar. Hence, from the initial $\epsilon_{0,vx}, \epsilon_{0,vy}$, we obtained the the new dispersions ϵ_{vx}^{new} and ϵ_{vy}^{new} with correlation coefficient ρ_{vxvy}^{new}. The new bi-dimensional gaussian in the xy plane can be written as

$$f(V_x, V_y) = A_{norm}\, e^{-\left(a_{rot}(V_x-\bar{V}_{x,th})^2 + 2b_{rot}(V_x-\bar{V}_{x,th})(V_y-\bar{V}_{y,th}) + c_{rot}(V_y-\bar{V}_{y,th})^2\right)} \tag{7.4}$$

with:

$$a_{rot} = \frac{\cos^2(\theta)}{2\epsilon_{0,vx}^2} + \frac{\sin^2(\theta)}{2\epsilon_{0,vy}^2} \tag{7.5}$$

$$b_{rot} = -\frac{\sin(2\theta)}{4\epsilon_{0,vx}^2} + \frac{\sin(2\theta)}{4\epsilon_{0,vy}^2} \tag{7.6}$$

$$c_{rot} = \frac{\sin^2(\theta)}{2\epsilon_{0,vx}^2} + \frac{\cos^2(\theta)}{2\epsilon_{0,vy}^2} \tag{7.7}$$

The new intrinsic dispersions and their correlation are:

$$\epsilon_{vx}^{new} = \frac{1}{\sqrt{2(1-\rho_{vxvy}^{new,2})a_{rot}}} \tag{7.8}$$

$$\epsilon_{vy}^{new} = \frac{1}{\sqrt{2(1-\rho_{vxvy}^{new,2})c_{rot}}} \tag{7.9}$$

$$\rho_{vxvy}^{new} = -\frac{b_{rot}}{\sqrt{a_{rot}c_{rot}}} \tag{7.10}$$

Hence, for a given position (l, b, r), we are able to predict the velocity distribution, which is a three-dimensional gaussian, centered on $\bar{V}_{x,th}, \bar{V}_{y,th}, \bar{V}_{z,th}$, whose covariance matrix includes the

dispersions (ϵ_{vx}^{new} etc.) and correlations (ρ_{vxvy}^{new} is the only non-zero correlation) as calculated above. From the intrinsic velocity distribution, we calculate the predicted distribution in proper motions (that will be included in Equation 7.2), which is still a gaussian

$$p(\mu_b \,|\, l, b, r, \mathbf{\Theta}_{KIN}) = \frac{1}{\sqrt{2\pi}\,\epsilon_{\mu_b}} e^{-\frac{1}{2}\left(\frac{\mu_b - \bar{\mu}_{b,th}}{\epsilon_{\mu_b}}\right)^2} \quad , \tag{7.11}$$

centered on

$$\bar{\mu}_{b,th} = 0.2104\left(-(\bar{V}_{x,th} - V_{x,\odot})\sin b\cos l - (\bar{V}_{y,th} - V_{y,\odot})\sin b\sin l + (\bar{V}_{z,th} - V_{z,\odot})\cos b\right)/r \tag{7.12}$$

and having intrinsic dispersion

$$\epsilon_{\mu_b} = 0.2104\left(\sqrt{\epsilon_{vx}^{new,2}\sin^2 b\cos^2 l + \epsilon_{vy}^{new,2}\sin^2 b\sin^2 l + 2\sin^2 b\sin l\cos l\,\rho_{vxvy}^{new}\epsilon_{vx}^{new}\epsilon_{vy}^{new} + \epsilon_{0,vz}^2\cos^2 b}\right)/r \quad . \tag{7.13}$$

We have now obtained the intrinsic distribution in μ_b predicted by our model; to solve the integral of Equation 7.2, we have to combine it with the noise model

$$p(\hat{\omega}, \hat{\mu}_b \,|\, \sigma_\omega, \sigma_{\mu_b}, \rho_{\mu_b,\omega}, 1/r, \mu_b) = \frac{1}{2\pi\sigma_{\hat{\omega}}\sigma_{\mu_b}\sqrt{1-\rho_{\mu_b,\omega}^2}} e^{-\frac{1}{2}\left[\frac{(\mu_b-\hat{\mu}_b)^2}{(1-\rho_{\mu_b,\omega}^2)\sigma_{\mu_b}^2} - \frac{2\rho_{\mu_b,\omega}(\mu_b-\hat{\mu}_b)(1/r-\hat{\omega})}{(1-\rho_{\mu_b,\omega}^2)\sigma_{\mu_b}\sigma_\omega} + \frac{(1/r-\hat{\omega})^2}{(1-\rho_{\mu_b,\omega}^2)\sigma_{\hat{\omega}}^2}\right]} \quad . \tag{7.14}$$

Hence, Equation 7.2 becomes

$$I_{\mu_b} = \int_{-\infty}^{\infty} \frac{1}{2\pi\sigma_{\hat{\omega}}\sigma_{\mu_b}\sqrt{1-\rho_{\mu_b,\omega}^2}} e^{-\frac{1}{2}\left[\frac{(\mu_b-\hat{\mu}_b)^2}{(1-\rho_{\mu_b,\omega}^2)\sigma_{\mu_b}^2} - \frac{2\rho_{\mu_b,\omega}(\mu_b-\hat{\mu}_b)(1/r-\hat{\omega})}{(1-\rho_{\mu_b,\omega}^2)\sigma_{\mu_b}\sigma_\omega} + \frac{(1/r-\hat{\omega})^2}{(1-\rho_{\mu_b,\omega}^2)\sigma_{\hat{\omega}}^2}\right]} \frac{1}{\sqrt{2\pi}\,\epsilon_{\mu_b}} e^{-\frac{1}{2}\left(\frac{\mu_b-\bar{\mu}_{b,th}}{\epsilon_{\mu_b}}\right)^2} d\mu_b \quad , \tag{7.15}$$

which is a 1-dimensional gaussian integral for a given value of r. It has been demonstrated that a gaussian integral of the form

$$I = \int_{-\infty}^{\infty} K e^{-ax^2+bx+c}\, dx \tag{7.16}$$

has the following solution:

$$I = K\sqrt{(\pi/a)}\, e^{(b^2/(4a)+c)} \quad . \tag{7.17}$$

If we define the following constants

$$A \equiv \frac{1}{(1-\rho_{\mu_b,\omega}^2)\sigma_{\hat{\omega}}^2} \quad , \tag{7.18}$$

$$B \equiv \frac{1}{(1-\rho_{\mu_b,\omega}^2)\sigma_{\mu_b}^2} \quad , \tag{7.19}$$

and

$$C \equiv \frac{1}{\epsilon_{\mu_b}^2} \quad , \tag{7.20}$$

Equation 7.15 can be written in the form of Equation 7.16

$$a = \frac{B+C}{2} \quad , \tag{7.21}$$

$$b = B\hat{\mu}_b + C\bar{\mu}_{b,th} + \sqrt{AB}\,\rho_{\mu_b,\varpi}(1/r - \hat{\varpi}) \quad , \tag{7.22}$$

$$c = -\frac{B\hat{\mu}_b^2 + C\bar{\mu}_{b,th}^2 + A(1/r-\hat{\varpi})^2}{2} - \sqrt{AB}\,\rho_{\mu_b,\varpi}(1/r-\hat{\varpi})\hat{\mu}_b \quad , \tag{7.23}$$

$$K = \frac{\sqrt{ABC}}{(2\pi)^{3/2}\sqrt{1-\rho_{\mu_b,\varpi}^2}} \quad . \tag{7.24}$$

Therefore, we can write the solution of the integral for each star $I_{\mu_b} = K\sqrt{(\pi/a)}e^{(b^2/(4a)+c)}$ according to Equation 7.17, where a, b, c and K are given in Equations 7.21, 7.22, 7.23 and 7.24, respectively.

7.1.2 Monte Carlo integration over heliocentric distance

Monte Carlo integration is a technique for numerical integration, which allows us to evaluate integrals when analytic integration is not possible or extremely difficult. A definite integral

$$I = \int_{x_0}^{x_1} f(x)\,dx \tag{7.25}$$

over the volume

$$V = \int_{x_0}^{x_1} dx \tag{7.26}$$

can be evaluated via Monte Carlo integration by generating n resamples $\{x_n\}$ over the volume V, and calculating

$$I \simeq \frac{V}{n}\sum_i^n f(x_n) \quad , \tag{7.27}$$

which is a good approximation of the integral I for sufficiently large numbers of n. Similarly, we solve the integral in Equation 7.3

$$I_r = \int_0^{r_{max}} S(\hat{l},\hat{b},\hat{G},\hat{J},\hat{H},\hat{Ks})\cdot p(G,J,H,Ks\,|\,l,b,r,\mathbf{\Theta}_{CMD})\cdot p(l,b,r\,|\,\mathbf{\Theta}_{SP})\cdot I_{\mu_b}(r)\,dr = \int_0^{r_{max}} f(r)\,dr \tag{7.28}$$

by generating uniform resamples $\{r_n\}$ between 0 and r_{max}, and evaluating the integrand at $f(r_n)$. The choice of r_{max} is arbitrary, and must include all the regions of interest for the integrand - but also avoid (for computational reasons) oversampling in regions where the integrand is nearly 0. We adopted $r_{max} = 20$ kpc, and verified that, in any case, a slight variation of the adopted value has no impact on our results. To calculate the integral in Equation 7.28 according to Equation 7.27,

we evaluate the various terms of the integrand at the positions $f(r_n)$, namely: the kinematic term $I_{\mu_b}(\{r_n\})$ (as explained in Section 7.1.1), the spatial term $p(l,b,\{r_n\}|\mathbf{\Theta}_{SP}) \propto \rho(l,b,\{r_n^2\})\{r_n^2\}$, where $\rho(l,b,\{r_n\})$ is the spatial density (Section 6.1.1) and $\{r_n^2\}$ is a geometric factor, the color-magnitude diagram $p(G|l,b,\{r_n\},\mathbf{\Theta}_{CMD})$ (Section 6.1.2) and, finally, the selection function $S(\hat{l},\hat{b},\hat{G},\hat{J},\hat{H},\hat{Ks}$ (Section 6.3), which is only function of observed quantities and, during the integration process, can be treated as a constant.

7.2 Routine validation

In order to validate the fitting routine, we generate a mock catalogue with known precession rate $\omega_{p,true}$ and test whether it can be successfully recovered. The synthetic catalogue is generated in a Monte-Carlo fashion in accordance with the model presented in Chapter 6. The mock stars are given a random three dimensional position according to the spiral arm pattern and the vertical profile described in Sections 6.1.1 and 3.3. We assign the mock absolute magnitudes G proportionally to the prediction from the adopted unreddened CMD (Section 6.1.2). Each star is also associated to a value of extinction A_V, randomly extracted from the lognormal intrinsic dispersion around the value predicted by the extinction map (Section 6.1.2). Moreover, stars are assigned random velocities according to the kinematic model presented in Section 6.1.3, including the systematic signal induced by a warp precessing with fixed rate $\omega_{p,true}$, as predicted by Equation 6.10. Simulated uncertainties and correlations on the astrometric parameters ϖ and μ_b are generated as follows. For the TGAS sources, *Gaia* DR1 provides astrometric uncertainties and correlations in equatorial coordinates; we convert them in galactic coordinates source by source, and construct projection maps with the medians of σ_{μ_b} and $\rho_{\mu_b,\varpi}$, as shown in Figure 7.1. For a mock star with a given position on the sky, the covariance matrix is constructed from the maps in Figure 7.1, and multivariate random noise is added to the true mock quantities. We point out that the maps are only used for the construction of the mock catalogue; for real data, the covariance matrix is given for each single star of the catalogue. Finally, stars are retained or discarded according to the selection function (see Section 6.3), which includes both the TGAS selection function and the OB selection process described in Section 5.1. Moreover, the apparent magnitude cut $G < 9$ and the parallax cut $\varpi < 2$ mas are applied, for consistency with the real data selection. Once the mock catalogue is ready, the fitting procedure is applied to it. We construct several mock catalogues (containing 3200 mock stars, to simulate the real dataset) and study whether the recovered values are consistent with the input parameter $\omega_{p,true} = 0$ km s^{-1} kpc^{-1}. We find that the estimated value is always consistent with true input parameter $\omega_{p,true}$, which systematically lies within 3σ from the median/mode/mean of the obtained distribution (where σ is the standard deviation of the distribution). Although this result is encouraging, a note of caution is necessary: the mock catalogue was specifically constructed with the purpose of being perfectly consistent with the model adopted by the fitting routine. However, any application to

the real data should be carefully investigated, since reality might be more complex than our simple model.

7.3 Results

7.3.1 Estimating the warp precession rate

We here present the results obtained with the sample of 3200 stars with $G < 9$ selected in Section 5.1. As described in Section 7.1, the fitting procedure requires the construction of the posterior probability distribution for the warp precession rate ω_p, that we want to infer from the data. As anticipated in Chapter 6, we decided to adopt a broad uniform prior on ω_p, which reflects our lack of previous knowledge of the warp precession rate of our Galaxy. Indeed, no previous estimates are available in the literature, due to the insufficient precision of the pre-*Gaia* astrometry. With the advent of the first *Gaia* data release, such a measure has been made possible for the first time; this is confirmed by the results obtained in Section 7.2 with simulated catalogues, which present typical TGAS astrometric uncertainties. The posterior distribution for the parameter ω_p, therefore, coincides with the likelihood probability distribution of Equation 6.3, which is calculated as a product over the 3200 stars of the catalogue. Figure 7.2 shows the obtained posterior probability distribution. A similar distribution (here not shown) has been obtained also for the catalogue with G<10.5, containig 24 570 stars (see Section 5.1). The most probable value of ω_p given the data (i.e. the mode of the distribution) occurs at 40.7 km s^{-1} kpc^{-1}. The distribution appears to be symmetric, and its mean, median and mode coincide. Hence, the inferred value for the warp precession rate is $\tilde{\omega}_p = 40.7 \pm 1.3$ km s^{-1} kpc^{-1}, where the confidence interval is given by the 10^{th} and the 90^{th} percentiles of the distribution.

7.3.2 Estimating the warp precession rate and the solar vertical velocity

As reported in Chapter 6, the inference of the parameter ω_p (Section 7.3.1) was performed maintaining fixed the other parameters of the Galactic model, i.e. the ones constituting the spatial, CMD and kinematic model. By performing numerous tests, we verified that a variation of the adopted values has no impact on the estimated ω_p for many parameters. We here present an interesting case, where we adjust simultaneously ω_p and the vertical component of the Solar motion $V_{z,\odot}$[1]. The result of the fit is shown in Figure 7.3. The degeneracy of the two parameters is apparent in the bottom left panel of Figure 7.3; as we can see, a variation of only 1 km s^{-1} in $V_{z,\odot}$ (for instance, from $V_{z,\odot} = 12$ to $V_{z,\odot} = 13$ km s^{-1}) results in a difference of approximately 10 km s^{-1} kpc^{-1} for the warp precession rate ω_p. From the two marginalized posterior distributions for ω_p (top left plot) and $V_{z,\odot}$ (bottom right plot) in Figure 7.3 we obtain the following estimated values: $\tilde{\omega}_p = 4.65^{+3.04}_{-3.05}$ km s^{-1} kpc^{-1} and $\tilde{V}_{z,\odot} = 12.64^{+0.40}_{-0.39}$ km s^{-1} (median, 10^{th} and 90^{th} percentiles of

[1] In the previous Chapters, the vertical component of the Solar motion was written as $W_\odot$

the distribution). These results, as well as those presented in Section 7.3.1, will be interpreted and discussed in the following Section.

7.4 Discussion

The statistical tool presented in Chapter 6 has been specifically developed with the purpose of inferring Galactic parameters from the data, based on an assumed model of the Galaxy, of the errors introduced by the measurement process and the selection function of the catalogue. We presented here a practical application to a subset of OB star candidates in the TGAS catalogue, selected in Chapter 5. By fitting for the warp precession rate, we obtain a value of ≈ 40 km s^{-1} kpc^{-1}, which implies a warp precessing at ≈ 320 km s^{-1} at the Solar circle (i.e. faster than the assumed rotation velocity at the Sun). A precession of this magnitude could be only associated with an highly unstable warp. However, further investigation leads to an interesting alternative scenario. We find a crucial connection between the estimated warp precession and the vertical component of the solar motion. By fitting simultaneously for those two parameters, we obtain a much lower precession rate of ≈ 5 km s^{-1} kpc^{-1} and a vertical motion of the Sun of about 12.7 km s^{-1}. The latter is larger than the value $7.25^{+0.37}_{-0.36}$ km s^{-1} reported by Schönrich et al. (2010), which was obtained with the Hipparcos catalogue (containing not only OB stars). To explain these results, we suggest that the kinematics of our OB sample is more complex than the simple assumptions made in our model. As discussed in Section 4.2, systematic motions such as vertical waves or breathing modes (Widrow et al., 2012; Williams et al., 2013; Xu et al., 2015) could be excited by tidal interaction with a satellite (Gómez et al., 2013; Laporte et al., 2016; Widrow et al., 2014), as well as caused by the bar and the spiral arms (Monari et al., 2015, 2016). Considering that the OB stars are a young and dynamically un-relaxed stellar population, any perturbation acting on the gas would be inherited by the kinematics of our OB sample. Finally, our modelling of the warp might be not appropriate: rather than static ($\omega_p = 0$ km/s/kpc) or precessing ($\omega_p \neq 0$ km/s/kpc), the warp might be an unstable structure, consistent with a disc in a non-equilibrium state (Antoja et al., 2018).

To conclude, our analysis suggests that our simple model is not sufficient to explain the kinematics of OB stars in the TGAS catalogue. We speculate that this is due to additional systematic motions, possibly caused by forces acting on the gas. If confirmed, these results inspire further questions on the nature of the possible perturbing agent and on its connection with the kinematic signature of warp. Alternatively, our results can be explained if the warp is an unstable structure, and our precessing warp model is not appropriate. The second *Gaia* data release, providing us with an unprecedented amount of data with exquisite astrometry, will allow us to map the stellar kinematics out to a few kiloparsec from the Sun and possibly disentangle the large-scale kinematic signature of the warp from other perturbation effects.

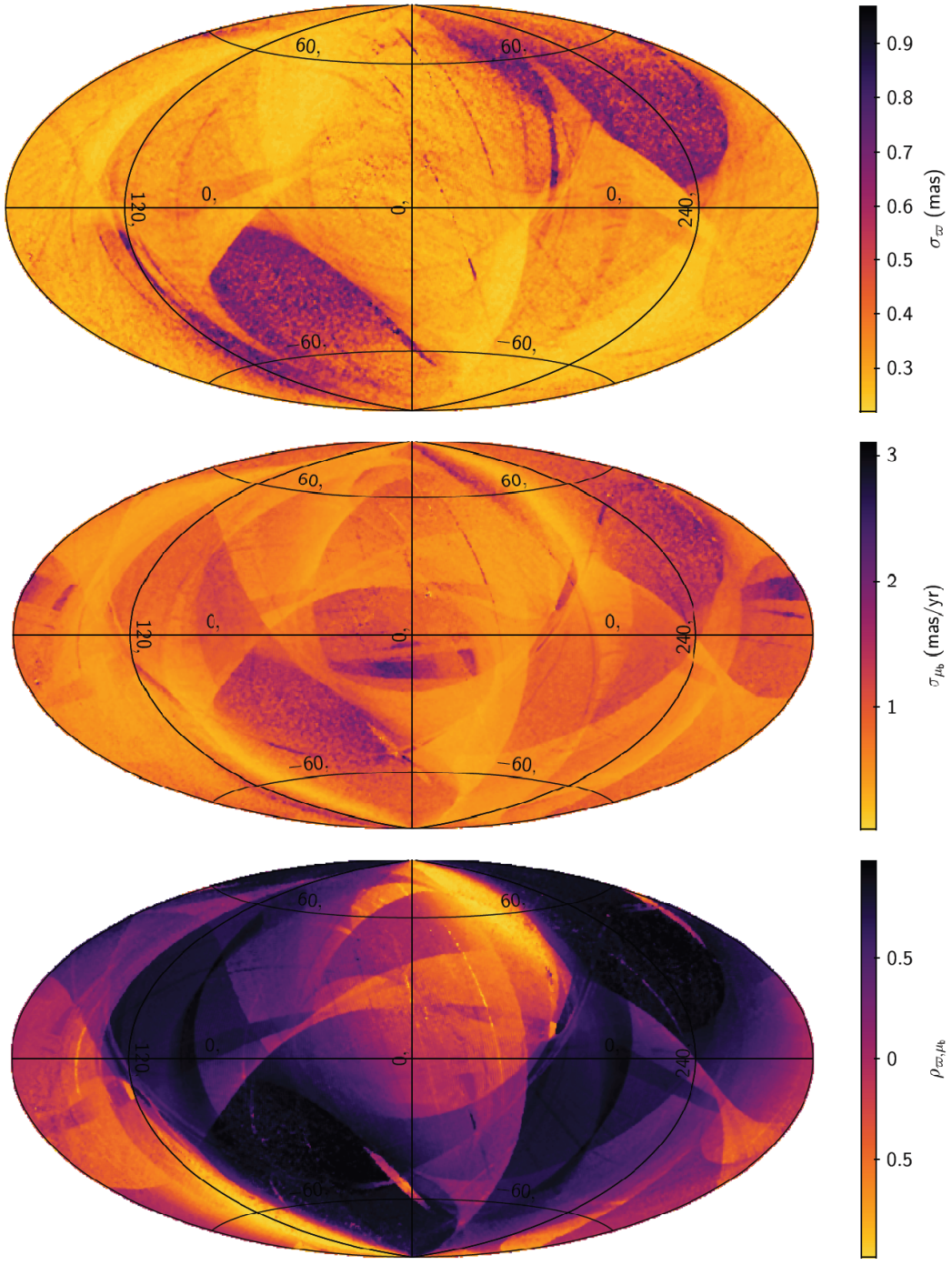

Figure 7.1: Aitoff projections (Healpix level 6) in Galactic coordinates showing the parallax (top) and proper motion (middle) uncertainties, together with their correlations (bottom), for the TGAS stars.

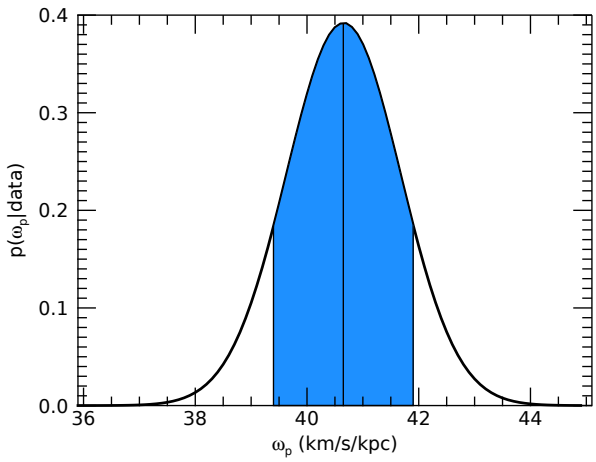

Figure 7.2: The posterior probability distribution for the warp precession rate ω_p. The blue shaded area indicates the region between the 10^{th} and the 90^{th} percentiles of the distribution. The median, the mode and the mean of the distribution coincide and are shown by the solid vertical line at 40.7 km s^{-1} kpc^{-1}.

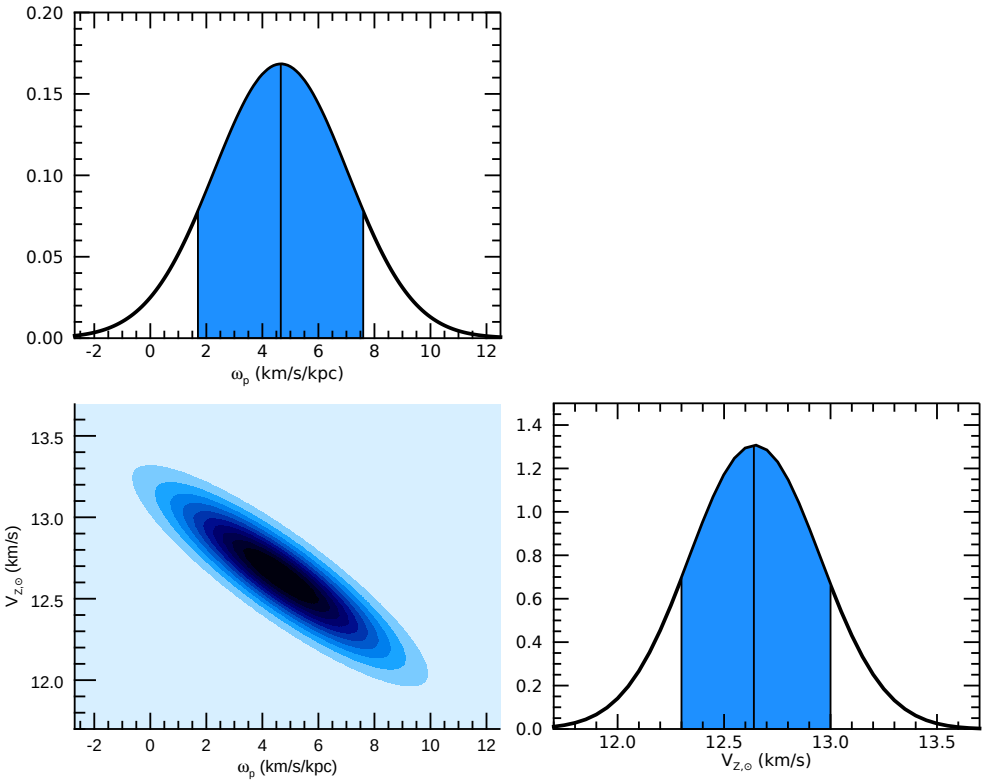

Figure 7.3: Marginalized posterior distribution for the warp precession rate ω_p (top left panel) and for the vertical component of the solar motion $V_{z,\odot}$ (bottom right panel). The colored area shows the portion of the distribution between the 10^{th} and the 90^{th} percentiles, while the vertical line shows the median. The contour plot (bottom left plot) shows the posterior distribution in the parameter space (the darkness is proportional to probability).

Part IV

The kinematic signature of the Galactic warp: *Gaia* DR2

CHAPTER 8

Gaia DATA RELEASE 2: MAPPING THE MILKY WAY DISC KINEMATICS

Due to our position in the Galactic disc, the large-scale mapping of the Milky Way represents a challenging task. To this end, large and precise astrometric catalogues are needed. The second *Gaia* data release (*Gaia* DR2, Gaia Collaboration et al., 2018a) provides the five-parameter astrometric solution for 1.3 billions sources down to magnitude $G \sim 21$ mag, enabling the scientific community to derive distances for an unprecedentedly large number of stars. Moreover, *Gaia* DR2 contains line-of-sight velocities for 7.2 million stars brighter than $G_{\rm RVS} = 12$ mag. *Gaia* DR2 was accompanied by six performance verification papers, aimed at demonstrating the scientific potential of the catalogue through a basic examination of some of the key science cases of the *Gaia* mission. The performance verification papers include Gaia Collaboration et al. (2018b), which is dedicated to the Milky Way disc kinematics. The present Chapter is based on my contribution to the results reported by Gaia Collaboration et al. (2018b); we refer the reader to the original paper for a complete overview of the Galactic disc kinematics with *Gaia* DR2. We here focus on the velocity perpendicular to the Galactic disc, which contains key information on the dynamical nature of the Galactic warp. In this context, we compare the results for two samples of stars having different typical ages. The unprecedented volume of *Gaia* DR2 data with exquisite astrometry allow us to map the kinematics of the disc out to a few kiloparsec from the Sun. In the following, we describe the data (Section 8.1), map the vertical velocities (Section 8.2) and discuss the results (Section 8.3).

8.1 The data

After a brief overview of *Gaia* DR2 data (Section 8.1.1), we describe how distances, velocities, and their uncertainties are calculated (Section 8.1.2). Finally, we describe the selection of the samples used in the present analysis (Section 8.1.3).

8.1.1 DR2 data overview

The *Gaia* DR2 catalogue contains 1.3 billion sources with full astrometric information (positions, parallaxes, and proper motions). For bright sources (G<15 mag), the typical uncertaintiy is 0.03 mas for the parallax and 0.07 mas yr^{-1} for the proper motions (Gaia Collaboration et al., 2018a). Figure 8.1.1 (from Gaia Collaboration et al., 2018a) shows the variation of the parallax uncertainty as a function of apparent magnitude G, compared to *Gaia* DR1. The reference frame is aligned with the International Celestial Reference System (ICRS) and non-rotating with respect to the quasars to within 0.1 mas yr^{-1}. The systematics are below 0.1 mas and the parallax zeropoint uncertainty is about 0.03 mas. Further details on the the astrometric content and quality of *Gaia* DR2 are reported in Lindegren et al. (2018a) and Arenou et al. (2018).

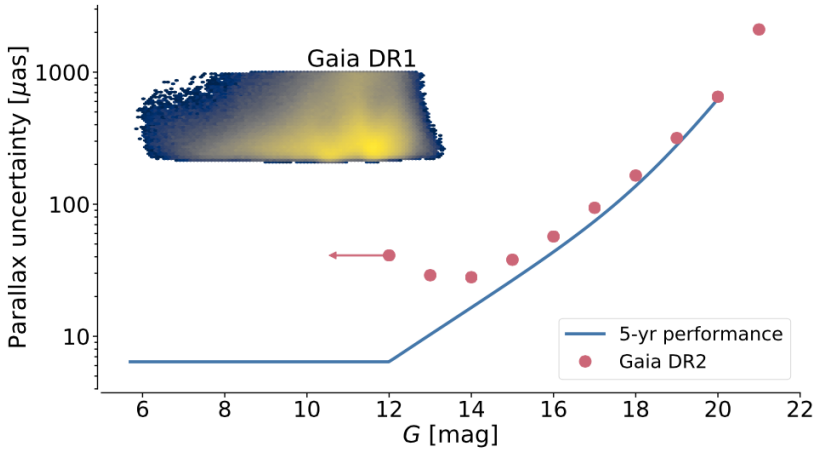

Figure 8.1: From Gaia Collaboration et al. (2018a): Parallax uncertainties in Gaia DR2 (dots) as a function of G compared to the uncertainties quoted for Gaia DR1 (colour scale) and the expected end-of-mission parallax performance (solid line), as predicted after the commissioning of Gaia. Note how the performance for Gaia DR2 is still limited by calibration uncertainties for sources brighter than G ≃ 14.

Gaia DR2 also provides photometric information in the G, $G_{\rm BP}$, and $G_{\rm RP}$ passbands. The precision at $G = 12$ (which is the most relevant magnitude for this Chapter, see below) is around 1 mmag or better for all three passbands. The photometric content of *Gaia* DR2 is described in Evans et al. (2018). To select specific stellar populations (Section 8.1.3), we also used the extinction

A_G and color excess $E(G_{\rm BP}-G_{\rm RP})$ provided in *Gaia* DR2, whose estimation is described in Andrae et al. (2018). Additionally, we made use of 2MASS photometry of the *Gaia* sources, specifically, of the *Gaia*/2MASS cross-match provided in the *Gaia* Archive[1] (see Marrese et al. 2018).

Gaia DR2 contains line-of-sight velocities[2] for 7.2 million stars brighter than $G_{\rm RVS} = 12$ mag, that were observed with the *Gaia* Radial Velocity Spectrometer (Cropper et al., 2018). Line-of-sight velocities in *Gaia* DR2 are provided for stars with effective temperatures in the range $\sim [3550, 6900]$ K, while cooler and hotter stars will be included in future *Gaia* releases. Details about the Gaia spectroscopic processing pipeline and the *Gaia* DR2 line-of-sight velocities can be found in Katz et al. (2018) and Sartoretti et al. (2018).

8.1.2 Calculation of distances, velocities, and uncertainties

To map the kinematics of the Galaxy, we derive distances from *Gaia* astrometry. We select from *Gaia* DR2 only stars with $\varpi/\sigma_\varpi > 5$ and adopt $1/\varpi$ as our distance estimate. With the cut in ϖ/σ_ϖ, we select stars with positive parallaxes and a relative parallax uncertainty smaller than 20%. This generates a cut in apparent magnitude and other minor selection effects. Using a set of simulations, Gaia Collaboration et al. (2018b) verified that it doesn't introduce relevant artifacts in the kinematics. Moreover, Gaia Collaboration et al. (2018b) established that inverting the parallax for stars with $\varpi/\sigma_\varpi > 5$ leads to unbiased distances out to about 1.5 kpc, with overestimates of the order of 17% at 3 kpc (see Arenou and Luri, 1999; Brown et al., 1997; Luri et al., 2018, for a discussion on the well-known bias caused by inverting the parallax in case of large fractional error). The impact of biased distances on vertical velocities is studied in Section B of this Thesis.

For a proper treatment of parallaxes, Bayesian methods might be used to infer distances (e.g. Bailer-Jones, 2015; Bailer-Jones et al., 2018), as done in Chapter 9 of this Thesis. However, Bayesian methods require fixing a prior, and also a numerical treatment to derive distance estimates or confidence intervals. In this exploratory study, we chose to select small uncertainty in parallax, since it is simpler and serves the purposes of our work well.

From *Gaia* DR2 we use the five astrometric parameters[3] $(\alpha, \delta, \varpi, \mu^*_\alpha, \mu_\delta)$ and line-of-sight velocities V_{los} [4], together with their associated uncertainties and correlations. Hence, we derive the positions and velocities in Galactocentric cylindrical coordinates $(R, \phi, Z, V_R, V_\phi, V_Z)$[5], where ϕ is positive in the direction of Galactic rotation and $\phi = 0^o$ coincides with the line Sun-Galactic centre. We also use Cartesian Galactic coordinates, with the Sun located at the X negative axis.

[1] *Gaia* Archive: http://gea.esac.esa.int/archive

[2] We use the term "line-of-sight velocity" for the Doppler-shift measured from the spectra and "radial velocity" for the Galactocentric velocity component V_R defined in Sect. 8.1.2.

[3] Proper motion in right ascension $\mu^*_\alpha \equiv \mu_\alpha \cos\delta$ of the source in ICRS at the reference epoch. This is the projection of the proper motion vector in the direction of increasing right ascension.

[4] Line-of-sight velocities will be used only for the sample containing giant stars, as explained in the following.

[5] As already stated before, we only show here the median vertical velocities V_Z in the Galactic plane. For additional analysis on all three velocity components, see Gaia Collaboration et al. (2018b).

For these transformations, we used $Z_\odot = 27$ pc for the height of the Sun above the plane (Chen et al., 2001), $R_\odot = 8.34$ kpc for the distance of the Sun to the Galactic centre and $V_c = 240\ \mathrm{km\,s^{-1}}$ for the circular velocity at the solar radius of (Reid et al., 2014). For the solar motion with respect of the local standard of rest, we adopted $(U_\odot, V_\odot, W_\odot) = (11.1, 12.24, 7.25)\ \mathrm{km\,s^{-1}}$ from Schönrich et al. (2010). The resulting value of $(V_c + V_\odot)/R_\odot$ is $30.2\ \mathrm{km\,s^{-1}\,kpc^{-1}}$, which is compatible with the value from the reflex motion of Sgr A* of Reid and Brunthaler (2004). The full covariance matrix of the astrometric parameters was propagated to Galactocetric cylindrical and Cartesian coordinates.

8.1.3 Data selection

We here focus on two of the samples considered in Gaia Collaboration et al. (2018b), which contain OB and giant stars. The selection of the two samples is reported in the following.

OB sample. We here describe the selection of OB stars used to map the median vertical velocity of young stellar populations in Section 8.2. For the OB stars, we do not require the availability of *Gaia* DR2 line-of-sight velocities, since they lie outside the range of effective temperatures considered in this data release (see Section 8.1.1). Hence, the vertical velocity will be approximated as explained in Section 8.2. An initial list of OB star candidates in DR2 was found using the following criteria:

$$\varpi/\sigma_\varpi > 5 \tag{8.1}$$

$$(G_{BP} - G_{RP})_0 = (G_{BP} - G_{RP}) - E(G_{BP} - G_{RP}) < 0 \tag{8.2}$$

$$M_G = G + 5\log\varpi + 5 - A_G < 2, \tag{8.3}$$

where A_G and $E(G_{BP} - G_{RP})$ are the extinction and colour excesses provided in *Gaia* DR2 (see Andrae et al. 2018), and ϖ is expressed in mas. To ensure that our sample indeed consists of young stars rather than giants or red clump stars with erroneous extinctions, a further selection was made using the 2MASS photometry that also satisfies the following conditions:

$$J - H < 0.14(G - K_s) + 0.02 \tag{8.4}$$

$$J - K_s < 0.23(G - K_s). \tag{8.5}$$

These colour-colour selection criteria were adopted from those described in Chapter 5 of this Thesis and are based on the observed 2MASS colours of spectroscopically bona fide OB stars from the *Tycho*-2 stars found in *Gaia* DR1 and the *Tycho*-2 spectral type catalogue (Wright et al., 2003). In addition, the photometric quality conditions $\sigma_{J,H,K_s} < 0.05$ and 2MASS photometric flag equal to AAA were applied to avoid sources with problematic photometry. These selections yielded 285 699 stars whose 2MASS/*Gaia* colours and astrometry are consistent with our sources being OB stars. However, given the relatively large uncertainties on the individual extinction

parameters, our sample is likely to also contain a significant number of upper main-sequence A stars. Nevertheless, such stars, being young, still serve our purpose here.

Giant sample. Considering *Gaia* DR2 stars with available astrometry, line-of-sight velocities, and $\varpi/\sigma_\varpi > 5$, a preliminary selection of 6 376 803 sources is performed. The requirement of the line-of-sight velocity is fundamental to derive the three velocity components V_R, V_ϕ, V_Z used in Gaia Collaboration et al. (2018b) (but we will show here only V_Z, see above). To select giant stars, the Herzprung-Russel diagram has been constructed by deriving absolute magnitudes and intrinsic colours for each source, based on *Gaia* and 2MASS photometry. Details can be found in Section 2.3 of Gaia Collaboration et al. (2018b). Stars are selected as giant candidates if they present absolute magnitude in G band $M_G < 3.9$ and intrinsic colour $(G_{\rm BP} - G_{\rm RP})_0 > 0.95$. The selected sample contains 3 153 160 sources, which is approximately the half of the 6 376 803 initial sources.

8.2 Mapping the disc median vertical velocities

We here present Galactocentric Cartesian XY-maps (face-on view) of the median vertical velocities for stars with Z-coordinates in the range $[-200, 200]$ pc (Figure 8.2 and 8.3). The XY plane is divided into cells of 200 pc by 200 pc, containing at least 30 stars. The maps are (roughly) centered on the Sun position $(X, Y) = (-8.34, 0)$ kpc, and the Galactic centre is located on the left side. The Milky Way rotates clockwise.

As discussed in the previous Chapters, the kinematics perpendicular to the Galactic disc is expected to reflect the large-scale warp. In particular, we expect to observe an associated kinematic signature, apparent as a systematic increase of the vertical velocities towards the Galactic anti-centre. Figure 8.2 shows the median vertical velocity for the young OB sample. As mentioned before, line-of-sight velocities are not available for this sample (see Section 8.1.1, 8.1.3 and Katz et al. (2018) for details), so that we cannot directly calculate V_Z for each star. However, at low Galactic latitudes, we can estimate a V_Z' since most of the vertical motion is seen in the proper motions perpendicular to the Galactic plane. The vertical velocity

$$V_Z = \frac{4.74\mu_b}{\varpi \cos b} + W_\odot + (S - S_\odot)\tan b, \tag{8.6}$$

where $S_\odot = U_\odot \cos l + V_\odot \sin l$, and similarly for S, which contains both differential Galactic rotation and the peculiar motion of the star parallel to the Galactic plane, S_*. Neglecting the latter and assuming a flat rotation curve, we estimate V_Z' by taking $S \approx V_{LSR}(R_\odot/R - 1)\sin l$ in the above equation. Using stars in the OB sample within 200 pc of the Galactic plane, we map the median V_Z', shown in Figure 8.2 (our approximation means that we have effectively ignored a $\langle S_* \tan b \rangle$ for each cell). The obtained map shows no signs of a warp signature, with important implications, as discussed in Section 8.3.

It is worth comparing the median vertical velocities of the young OB sample with a similar map obtained with the older giants, shown in Figure 8.3. The vertical trends of the giant sample appear to be distinctly different from the map for the OB sample, and indeed seems to exhibit a systematic vertical velocity of about 2-3 $\mathrm{km\,s^{-1}}$ at $R = 10-11$ kpc in the direction of the Galactic anti-centre. The median uncertainty of the vertical velocity is 1.2 $\mathrm{km\,s^{-1}}$, and 13% of the stars of the sample have an uncertainty in all velocity components that is smaller than 1 $\mathrm{km\,s^{-1}}$. In the midplane $Z = [-200, 200]$ pc, the velocity dispersions decrease mildly with increasing Galactocentric radius (here not shown, see Gaia Collaboration et al., 2018b), with a significantly stronger gradient for larger Z.

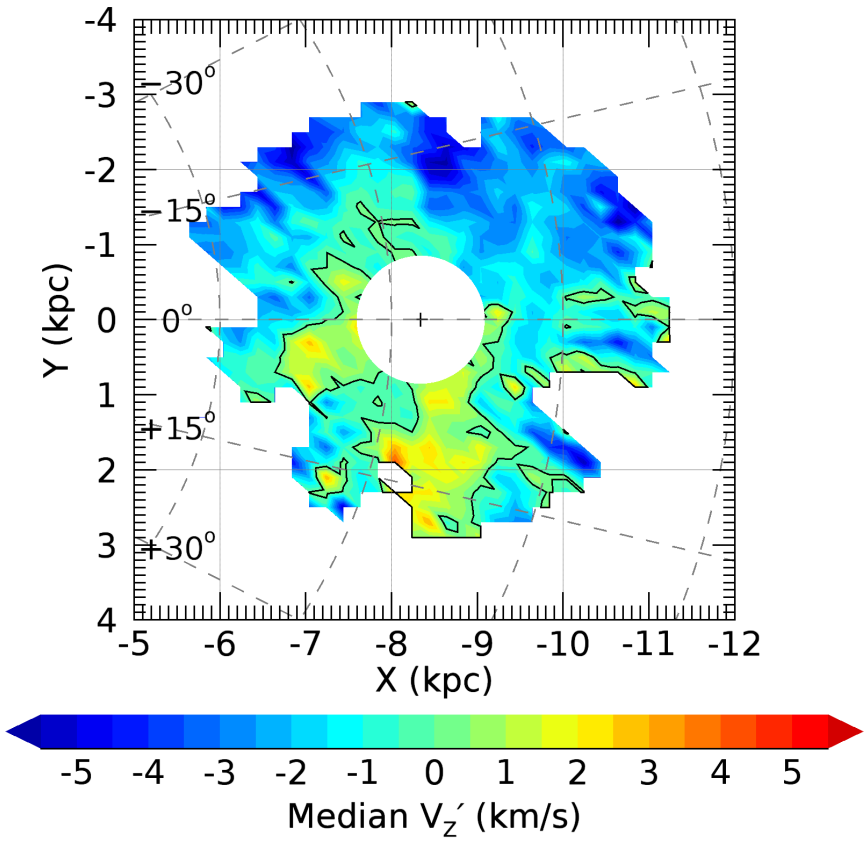

Figure 8.2: Median vertical velocity V_Z' of the OB sample in the disc midplane ($Z = [-200, 200]$ pc) for the 200 098 stars with $|Z| < 200$pc and $|b| < 15°$. The black cross shows the position of the Sun, and the white area around the Sun masks the region where the height of a 200 pc cell has a Galactic latitude $b > 15°$. The azimuths increase clockwise. They are labelled from −30 to +30 degrees, on the left of the maps. The Sun is represented by a black dot at $X = -8.34$ kpc and $Y = 0$ kpc. The Galactic centre is located on the left side. The Milky Way rotates clockwise. The iso-velocity contours $V_Z' = 0$ km s^{-1} are shown as black lines.

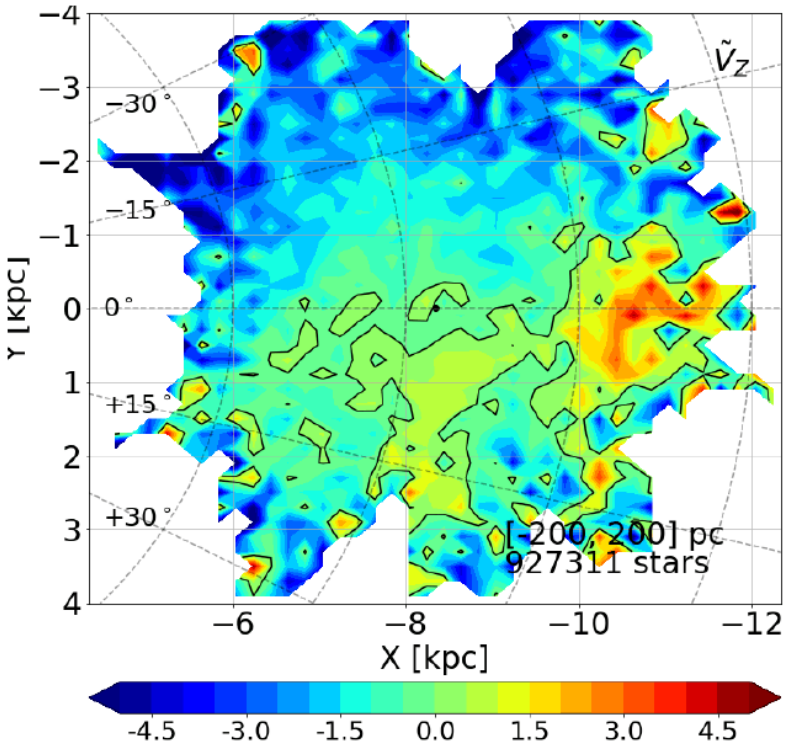

Figure 8.3: Face-on view of the kinematics of the disc mid-plane ([-200, 200] pc) derived using the giant sample, showing the median vertical velocity $\tilde{V}_Z$ (in $\mathrm{km\,s^{-1}}$). Orientation and coordinates are the same as in Fig. 8.2. The iso-velocity contour $\tilde{V}_Z = 0$ $\mathrm{km\,s^{-1}}$ is pointed out as black lines.

8.3 Discussion

Taking advantage of the large data volume, full sky coverage, accuracy, and precision of *Gaia* DR2, we mapped the vertical velocity field of the Galaxy over a large portion of the disc ($5 \leq R \leq 13$ kpc) for more than three million giant stars and approximately two hundred thousand OB stars. The comparison of the vertical motions of young and old stellar populations can provide important clues on the dynamical nature of the warp. We recall that the OB sample is expected to trace the motions of the gas from which these stars have recently been born. Thus, the lack of any warp signature in the OB vertical velocities suggests that either the warp is an unstable transient feature, or that additional perturbations are acting on the gas. This is consistent with previous results obtained with OB stars in *Gaia* DR1 (Chapter 4 and 7 of this Thesis, Poggio et al., 2017) and pre-*Gaia* astrometry (Drimmel et al., 2000; Smart et al., 1998). The map of the OB stars is considerably different from the one obtained with the giants. The latter exhibit an increase of the vertical velocities toward the Galactic anticenter, as expected from a warp signature. However, this signal is weaker than expected from current empirical descriptions of the stellar warp, which assume the warp to be stable and non-precessing, and might indicate that the warp is

instead an unstable transient feature. Finally, it is worth mentioning that, in addition to the warp, non-axisymmetric structures (e.g. bar and spiral arms) and external perturbers (e.g. the Sagittarius dwarf galaxy and the Magellanic Clouds) are expected to disturb the Milky Way velocity field. Such perturbations are observed in the vertical velocity field of the *Gaia* DR2, which appears to be quite complex, and bears witness that the Milky Way is not an axysimmetric system at equilibrium (see Gaia Collaboration et al., 2018b).

CHAPTER 9

THE GALACTIC WARP REVEALED BY *Gaia* DR2 KINEMATICS

Theoretical models for the warping of stellar discs include interactions with satellites intergalactic magnetic fields (Battaner et al., 1990), accretion of intergalactic matter (Kahn and Woltjer, 1959; López-Corredoira et al., 2002a), and a mis-aligned dark halo (Debattista and Sellwood, 1999; Sparke and Casertano, 1988), amongst others. However, to date only the shape of the Galactic warp has been roughly constrained, leading to a lack of consensus for its causal mechanism due to the lack of kinematic information perpendicular to the galactic disc. In particular, a consistent kinematic signature in old and young stars would exclude non-gravitational mechanisms (see Section 9.3). In the pre-*Gaia* era, kinematic studies suggested a signature inconsistent with a long-lived warp Drimmel et al. (2000); López-Corredoira et al. (2014); Smart et al. (1998), while the kinematics of stars near the Sun seemed to be consistent with the presence of a warp (Dehnen 1998, though see Seabroke and Gilmore 2007). With the first *Gaia* data release, Schönrich and Dehnen (2018) detected the warp kinematic signature using the TGAS catalogue, while Poggio et al. (2017) found no evidence of the warp signal in the kinematics of OB stars.

With *Gaia*'s most recent second data release, Gaia Collaboration et al. (2018b) (hereafter MWDR2, see Chapter 8) showed a kinematic signature on large scales consistent with a warp with a sample of red giants (in agreement with LAMOST radial velocities, Liu et al., 2017), while their young OB stellar sample seemed to give divergent results. In this contribution we expand on the work of MWDR2, with larger and fainter samples of the old (red giants) and young (upper main sequence stars) selected from *Gaia* DR2, using 2MASS (2-Micron All Sky Survey, Skrutskie et al., 2006) photometry, following the technique presented in Chapter 5. We identify 599 494 upper main sequence stars and 12 616 068 giants without the need for individual extinction estimates (see Section 9.1). We find that the large-scale kinematics of both the upper main

sequence and giant populations show a clear signature of the warp of the Milky Way, apparent as a gradient of 5-6 km/s in the vertical velocities from 8 to 14 kpc in Galactic radius (see Section 9.2). The presence of the signal in both samples, which have different typical ages, resuggests that the warp is a gravitationally induced phenomenon (see Section 9.3).

The present Chapter is based on the results presented in Poggio et al. (2018a), and contains supplementary material, that was not included in the original paper due to the page limit of the journal.

9.1 Data selection

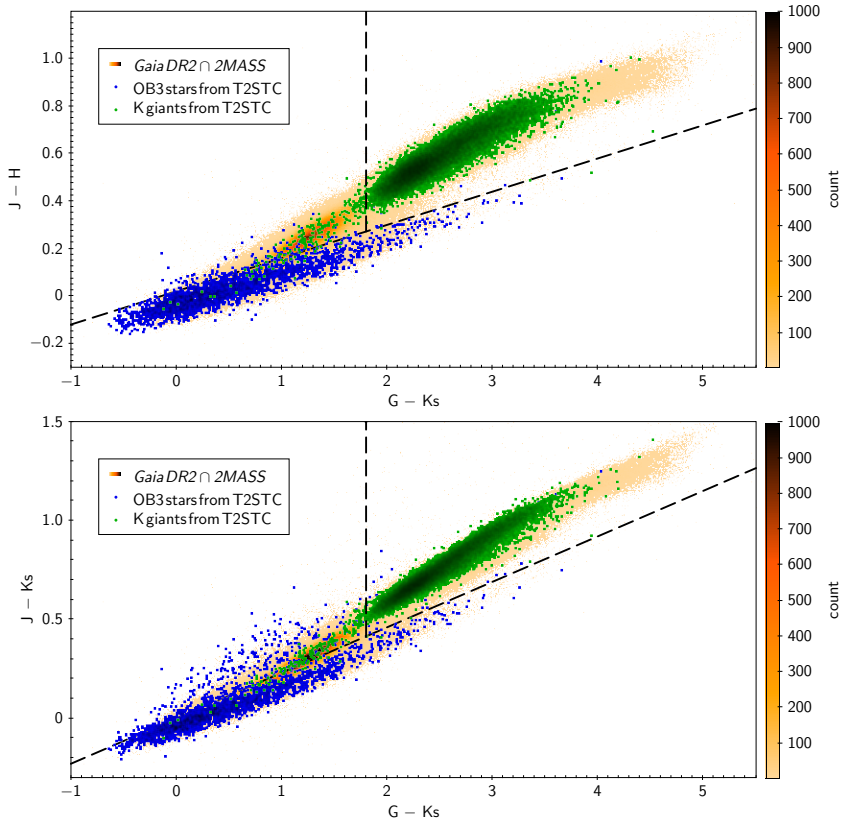

Figure 9.1: Colour-colour plots showing the 2MASS-*Gaia* preliminary selection. Candidate upper main sequence (UMS) are taken as stars lying below the diagonal dashed line, while candidate giants are those lying in the top right area of the plots. The yellow-orange density plots a sample of *Gaia* DR2 stars with $G < 12$, while the blue and green points show the colours of stars in the Tycho-2 Spectral Type Catalogue (T2STC) that are classified as either OB stars or K giants (luminosity class I and II).

To select upper main sequence (UMS) and giants in the Galactic plane ($|b| < 20\,\mathrm{deg}$) without the need for individual reddening estimates, we use 2MASS photometry for *Gaia* DR2 sources

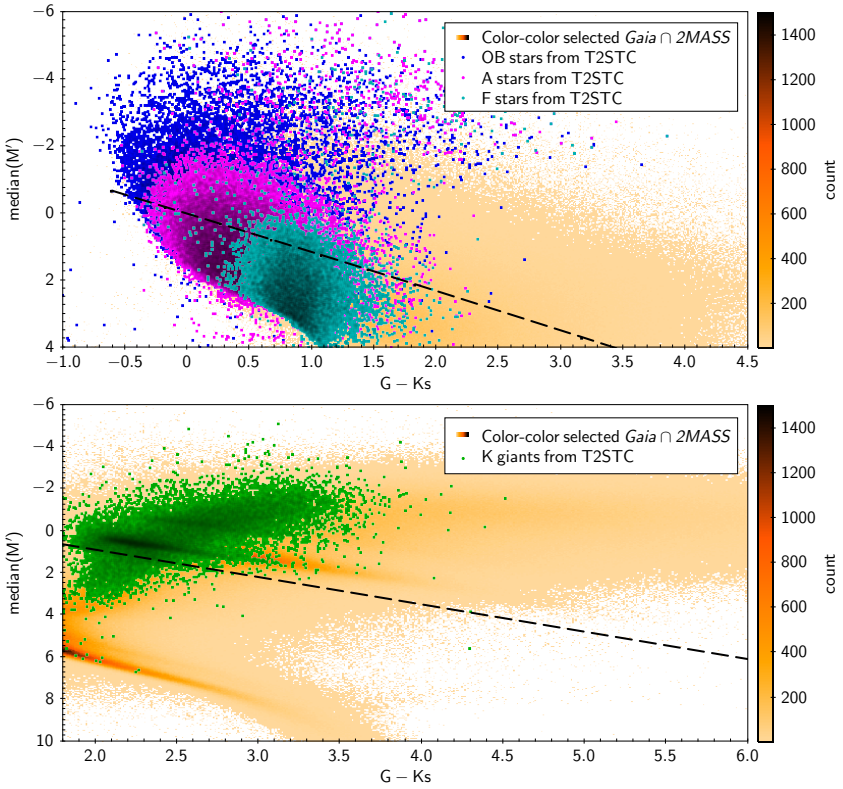

Figure 9.2: The parallax criterium for the UMS (top panel) and for the giants (bottom panel). On the y-axis, the median of the probability density function of M'. The dashed line shows the adopted tolerance limit (see text), selecting those stars that are above the dashed lines. Orange density area as in the previous plot, other coloured points are for those stars in the Tycho-2 Spectral Type Catalogue (T2STC), colour coded as per the key in the figures.

using the cross match table provided by the *Gaia* Archive (`https://archives.esac.esa.int/gaia`), and restricting ourselves to 2MASS sources with uncertainties $\sigma_{J,H,K_s} < 0.05$ mag and a photometric quality flag of "AAA". Finally, as a practical matter, we select stars with $G < 15.5$ mag, as very few fainter stars have 2MASS photometry.

Upper Main Sequence stars.[1] A preliminary selection is made based only on measured 2MASS/*Gaia* colours. As shown in Figure 9.1, known OB stars from the Tycho-2 Spectral Type Catalogue (hereafter T2STC, Wright et al., 2003) lie along a sequence that is a consequence of interstellar reddening, which is clearly separated from the redder turn-off stars, giants and lower main sequence stars. Based on this, candidates UMS stars are selected from the Gaia DR2∩2MASS catalogue satisfying both $(J-H) < 0.14(G-K_s)+0.02$ and $(J-K) < 0.23(G-K_s)$.

A second step of the selection procedure uses *Gaia* astrometry (Lindegren et al., 2018b),

[1]The selection technique for the Upper Main Sequence stars follows the one presented in Section 5.1, though with some minor differences (e.g. a more sophisticated prior for the heliocentric distance). For reasons of clarity, we here provide a detailed description, at the risk of being repetitive.

choosing those stars whose parallax ϖ, parallax uncertainty σ_ϖ and apparent G magnitude is likely to be consistent with being a UMS star. To this end, we calculated the probability density function (pdf) of the heliocentric distance r for the given coordinates (l,b) via Bayes' theorem, $P(r|l,b,\varpi,\sigma_\varpi) \propto P(\varpi|r,\sigma_\varpi)P(r|l,b)$, assuming a gaussian likelihood $P(\varpi|r,\sigma_\varpi)$ and constructing the prior according to Astraatmadja and Bailer-Jones (2016) (their Equation 7, i.e. the Milky Way prior)

$$P(r|l,b) \propto r^2 \rho(l,b,r) S(l,b,r) \quad . \tag{9.1}$$

We adopt a simple density model for the Galactic disc $\rho(l,b,r)$, consisting of an exponential disc in Galactocentric radius R and vertical height z, with a radial scale length $L_R = 2.6$ kpc (Bland-Hawthorn and Gerhard, 2016) and vertical scale height $h_z = 150$ pc (larger than the known scale height for OB stars, Poggio et al., 2017). We assume for the Sun $R_\odot$=8.34 kpc (Reid et al., 2014) and $z_\odot = 25$ pc (Bland-Hawthorn and Gerhard, 2016). The term $S(l,b,r)$ takes into account the fall-off of the number of observable objects with r due to the survey selection function, neglect of which can cause severe biases in the obtained distance estimates (Schönrich and Aumer, 2017). We estimated the term $S(l,b,r)$ according to Astraatmadja and Bailer-Jones (2016), and modelled the variation of Gaia DR2∩2MASS completeness as a function of apparent magnitude G (see Figure 9.3) according to Drimmel et al. (in prep.), including the previously mentioned cut at $G = 15.5$. The adopted luminosity function in the G band is calculated through the PARSEC isochrones (web interface `http://stev.oapd.inaf.it/cmd`, Bressan et al., 2012; Chen et al., 2014, 2015; Tang et al., 2014), after taking into account the colour-colour cuts applied in the preliminary selection. The luminosity function was obtained assuming a star formation rate constant with time, the canonical two-part power law IMF corrected for unresolved binaries (Kroupa, 2001, 2002), and solar metallicity. The impact of various assumptions incorporated in our prior is discussed in the following section.

For each star, we derived from $P(r|l,b,\varpi,\sigma_\varpi)$ a pdf of the quantity $M' \equiv M_G + A_G = G - 5\log r_{pc} + 5$, which is the absolute magnitude M_G plus the extinction in the G band of the source. The Jacobian of the transformation dr/dM' can be written when the G magnitude is fixed, obtaining $P(M'|l,b,\varpi,\sigma_\varpi,G)$. After numerically imposing the normalization condition $\int_{-\infty}^{+\infty} P(M'|l,b,\varpi,\sigma_\varpi,G)dM' = 1$, we calculate the probability of the star being brighter than the limit M'_{lim}, which is the faintest extincted magnitude that we are willing to tolerate for an UMS star candidate with an observed $(G-K_s)$ colour. The tolerance limit M'_{lim} was arbitrarily chosen as the absolute magnitude of a fictitious B3-like star having log(age/yr) = 6 and $\log(T_{eff}) = 4.27$. For such a star, the PARSEC isochrones provide us with an absolute magnitude of $(M_G)_{lim} = -0.7$ and $(G-K_s) = -0.6$ in the case of no extinction. The PARSEC isochrones give the corresponding values of M'_{lim} and $(G-K_s)$ when extinction is present (Figure 9.2, left plot). Hence we calculate the probability of the star being an UMS star - i.e. brighter than the tolerance limit - by performing

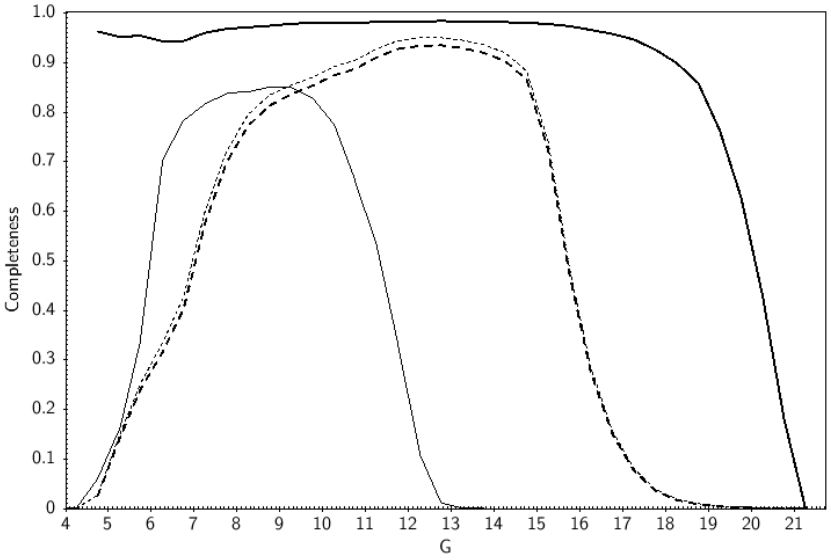

Figure 9.3: From Drimmel et al. (in prep.): Completeness of the *Gaia* DR2 sources with five-parameter astrometric solution (thick solid line), of 2MASS (dotted line), 2MASS∩DR2 (dashed line) and TGAS (thin solid line).

the following integral

$$p(UMS\,|\,l,b,\varpi,\sigma_\varpi,G) = \int_{-\infty}^{M'_{lim}} P(M'|l,b,\varpi,\sigma_\varpi,G)\,dM', \tag{9.2}$$

which is by definition between 0 and 1. The stars for which $p(UMS\,|\,l,b,\varpi,\sigma_\varpi,G) > 0.5$ are selected, giving us 599 494 UMS stars.

Giant stars. In a similar fashion as the colour-colour selection of the UMS stars, we perform a preliminary selection based on photometry, this time selecting the stars with $(J-H) > 0.14(G-Ks)+0.02$ and $(J-Ks) > 0.23(G-Ks)$ (see Figure 9.1), with an additional $(G-Ks) > 1.8$ cut to remove the objects too blue to be considered giant candidates. We adopt the same probabilistic approach used for the UMS stars, but assuming a spatial density scale height of h_z =300 pc (Bland-Hawthorn and Gerhard, 2016). We calculate for each source the probability of being a giant star, with the tolerance limit set as equal to $M'_{lim} = 1.3(G-Ks)-1.7$. Such a limit removes sub-giants and dwarfs, and also accounts for interstellar reddening (see Figure 9.2, right plot). This selection gives us 12 616 068 giants.

To test the composition of the selected samples, we crossmatched our samples with the T2STC. For the UMS sample, we obtained 24 422 objects, of which approximately 55% are OB stars, 40% are A stars and 5% are F stars, according to the T2STC spectral classifications. For the giant sample, we found 33 842 stars with complete spectral classification from T2STC, of which 88% are giants (69% K giants and 19% G giants) and 12% are main sequence stars (mostly of spectral class K or G, while A or F stars are less than 1%).

9.2 Density and kinematic maps

In this Section, we present and compare the maps obtained with the UMS and giant samples, shown in Figure 9.4. For both samples we use as our distance estimator for each star the mean (see for example Gelman et al., 1995; MacKay, 2003) of the posterior distribution $P(r\,|\,l,b,\varpi,\sigma_\varpi)$ (see previous section). The UMS stars have mean distances of approximately 3 kpc, and mean heights with respect to the Galactic plane of about 100 pc, in contrast to the giant sample, which presents, respectively, 4.5 kpc and 480 pc. The giant sample exhibits a smooth density distribution (Figure 9.4B), decreasing for large heliocentric distance, as expected for a magnitude limited sample, and for larger Galactocentric radii, as expected from an exponential disc. In contrast the UMS sample (Figure 9.4A and 9.5) shows three observed overdensities that correspond to sections of the nearby spiral arms (from left to right: Sagittarius-Carina arm, local arm and Perseus arm). The evident spiral structure confirms that our UMS sample is young with respect to the smooth distribution shown by the older and dynamically relaxed giant population.

Figure 9.4C and 9.4D show a face-on view of the vertical motions in the Galactic plane of the two samples, calculated deriving the proper motions in galactic latitude μ_b from the *Gaia* DR2 astrometry and correcting for the solar motion $(V_{X\odot}, V_{Y\odot}, V_{Z\odot}) = (11.1, 12.24, 7.25)$ km s^{-1} (Schönrich et al., 2010). The large majority of stars in our UMS sample lack line-of-sight velocities, so that it is not possible to calculate directly the vertical velocity. We therefore estimate the mean vertical velocity V_Z' from the available astrometry, correcting for solar motion and differential Galactic rotation, assuming a flat rotation curve ($V_c = 240$ km/s, Reid et al., 2014), as done in MWDR2 (see Equation 8 of Drimmel et al., 2000). We find that 3 042 265 of our giants have line-of-sight velocities provided in *Gaia* DR2, for which we calculate directly the vertical velocity, while for the remaining we estimate the vertical velocities as done for the UMS sample. (For the subsample of stars having line-of-sight velocities, we have verified that our approximation of using V_Z' instead of V_Z produces consistent results.)

A gradient in the median vertical velocities is apparent in Figure 9.4C and 9.4D, as expected from a warp signature (Abedi et al., 2014; Poggio et al., 2017). Also worthy to note is that the peak velocities in both samples is not exactly toward the anti-center, which is probably due to the Sun not being on the line-of-nodes. We observe that the vertical velocities in the UMS sample are more symmetric with respect the Galactic anti-center $l = 180^o$ than the giant sample. Radial features in this plot are due to uneven sampling above/below the Galactic plane due to foreground extinction (see Section 8.4.2 in the Gaia DR2 online documentation). The bootstrap uncertainties on the median velocities $\sigma^*_{V_Z}$ are shown in Figure 9.4E and 9.4F. Figure 9.6 show the variation of the vertical velocities in function of Galactic radius R. It is apparent from Figure 9.4C, 9.4D and 9.6 that the vertical velocities of the giant sample increase smoothly with R, while the UMS sample present a more perturbed pattern for $R < 12$ kpc. For both samples, the increase of the median vertical velocity is of about 5-6 km/s from $R \sim 8$ kpc to 14 kpc, with a signal-to-noise greater than 10.

The subsets of stars having $\varpi/\sigma_\varpi > 5$ (478 258 UMS stars and 6 373 188 giants) present a signal consistent with the whole sample. In order to test the robustness of the signal, we also re-calculated distances with the iterative approach of Schönrich and Aumer (2017) for $20^o < l < 340^o$, finding a consistent gradient. We also slightly modified the prior (e.g. assuming $L_R = 4$ kpc for the UMS sample or including a thick disc for the giant sample), always confirming the presence of the signal. Moreover, we verified that adopting as distance estimator the mode (following Bailer-Jones, 2015; Bailer-Jones et al., 2018; Bailer-Jones, 2017) or the median of the pdf produces consistent results. Finally, we explored the impact of a systematic zero-point error (exploring the range ± 0.080 mas) of *Gaia* DR2 parallaxes (Lindegren et al., 2018b), which only results in a contraction/expansion of the maps, but still preserves the presence of the warp signature.

9.3 Discussion and conclusions

The kinematic signature of the Galactic warp is expected to manifest itself toward the Galactic anticenter as large-scale systematic velocities perpendicular to the Galactic plane. Thanks to the large sample of stars in *Gaia* DR2 with exquisite astrometric precision, we are able to map the vertical motions over a larger extent of the Milky Way's disc than previously possible, for both an intrinsically young and old population. That our UMS sample clearly shows the spiral arms (Figure 9.5), in contrast with the giant population, confirms that it is a dynamically young population.

The observed gradient in the giants appears to be in agreement with the overall increase in vertical velocity shown by *Gaia* DR2 data in Kawata et al. (2018) and the giant sample in MWDR2 for the range in Galactocentric radius in which our studies overlap. Meanwhile, our UMS sample exhibit a more perturbed pattern than the giants at $R < 12$ kpc, in agreement with the OB sample in MWDR2, showing the warp signature at larger Galactocentric radii. However, the observed gradient in both components is smaller than the expectation from the stable warp model shown in Figure 3.1, which adopts the warp spatial parameters from Drimmel and Spergel (2001). This might indicate that the stable model is not appropriate for the warp and/or that the warp amplitude is less than expected.

The presence of the warp signature in our two samples suggests that the warp is principally a gravitational phenomenon; indeed, warp generation models exclusively based on non-gravitational mechanisms (such as magnetic fields or hydrodynamical pressure from infalling gas) would act on the gas and affect the young stars only (see also the discussion in Guijarro et al., 2010; Sellwood, 2013); recently-born stars would inherit the kinematics of the gas and trace the warp-induced kinematics until phase mixing smeared out evidence of their initial conditions. The detection of a similar warp kinematic signal in both young and old stellar populations thus suggests that gravity is the principle mechanism causing the warp. However, the two samples do present some differences on smaller scales, possibly indicating that additional perturbations or

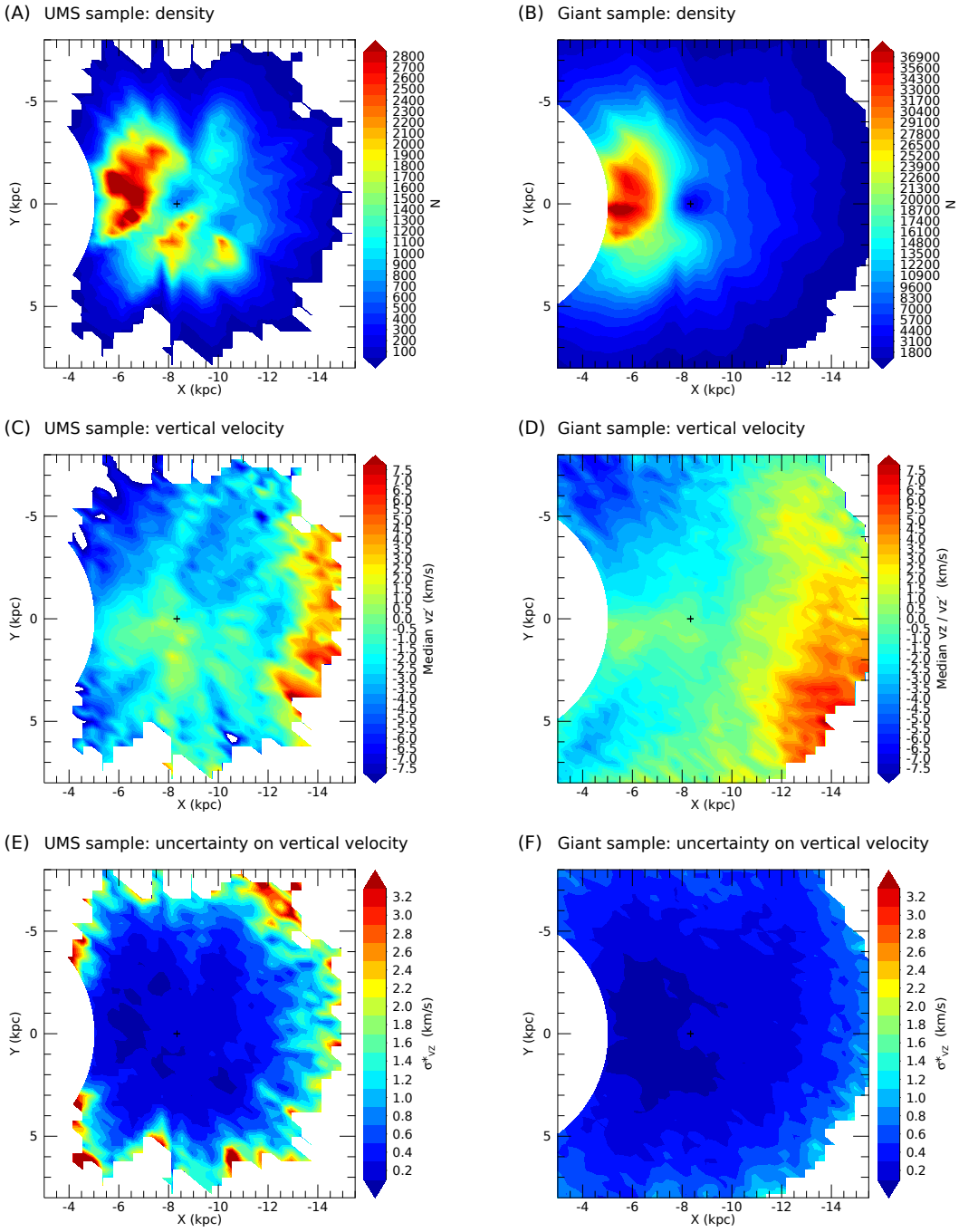

Figure 9.4: Maps for the UMS (left plots) and giant (right plots) samples. The Sun is represented by a black cross at X = -8.35 kpc and Y=0 kpc. The Galactic center is located at X=0 and Y=0, and the Galaxy is rotating clockwise. The XY plane was divided into cells of 400 pc width, only showing the ones containing more than 50/500 stars for the UMS/giant sample. From top to bottom: maps of the density (N is the number of sources per cell), median vertical velocity V_Z or V'_Z (see text) and bootstrap uncertainty on the median vertical velocity $\sigma^*_{V_Z}$.

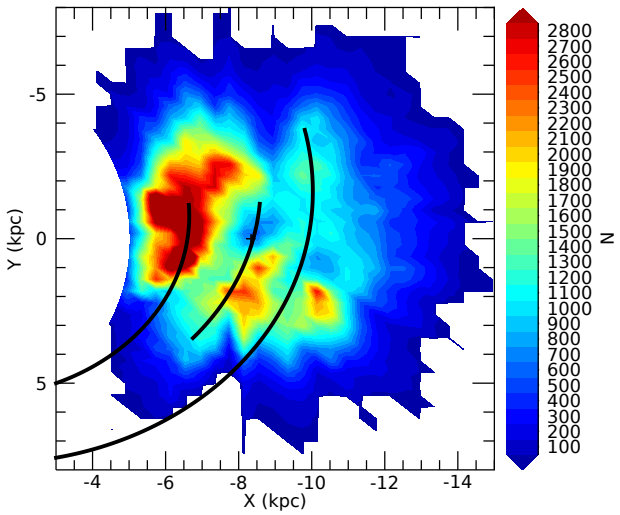

Figure 9.5: Same as Figure 9.4A, but overplotting the spiral arms from Reid et al. (2014). The three black curves show, from left to right: the Sagittarius-Carina arm, the local arm and the Perseus arm. Our mapping of the Sagittarius-Carina arm approximately coincide, while the local arm and the Perseus arm appear to be different. Possible causes for this discrepancy will be explored in future works.

forces are acting on the gaseous component of the disc (see Figure 9.7).

We have here only evidenced the kinematic signature of the warp in *Gaia* DR2. Our findings bear further witness to the great potential of this data set. Future work confronting this signature with more quantitative models will certainly reveal further details of the dynamical nature of the Galactic warp.

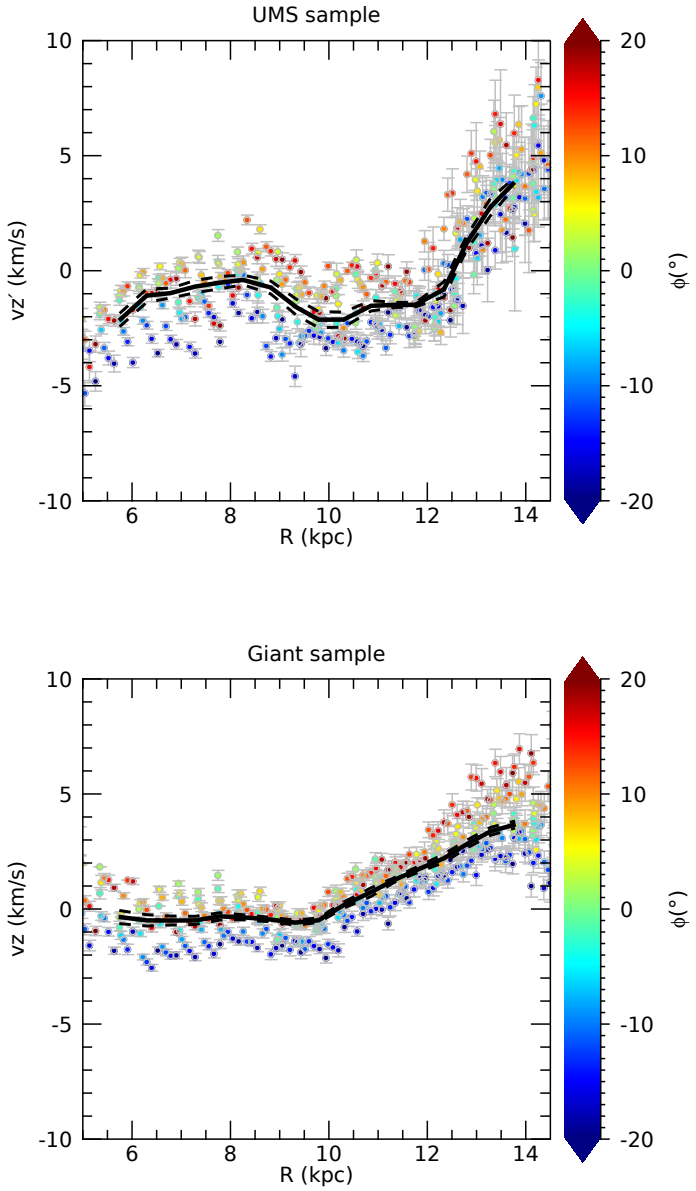

Figure 9.6: A different view of the kinematic maps shown in Figure 9.4C and 9.4D (upper and lower panel, respectively). The plots show the variation of the vertical velocity V_Z or $V_{Z'}$ in function of Galactocentric radius R for the UMS (upper panel) and the giant (lower panel) stars. Every point corresponds to a cell in the kinematic maps from Figure 9.4C and 9.4D, with the uncertainties from 9.4E and 9.4F. Points are color-colored by Galactic azimuth ϕ; we only show the cells with $|\phi| < 20^o$. The black solid line show the median of the points, while the dashed line shows the bootstrap error on the median.

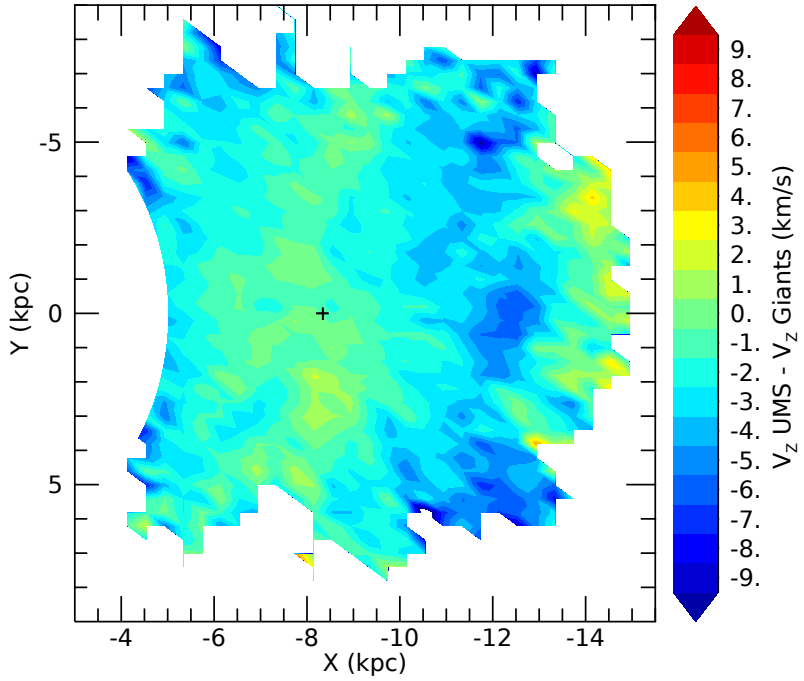

Figure 9.7: Difference in the vertical velocity maps from Figure 9.4C and 9.4D.

Part V

Conclusion

CHAPTER 10

CONCLUSION AND FUTURE WORKS

Notwithstanding the apparent simplicity of their structure, warps in disc galaxies are enigmatic features, as their nature and origin continue to remain a mystery. Our Milky Way presents the opportunity for a unique case study of galactic warps, considering that stellar motions can be studied on a star-by-star basis, potentially providing fundamental clues on the dynamical nature of the Galactic warp. The present Thesis would like to contribute to our current understanding of the Galactic warp, taking advantage of the astrometric data published in *Gaia* DR1 and *Gaia* DR2. Throughout the development of this Thesis, we acquired a progressive knowledge of the kinematics of the Galactic disc, as deduced from the different dataset analyzed in this work. The main conclusions of this Thesis are listed in the following.

1. Taking advantage of the unprecedentedly large volume of *Gaia* DR2 data with exquisite astrometry, we have mapped the vertical kinematics of the Galactic disc over a larger extent than previously possible.

2. By considering two samples of intrinsically young and old stars, we observe that they both exhibit a systematic increase of the vertical velocities of 5-6 km/s from 8 to 14 kpc in Galactocentric radius, with a signal-to-noise greater than 10. We interpret the observed gradient as the large-scale kinematic signature of the Galactic warp.

3. The presence of the signal in both populations indicates that the warp is principally a gravitational phenomenon. Indeed, purely non-gravitational warp formation mechanisms (e.g. magnetic or hydrodynamical forces) would warp only the gaseous component, whose kinematics would be inherited by young stars. However, such an evidence of an initial warp kinematic signal would by erased by phase mixing in old stellar populations. The

involvement of gravitational forces represents an important constraint on the possible warp formation scenario.

4. The warp kinematic signature is apparent in the kinematics of old stellar populations as a smooth gradient in vertical velocities, as expected from a dynamically relaxed stellar population.

5. Inside approximately 12 kpc from the Galactic center, the kinematic patterns presented by young stars are considerably more perturbed than those observed in old stellar populations. This indicates a different response of the gas (traced by young populations) and stars to a perturbative agent. Possible candidates include the interaction with non-axisymmetric features (e.g. bar and spiral arms), external perturbers (the Sagittarius dwarf galaxy and/or the Magellanic clouds), and magnetic fields.

6. The perturbed local kinematics of the young component is responsible for the observed inconsistency between warp models and OB stars in *Gaia* DR1 data (Poggio et al., 2017, 2018b) and pre-*Gaia* astrometry (Drimmel et al., 2000; Smart et al., 1998).

By depicting a general picture of the vertical motions out to approximately 7 kpc from the Sun, *Gaia* DR2 have already made an important contribution to the understanding of the nature of the Galactic warp. However, numerous questions regarding the warp are still unanswered. For instance, it is not known whether the warp is a transient structure (as would result from being caused by an encounter), or whether it is a stable (or semi-stable) structure, as would be expected if it was the result of torques from a non-spherical halo. A more quantitative analysis can provide additional valuable informations, i.e. kinematic and/or spatial warp parameters statistically inferred from the data. Therefore, we plan to fit for the warp parameters using our *Gaia* DR2 samples, expanding the statistical approach adopted for TGAS OB stars (Chapter 6) according to the properties of the *Gaia* DR2 data. Future plans also include a more detailed exploration of the spiral arms structure observed in the upper main sequence *Gaia* DR2 sample, possibly investigating the impact of the spiral arms on the kinematics of the disc. Finally, we will prepare for further *Gaia* releases by developing new techniques for selecting stellar populations, based only on Gaia observables, without limiting ourselves to the stars with available 2MASS photometry.

APPENDIX A

Appendix: Absolute magnitude / intrinsic color calibrations

The study presented in Part I of this Thesis does not involve distance estimates, for the reasons discussed in Appendix B. The analysis (Chapter 4) is instead performed in the space of observables, namely Galactic longitude l and proper motion μ_b. Parallaxes are only used to split our sample in two main subsamples (i.e. a nearby and distant objects). While for the the TGAS(HIP2) catalogue we use *Gaia* DR1 trigonometric parallaxes, spectro-photometric parallaxes are used for the HIP2 sample. Indeed, due to the adopted parallax cut ($\varpi < 2$ mas), our sample mostly contains stars more distant than 500 pc, for which the large relative errors on the *Hipparcos* trigonometric parallaxes do not allow us to obtain reliable distance information. The present Appendix represents a digression from the main content of this Thesis, as it is focused on two main objectives: choosing the absolute magnitude-intrinsic color calibration (which is included in our model in Section 3.2) from those available in the literature, and also estimating the typical uncertainty on spectro-photometric parallaxes. As explained in the following, the data adopted here are used only in this Appendix, for achieving the two objectives reported above.

Numerous spectral class - luminosity calibrations for OB stars are available in the literature. In order to select an appropriate calibration, we evaluated those listed in Table A.1 using a set of OB stars located approximately at the same distance from the Sun, namely from the LMC. Since these stars can be assumed to be at nearly the same distance, there should be no trends in the distance modulus with respect to spectral class or intrinsic color. To test this for each calibration, we select 352 O-B0 stars (hereafter, the O sample) presented in Walborn et al. (2014), based on the VLT-FLAMES Tarantula Survey (VFTS, Evans et al., 2011) which performed a census of the hot luminous stars (Doran et al., 2013) in the 30 Doradus (the Tarantula nebula) star forming region, and 330 B0-B3 stars (hereafter, the B sample) in the two LMC clusters N11 and NGC

Table A.1: Absolute magnitude and intrinsic color calibrations.

Calibration	Spectral range[1]	References
Straizys (1981)	O5-B9	Straizys and Kuriliene, Straižys (1992)
Schmidt-Kaler (1982)	O3-B9	Schmidt-Kaler (1982)
Humphreys (1984)	O7-B3	Humphreys and McElroy (1984), Flower (1977)
Vacca (1996)	O3-B0.5	Vacca et al. (1996), Straižys (1992)
Loktin (2001)	O9-B8	Loktin and Beshenov (2001), Straižys (1992)
Martins (2005)	O3-O9.5	Martins et al. (2005), Martins and Plez (2006)
Wegner (2006)	O5-B9.5	Wegner (2006)

2004, selected from Hunter et al. (2008).

For each calibration the distance modulus $(m-M)_{cal} = m_V - M_{V,cal} - A_{V,cal}$ is computed for each star, where the extinction A_V is determined from the observed $(B-V)$ color excess, using a constant value of visual reddening R_V, taken from the literature. For the O sample in the 30 Doradus nebula, we used $R_V = 4.5 \pm 0.2$ estimated by De Marchi and Panagia (2014), while for the B sample in the clusters N11 and NGC 2004 we used the standard Galactic reddening ($R_V = 3.1$) in line with Hunter et al. (2008). Where possible, both absolute magnitude and intrinsic color are taken from the same author, for consistency. Otherwise we import the intrinsic color from another calibration that the author used or mentioned in their work. Finally, the trends with respect to spectral type and intrinsic color were evaluated by performing linear fits with respect to these parameters, as shown in Figures A.1 and A.2.

Based on their minimum dependance on the spectral type and intrinsic color, we selected the calibration of Martins (2005) for the O stars and Humphreys (1984) for the B stars. Given that the extinction in these star forming regions of the LMC is a subject of study, we repeated the same analysis with different values for the reddening (e. g. for the 30 Doradus nebula, $R_V = 3.5$ within the MEDUSA region and $R_V = 4.2$ within the R136 region, as suggested by Doran et al. (2013)). Although the distributions were shifted, the global trends were approximately preserved and the calibrations of Martins and Humphreys remained the preferred ones.

Since two calibrations are to be used for our Hipparcos OB sample, we checked their consistency using the stars in the LMC O sample, using the same value for the reddening (i.e. $R_V = 4.5$). (For the Humphreys calibration only those stars in the O7 to B0 range are used.) Figure A.3 shows the distribution of $(m-M)_{cal} - (m-M)_0$, where $(m-M)_0 = 18.50 \pm 0.10$ is the "canonical" value for distance modulus of the LMC (Freedman et al., 2001). We obtain a mean value of $< (m-M)_{O,Mt} >= 18.55 \pm 0.04$ and standard deviation $\sigma_{O,Mt} = 0.73 \pm 0.03$ using the Martins' calibration, while from the Humphreys' calibration we find $< (m-M)_{O,Hm} >= 18.52 \pm 0.04$ and $\sigma_{O,Hm} = 0.73 \pm 0.04$. According to the Kolmogorov-Smirnoff test, the two distributions are from the same parent distribution at the 95% confidence level. The consistency of the results suggests that, even if the calibrations were produced by different authors and were obtained using dif-

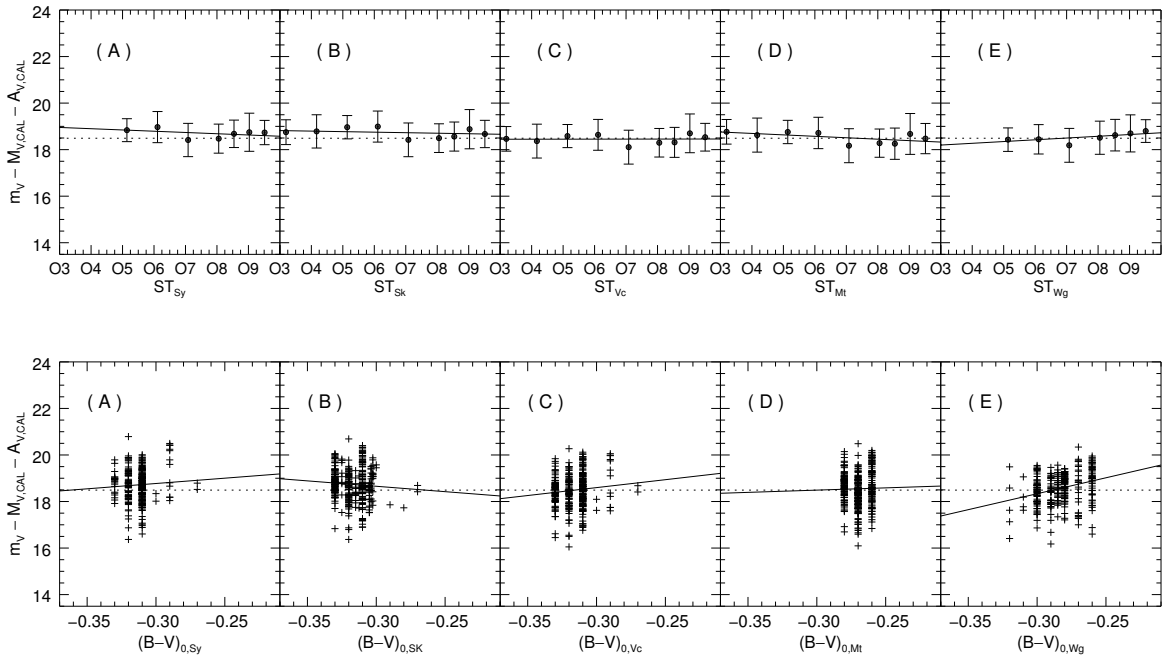

Figure A.1: Distance modulus in function of spectral type (top) and intrinsic color (bottom) for the O sample. From left to right: (A) Straizys and Kuriliene, (B) Schmidt-Kaler (1982), (C) Vacca et al. (1996), (D) Martins et al. (2005), (E) Wegner (2006). The solid line shows the linear fit to the data, while the dotted line represents the value found in literature (Freedman et al., 2001, see text).

ferent methods, they can be applied to a unique sample containing both O and B stars without introducing a discontinuity in the distance determinations. The $\sigma_{(m-M)}$ of these distributions also provides us with an empirical estimate of the overall uncertainty of the distance moduli of OB stars derived from the spectral types and these calibrations. The $\sigma_{(m-M)} = 0.73$ is comparable with the error model presented in Drimmel et al. (2000), which we adopted in this work.

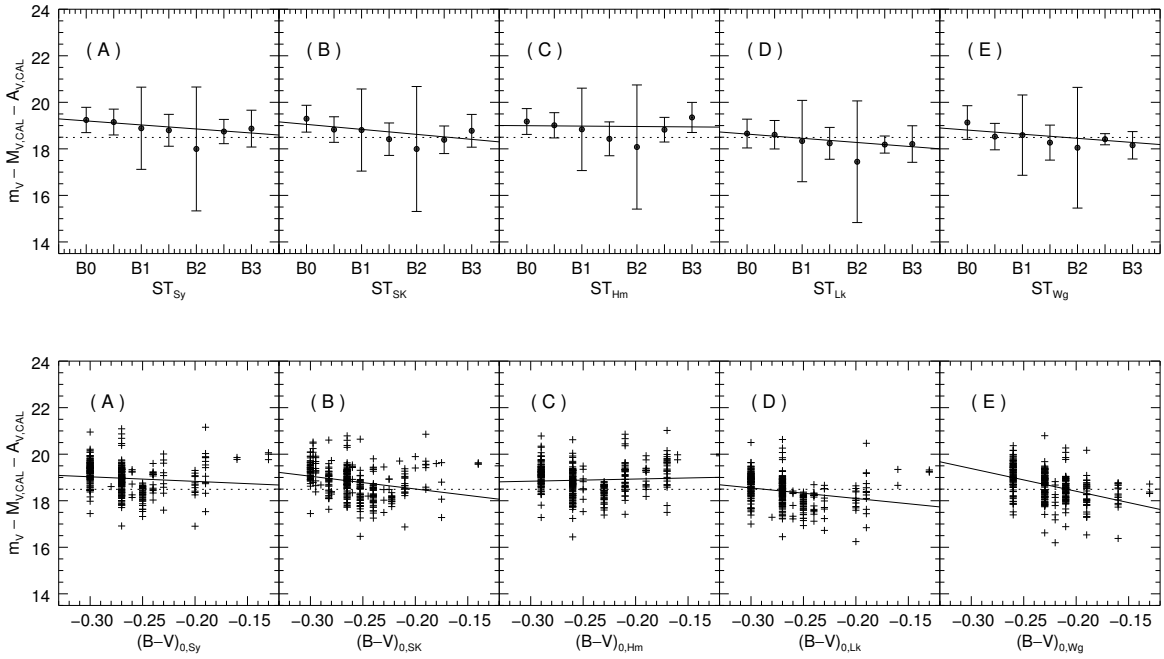

Figure A.2: Distance modulus in function of spectral type (top) and intrinsic color (bottom) for the B sample. From left to right: (A) Straizys and Kuriliene, (B) Schmidt-Kaler (1982), (C) Humphreys and McElroy (1984), (D) Loktin and Beshenov (2001), (E) Wegner (2006). The solid line shows the linear fit to the data, while the dotted line represents the value found in literature (Freedman et al., 2001, see text).

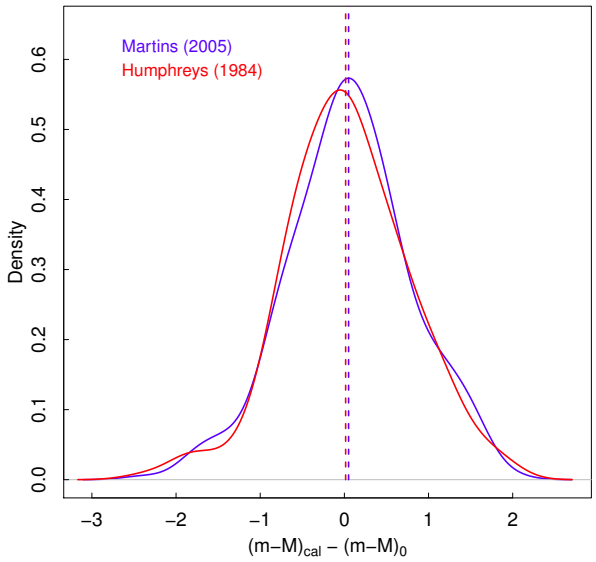

Figure A.3: Distance modulus distribution for the O sample according to Martins (2005) and Humphreys (1984) calibrations. The curves show the kernel density estimation for the two distributions. A gaussian kernel has been used for both. The dashed vertical lines represent the medians of the two distributions.

APPENDIX B

APPENDIX: STUDYING THE BIAS IN VERTICAL VELOCITY AS A CONSEQUENCE OF DISTANCE BIAS

The present Appendix represents a cautionary tale, that should be kept in mind when dealing with quantities derived from data observables. We specifically focus on the impact of distance errors on the mean vertical velocity $\overline{v}_z$. We here consider the mean vertical velocity as a function of Galactocentic radius R that one would derive from the HIP2 catalogue (see Chapter 2), comparing the data with what we expect from the no-warp and warp models (see Chapter 3). We present the results obtained from measured proper motions and spectro-photometric distances (see Appendix A), although a similar conclusion can be reached, in general, also for distances derived from trigonometric parallaxes with large relative errors.

In the no-warp case, the true mean vertical velocities are zero, while a warp model predicts that they increase with R outside the radius R_w at which the Galactic warp starts (see equation 3.6). Figure B.1 shows the mean vertical velocities, after removing the solar motion, for the data and for the no-warp/warp simulated catalogues. The simulated catalogues include the modelled errors, as described in Section 3.6. Taking into account both distance and proper motion errors, the observed trend is biased toward negative velocities with increasing distance. This bias is particularly evident with the no-warp model, where the true $\overline{v}_z(R) = 0$ (dashed line in Figure B.1), but similarly affects the warp model. One might be tempted to proceed to compare models to the data in this space of derived quantities, assuming the error models are correct, but this approach gives the most weight to the data at large distances, i.e. those with the highest errors and the most biased. Indeed, from Figure B.1 one might quickly conclude that the data was consistent with the no-warp model, based however on trends that are dominated by a bias in the derived quantities.

A better approach is to compare the data to the models in the space of the observations,

i.e. the mean proper motions as a function of position on the sky, thereby avoiding the biases introduced by the highly uncertain distances. That is, it is better to pose the question: which model best reproduces the observations? Our approach in Chapter 4 will make minimum use of the spectro-photometric distances and parallaxes to avoid the strong biases introduced when using distances with relatively large uncertainties to arrive at other derived quantities, as in the example above. Indeed, whether based on spectrophotometric data or parallaxes, distance is itself a derived quantity that can suffer from strong biases (Bailer-Jones, 2015).

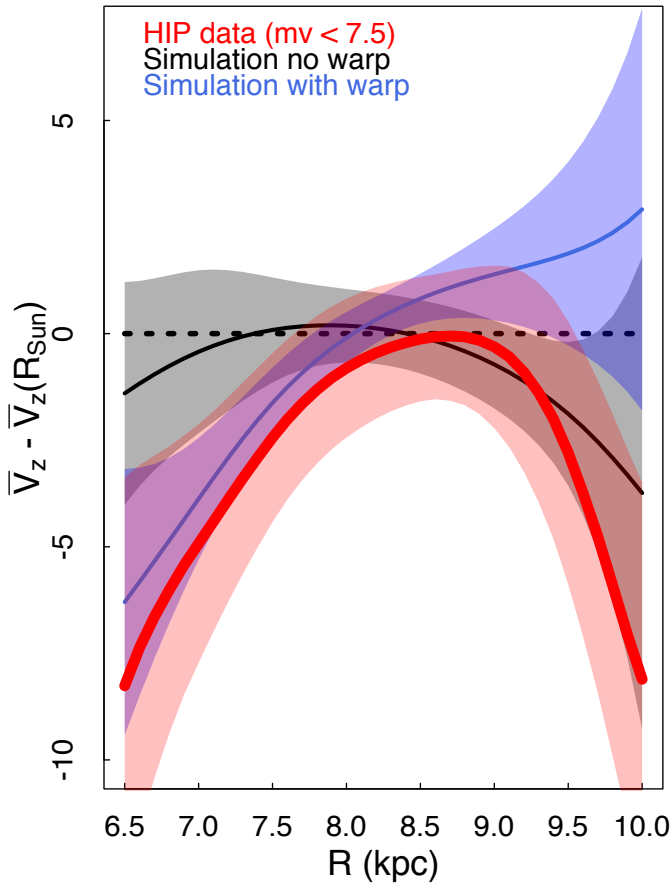

Figure B.1: Bivariate Nadaraya-Watson regression estimator of stellar vertical velocities as a function of Galactocentric radius, using a bandwidth of h = 0.5 kpc. The same regression bandwidth has been used for the data (red), the no-warp model (black) and warp model of Yusifov (2004) (blue). The 95 % bootstrap confidence band is shown for the data. For each of the two models, the non parametric regressions are performed for 20 simulated catalogues, obtaining the curves as the mean values and the shaded areas as the 95 % uncertainty. This Figure shows that the observational errors in the calculated distances cause the obtained vertical velocites to be biased toward negative values at large distances, as reproduced by the simulated catalogues (see the text for the details).

Acknowledgements

Firstly, I would like to express my sincere gratitude to Ronald Drimmel for the continuous support of my Ph.D study and related research, for his patience, motivation, and immense knowledge. I could not have imagined having a better guidance for my Ph.D study! Profound gratitude goes to Alessandro Spagna, for his valuable comments, encouragement and helpfulness. I also would like to thank Richard Smart, for his fundamental support and his British humor. Special mention also to Mario Lattanzi, for sharing his extensive knowledge in astronomy. Moreover, I want to thank Beatrice Bucciarelli, for her help with questions on astrometry, as well as her enthusiasm and friendship. I also would like to thank Rene Andrae, Coryn Bailer-Jones and Morgan Fouesneau for their fundamental help and support during my stay at the Max Planck Institute for Astronomy in Heidelberg.

Lastly, I would like to thank my family and friends for all their love and inspiration. Special mention to my beloved husband, Alberto, for his unconditional support and encouragement. I wish also to thank my baby, Lorenzo, for his sweetness and happiness. I want to thank my parents Vera e Maurizio, as well as my grandma Jose, for their enormous help, especially for their full-time baby sitting. Finally, I would like to thank Valerio, Clementina, Paolo, Lucia, Gabriele, Damiano, Sara, Madda, Franco and Maria, for their presence and encouragement. Last, but not least, many thanks to my friends Maria Cristina and Anastasia, for their unique support and friendship.

BIBLIOGRAPHY

H. Abedi, F. Figueras, L. Aguilar, C. Mateu, M. Romero-Gomez, M. Lopez-Corredoira, and F. Garzon Lopez.
On the characterization of the Galactic warp in the Gaia era.
In *EAS Publications Series*, volume 67 of *EAS Publications Series*, pages 237–240, July 2014.
doi: 10.1051/eas/1567042.

H. Abedi, F. Figueras, L. Aguilar, C. Mateu, M. Romero-Gómez, M. López-Corredoira, and F. Garzón.
Galactic warp kinematics: model vs. observations.
In A. J. Cenarro, F. Figueras, C. Hernández-Monteagudo, J. Trujillo Bueno, and L. Valdivielso, editors, *Highlights of Spanish Astrophysics VIII*, pages 423–428, May 2015.

E. Anderson and C. Francis.
XHIP: An extended hipparcos compilation.
Astronomy Letters, 38:331–346, May 2012.
doi: 10.1134/S1063773712050015.

R. Andrae, M. Fouesneau, O. Creevey, C. Ordenovic, N. Mary, A. Burlacu, L. Chaoul, A. Jean-Antoine-Piccolo, G. Kordopatis, A. Korn, Y. Lebreton, C. Panem, B. Pichon, F. Thévenin, G. Walmsley, and C. A. L. Bailer-Jones.
Gaia Data Release 2. First stellar parameters from Apsis.
Astron. Astrophys., 616:A8, August 2018.
doi: 10.1051/0004-6361/201732516.

T. Antoja, A. Helmi, M. Romero-Gomez, D. Katz, C. Babusiaux, R. Drimmel, D. W. Evans, F. Figueras, E. Poggio, C. Reyle, A. C. Robin, G. Seabroke, and C. Soubiran.
Wrinkles in the Gaia data unveil a dynamically young and perturbed Milky Way disk.
ArXiv e-prints, April 2018.

F. Arenou and X. Luri.
Distances and absolute magnitudes from trigonometric parallaxes.
In D. Egret and A. Heck, editors, *Harmonizing Cosmic Distance Scales in a Post-HIPPARCOS Era*, volume 167 of *Astronomical Society of the Pacific Conference Series*, pages 13–32, 1999.

F. Arenou, X. Luri, C. Babusiaux, C. Fabricius, A. Helmi, T. Muraveva, A. C. Robin, F. Spoto, A. Vallenari, T. Antoja, T. Cantat-Gaudin, C. Jordi, N. Leclerc, C. Reylé, M. Romero-Gómez, I.-C. Shih, S. Soria, C. Barache, D. Bossini, A. Bragaglia, M. A. Breddels, M. Fabrizio, S. Lambert, P. M. Marrese, D. Massari, A. Moitinho, N. Robichon, L. Ruiz-Dern, R. Sordo, J. Veljanoski, L. Eyer, G. Jasniewicz, E. Pancino, C. Soubiran, A. Spagna, P. Tanga, C. Turon, and C. Zurbach.
Gaia Data Release 2. Catalogue validation.
Astron. Astrophys., 616:A17, August 2018.
doi: 10.1051/0004-6361/201833234.

T. L. Astraatmadja and C. A. L. Bailer-Jones.
Estimating Distances from Parallaxes. II. Performance of Bayesian Distance Estimators on a Gaia-like Catalogue.
Astrophys. J., 832:137, December 2016.
doi: 10.3847/0004-637X/832/2/137.

E. Athanassoula.
Boxy/Peanut/X Bulges, Barlenses and the Thick Part of Galactic Bars: What Are They and How Did They Form?
In E. Laurikainen, R. Peletier, and D. Gadotti, editors, *Galactic Bulges*, volume 418 of *Astrophysics and Space Science Library*, page 391, 2016.
doi: 10.1007/978-3-319-19378-6_14.

C. Babusiaux and G. Gilmore.
The structure of the Galactic bar.
358:1309–1319, April 2005.
doi: 10.1111/j.1365-2966.2005.08828.x.

J. N. Bahcall and R. M. Soneira.
doi: 10.1086/190685.

J. N. Bahcall, S. Casertano, and K. U. Ratnatunga.
An analysis of the Yale Bright Star Catalog.
Astrophys. J., 320:515–526, September 1987.
doi: 10.1086/165569.

C. A. L. Bailer-Jones.
Estimating Distances from Parallaxes.
Publ. Astron. Soc. Pac., 127:994–1009, October 2015.
doi: 10.1086/683116.

C. A. L. Bailer-Jones, J. Rybizki, M. Fouesneau, G. Mantelet, and R. Andrae.

Estimating distances from parallaxes IV: Distances to 1.33 billion stars in Gaia Data Release 2.
ArXiv e-prints, April 2018.

Coryn A. L. Bailer-Jones.
Practical Bayesian Inference: A Primer for Physical Scientists.
Cambridge University Press, 2017.
doi: 10.1017/9781108123891.

J. Bailin.
Evidence for Coupling between the Sagittarius Dwarf Galaxy and the Milky Way Warp.
Astrophys. J. Lett., 583:L79–L82, February 2003.
doi: 10.1086/368160.

J. Bailin and M. Steinmetz.
Coupling between Satellite Dwarfs and the Milky Way Warp.
In F. Prada, D. Martinez Delgado, and T. J. Mahoney, editors, *Satellites and Tidal Streams*, volume 327 of *Astronomical Society of the Pacific Conference Series*, page 225, December 2004.

E. Battaner, E. Florido, and M. L. Sanchez-Saavedra.
Intergalactic magnetic field and galactic WARPS.
Astron. Astrophys., 236:1–8, September 1990.

V. Belokurov, N. W. Evans, M. J. Irwin, D. Lynden-Bell, B. Yanny, S. Vidrih, G. Gilmore, G. Seabroke, D. B. Zucker, M. I. Wilkinson, P. C. Hewett, D. M. Bramich, M. Fellhauer, H. J. Newberg, R. F. G. Wyse, T. C. Beers, E. F. Bell, J. C. Barentine, J. Brinkmann, N. Cole, K. Pan, and D. G. York.
An Orphan in the “Field of Streams”.
Astrophys. J., 658:337–344, March 2007.
doi: 10.1086/511302.

T. Bensby, S. Feltzing, and I. Lundström.
Elemental abundance trends in the Galactic thin and thick disks as traced by nearby F and G dwarf stars.
Astron. Astrophys., 410:527–551, November 2003.
doi: 10.1051/0004-6361:20031213.

J. Binney.
WARPS.
30:51–74, 1992.
doi: 10.1146/annurev.aa.30.090192.000411.

J. Binney, O. E. Gerhard, A. A. Stark, J. Bally, and K. I. Uchida.
Understanding the kinematics of Galactic centre gas.
252:210–218, September 1991.
doi: 10.1093/mnras/252.2.210.

J. Binney, O. Gerhard, and D. Spergel.
The photometric structure of the inner Galaxy.
288:365–374, June 1997.
doi: 10.1093/mnras/288.2.365.

J. Binney, I.-G. Jiang, and S. Dutta.
The Persistence of WARPS in Spiral Galaxies with Massive Haloes.
297:1237–1244, July 1998.
doi: 10.1046/j.1365-8711.1998.01595.x.

N. Bissantz and O. Gerhard.
Spiral arms, bar shape and bulge microlensing in the Milky Way.
330:591–608, March 2002.
doi: 10.1046/j.1365-8711.2002.05116.x.

J. Bland-Hawthorn and O. Gerhard.
The Galaxy in Context: Structural, Kinematic, and Integrated Properties.
54:529–596, September 2016.
doi: 10.1146/annurev-astro-081915-023441.

J. Bland-Hawthorn and P. R. Maloney.
Hα Distance Constraints for High Velocity Clouds in the Galactic Halo.
In J. S. Mulchaey and J. T. Stocke, editors, *Extragalactic Gas at Low Redshift*, volume 254 of *Astronomical Society of the Pacific Conference Series*, page 267, 2002.

V. V. Bobylev.
Parameters of the local warp of the stellar-gaseous galactic disk from the kinematics of Tycho-2 nearby red giant clump stars.
Astronomy Letters, 36:634–644, September 2010.
doi: 10.1134/S1063773710090021.

V. V. Bobylev.
Cepheid kinematics and the Galactic warp.
Astronomy Letters, 39:819–825, December 2013.
doi: 10.1134/S1063773713120025.

V. V. Bobylev.

Residual HCRF rotation relative to the inertial coordinate system.
Astronomy Letters, 41:156–165, March 2015.
doi: 10.1134/S1063773715040039.

A. Bonaca, C. Conroy, A. Wetzel, P. F. Hopkins, and D. Kereš.
Gaia Reveals a Metal-rich, in situ Component of the Local Stellar Halo.
Astrophys. J., 845:101, August 2017.
doi: 10.3847/1538-4357/aa7d0c.

A. Bosma.
Warped and Flaring HI Disks.
In S. Casertano, P. D. Sackett, and F. H. Briggs, editors, *Warped Disks and Inclined Rings around Galaxies*, page 181, 1991.

A. Bressan, P. Marigo, L. Girardi, B. Salasnich, C. Dal Cero, S. Rubele, and A. Nanni.
PARSEC: stellar tracks and isochrones with the PAdova and TRieste Stellar Evolution Code.
427:127–145, November 2012.
doi: 10.1111/j.1365-2966.2012.21948.x.

F. H. Briggs.
Rules of behavior for galactic WARPS.
Astrophys. J., 352:15–29, March 1990.
doi: 10.1086/168512.

A. G. A. Brown, E. J. de Geus, and P. T. de Zeeuw.
The Orion OB1 association. 1: Stellar content.
Astron. Astrophys., 289:101–120, September 1994.

A. G. A. Brown, F. Arenou, F. van Leeuwen, L. Lindegren, and X. Luri.
Considerations in Making Full Use of the HIPPARCOS Catalogue.
In R. M. Bonnet, E. Høg, P. L. Bernacca, L. Emiliani, A. Blaauw, C. Turon, J. Kovalevsky, L. Lindegren, H. Hassan, M. Bouffard, B. Strim, D. Heger, M. A. C. Perryman, and L. Woltjer, editors, *Hipparcos - Venice '97*, volume 402 of *ESA Special Publication*, pages 63–68, August 1997.

B. F. Burke.
Systematic distortion of the outer regions of the galaxy.
Astron. J., 62:90, May 1957.
doi: 10.1086/107463.

W. B. Burton.
The structure of our Galaxy derived from observations of neutral hydrogen, pages 295–358.
1988.

J. A. Cardelli, G. C. Clayton, and J. S. Mathis.
The relationship between infrared, optical, and ultraviolet extinction.
Astrophys. J., 345:245–256, October 1989.
doi: 10.1086/167900.

D. Carollo, T. C. Beers, Y. S. Lee, M. Chiba, J. E. Norris, R. Wilhelm, T. Sivarani, B. Marsteller, J. A. Munn, C. A. L. Bailer-Jones, P. R. Fiorentin, and D. G. York.
Two stellar components in the halo of the Milky Way.
Nature, 450:1020–1025, December 2007.
doi: 10.1038/nature06460.

B. Chen, C. Stoughton, J. A. Smith, A. Uomoto, J. R. Pier, B. Yanny, Ž. Ivezić, D. G. York, J. E. Anderson, J. Annis, J. Brinkmann, I. Csabai, M. Fukugita, R. Hindsley, R. Lupton, J. A. Munn, and SDSS Collaboration.
Stellar Population Studies with the SDSS. I. The Vertical Distribution of Stars in the Milky Way.
Astrophys. J., 553:184–197, May 2001.
doi: 10.1086/320647.

Y. Chen, L. Girardi, A. Bressan, P. Marigo, M. Barbieri, and X. Kong.
Improving PARSEC models for very low mass stars.
444:2525–2543, November 2014.
doi: 10.1093/mnras/stu1605.

Y. Chen, A. Bressan, L. Girardi, P. Marigo, X. Kong, and A. Lanza.
PARSEC evolutionary tracks of massive stars up to 350 $M_{\odot}$ at metallicities $0.0001 \leq Z \leq 0.04$.
452:1068–1080, September 2015.
doi: 10.1093/mnras/stv1281.

F. Comeron, J. Torra, and A. E. Gomez.
The characteristics and origin of the Gould's Belt.
Astrophys. Space Science, 187:187–195, January 1992.
doi: 10.1007/BF00643388.

A. P. Cooper, O. H. Parry, B. Lowing, S. Cole, and C. Frenk.
Formation of in situ stellar haloes in Milky Way-mass galaxies.
454:3185–3199, December 2015.
doi: 10.1093/mnras/stv2057.

M. Cropper, D. Katz, P. Sartoretti, T. Prusti, J. H. J. de Bruijne, F. Chassat, P. Charvet, J. Boyadjian, M. Perryman, G. Sarri, P. Gare, M. Erdmann, U. Munari, T. Zwitter, M. Wilkinson, F. Arenou, A. Vallenari, A. Gómez, P. Panuzzo, G. Seabroke, C. Allende Prieto, K. Benson,

O. Marchal, H. Huckle, M. Smith, C. Dolding, K. Janßen, Y. Viala, R. Blomme, S. Baker, S. Boudreault, F. Crifo, C. Soubiran, Y. Frémat, G. Jasniewicz, A. Guerrier, L. P. Guy, C. Turon, A. Jean-Antoine-Piccolo, F. Thévenin, M. David, E. Gosset, and Y. Damerdji.
Gaia Data Release 2. Gaia Radial Velocity Spectrometer.
Astron. Astrophys., 616:A5, August 2018.
doi: 10.1051/0004-6361/201832763.

G. De Marchi and N. Panagia.
The extinction law inside the 30 Doradus nebula.
445:93–106, November 2014.
doi: 10.1093/mnras/stu1694.

P. T. de Zeeuw, R. Hoogerwerf, J. H. J. de Bruijne, A. G. A. Brown, and A. Blaauw.
A HIPPARCOS Census of the Nearby OB Associations.
Astron. J., 117:354–399, January 1999.
doi: 10.1086/300682.

A. J. Deason, V. Belokurov, and N. W. Evans.
The Milky Way stellar halo out to 40 kpc: squashed, broken but smooth.
416:2903–2915, October 2011.
doi: 10.1111/j.1365-2966.2011.19237.x.

V. P. Debattista and J. A. Sellwood.
Warped Galaxies from Misaligned Angular Momenta.
Astrophys. J. Lett., 513:L107–L110, March 1999.
doi: 10.1086/311913.

W. Dehnen.
The Distribution of Nearby Stars in Velocity Space Inferred from HIPPARCOS Data.
Astron. J., 115:2384–2396, June 1998.
doi: 10.1086/300364.

W. Dehnen and J. J. Binney.
Local stellar kinematics from HIPPARCOS data.
298:387–394, August 1998.
doi: 10.1046/j.1365-8711.1998.01600.x.

S. Derriere and A. C. Robin.
Near-infrared Surveys and the Shape of the Galactic Disc.
In R. Clowes, A. Adamson, and G. Bromage, editors, *The New Era of Wide Field Astronomy*, volume 232 of *Astronomical Society of the Pacific Conference Series*, page 229, 2001.

P. Di Matteo, M. Haywood, A. Gómez, L. van Damme, F. Combes, A. Hallé, B. Semelin, M. D. Lehnert, and D. Katz.
Mapping a stellar disk into a boxy bulge: The outside-in part of the Milky Way bulge formation.
Astron. Astrophys., 567:A122, July 2014.
doi: 10.1051/0004-6361/201322958.

E. I. Doran, P. A. Crowther, A. de Koter, C. J. Evans, C. McEvoy, N. R. Walborn, N. Bastian, J. M. Bestenlehner, G. Gräfener, A. Herrero, K. Köhler, J. Maíz Apellániz, F. Najarro, J. Puls, H. Sana, F. R. N. Schneider, W. D. Taylor, J. T. van Loon, and J. S. Vink.
The VLT-FLAMES Tarantula Survey. XI. A census of the hot luminous stars and their feedback in 30 Doradus.
Astron. Astrophys., 558:A134, October 2013.
doi: 10.1051/0004-6361/201321824.

R. Drimmel and D. N. Spergel.
Three-dimensional Structure of the Milky Way Disk: The Distribution of Stars and Dust beyond 0.35 R_{solar}.
Astrophys. J., 556:181–202, July 2001.
doi: 10.1086/321556.

R. Drimmel, R. L. Smart, and M. G. Lattanzi.
The Galactic warp in OB stars from Hipparcos.
Astron. Astrophys., 354:67–76, February 2000.

R. Drimmel, A. Cabrera-Lavers, and M. López-Corredoira.
A three-dimensional Galactic extinction model.
Astron. Astrophys., 409:205–215, October 2003.
doi: 10.1051/0004-6361:20031070.

S. Duffau, R. Zinn, A. K. Vivas, G. Carraro, R. A. Méndez, R. Winnick, and C. Gallart.
Spectroscopy of QUEST RR Lyrae Variables: The New Virgo Stellar Stream.
Astrophys. J. Lett., 636:L97–L100, January 2006.
doi: 10.1086/500130.

E. Dwek, R. G. Arendt, M. G. Hauser, T. Kelsall, C. M. Lisse, S. H. Moseley, R. F. Silverberg, T. J. Sodroski, and J. L. Weiland.
Morphology, near-infrared luminosity, and mass of the Galactic bulge from COBE DIRBE observations.
Astrophys. J., 445:716–730, June 1995.
doi: 10.1086/175734.

O. J. Eggen, D. Lynden-Bell, and A. R. Sandage.

Evidence from the motions of old stars that the Galaxy collapsed.
Astrophys. J., 136:748, November 1962.
doi: 10.1086/147433.

P. Englmaier and O. Gerhard.
Gas dynamics and large-scale morphology of the Milky Way galaxy.
304:512–534, April 1999.
doi: 10.1046/j.1365-8711.1999.02280.x.

ESA, editor.
The HIPPARCOS and TYCHO catalogues. Astrometric and photometric star catalogues derived from the ESA HIPPARCOS Space Astrometry Mission, volume 1200 of *ESA Special Publication*, 1997.

C. Evans, W. Taylor, H. Sana, V. Hénault-Brunet, T. Bagnoli, N. Bastian, J. Bestenlehner, A. Bonanos, E. Bressert, I. Brott, M. Campbell, M. Cantiello, G. Carraro, S. Clark, E. Costa, P. Crowther, A. de Koter, S. E. de Mink, E. Doran, P. Dufton, P. Dunstall, M. Garcia, M. Gieles, G. Gräfener, A. Herrero, I. Howarth, R. Izzard, K. Köhler, N. Langer, D. Lennon, J. Maíz Apellániz, N. Markova, P. Najarro, J. Puls, O. Ramirez, C. Sabín-Sanjulián, S. Simón-Díaz, S. Smartt, V. Stroud, J. van Loon, J. S. Vink, and N. Walborn.
The VLT FLAMES Tarantula Survey.
The Messenger, 145:33–38, September 2011.

D. W. Evans, M. Riello, F. De Angeli, J. M. Carrasco, P. Montegriffo, C. Fabricius, C. Jordi, L. Palaversa, C. Diener, G. Busso, C. Cacciari, F. van Leeuwen, P. W. Burgess, M. Davidson, D. L. Harrison, S. T. Hodgkin, E. Pancino, P. J. Richards, G. Altavilla, L. Balaguer-Núñez, M. A. Barstow, M. Bellazzini, A. G. A. Brown, M. Castellani, G. Cocozza, F. De Luise, A. Delgado, C. Ducourant, S. Galleti, G. Gilmore, G. Giuffrida, B. Holl, A. Kewley, S. E. Koposov, S. Marinoni, P. M. Marrese, P. J. Osborne, A. Piersimoni, J. Portell, L. Pulone, S. Ragaini, N. Sanna, D. Terrett, N. A. Walton, T. Wevers, and Ł. Wyrzykowski.
Gaia Data Release 2. Photometric content and validation.
Astron. Astrophys., 616:A4, August 2018.
doi: 10.1051/0004-6361/201832756.

E. D. Feigelson and G. J. Babu.
Modern Statistical Methods for Astronomy.
July 2012.

P. J. Flower.
Transformations from Theoretical H-R Diagrams to C-M Diagrams.
Astron. Astrophys., 54:31, January 1977.

W. L. Freedman, B. F. Madore, B. K. Gibson, L. Ferrarese, D. D. Kelson, S. Sakai, J. R. Mould, R. C. Kennicutt, Jr., H. C. Ford, J. A. Graham, J. P. Huchra, S. M. G. Hughes, G. D. Illingworth, L. M. Macri, and P. B. Stetson.
Final Results from the Hubble Space Telescope Key Project to Measure the Hubble Constant.
Astrophys. J., 553:47–72, May 2001.
doi: 10.1086/320638.

K. Freeman and J. Bland-Hawthorn.
The New Galaxy: Signatures of Its Formation.
40:487–537, 2002.
doi: 10.1146/annurev.astro.40.060401.093840.

H. T. Freudenreich, G. B. Berriman, E. Dwek, M. G. Hauser, T. Kelsall, S. H. Moseley, R. F. Silverberg, T. J. Sodroski, G. N. Toller, and J. L. Weiland.
DIRBE evidence for a warp in the interstellar dust layer and stellar disk of the galaxy.
Astrophys. J. Lett., 429:L69–L72, July 1994.
doi: 10.1086/187415.

D. Friedli, W. Benz, and R. Kennicutt.
On the influence of bars and star formation on galactic abundance gradients.
Astrophys. J. Lett., 430:L105–L108, August 1994.
doi: 10.1086/187449.

R. Fux.
3D self-consistent N-body barred models of the Milky Way. II. Gas dynamics.
Astron. Astrophys., 345:787–812, May 1999.

Gaia Collaboration, A. G. A. Brown, A. Vallenari, T. Prusti, J. H. J. de Bruijne, F. Mignard, R. Drimmel, C. Babusiaux, C. A. L. Bailer-Jones, U. Bastian, and et al.
Gaia Data Release 1. Summary of the astrometric, photometric, and survey properties.
Astron. Astrophys., 595:A2, November 2016.
doi: 10.1051/0004-6361/201629512.

Gaia Collaboration, A. G. A. Brown, A. Vallenari, T. Prusti, J. H. J. de Bruijne, C. Babusiaux, C. A. L. Bailer-Jones, M. Biermann, D. W. Evans, L. Eyer, and et al.
Gaia Data Release 2. Summary of the contents and survey properties.
Astron. Astrophys., 616:A1, August 2018a.
doi: 10.1051/0004-6361/201833051.

Gaia Collaboration, D. Katz, T. Antoja, M. Romero-Gómez, R. Drimmel, C. Reylé, G. M. Seabroke, C. Soubiran, C. Babusiaux, P. Di Matteo, and et al.
Gaia Data Release 2. Mapping the Milky Way disc kinematics.

Astron. Astrophys., 616:A11, August 2018b.
doi: 10.1051/0004-6361/201832865.

Andrew Gelman, Andrew Gelman, Christian Robert, Nicolas Chopin, and Judith" Rousseau.
Bayesian data analysis.
pages 1360–1383, 1995.
doi: 10.1.1.217.2021.

Y. M. Georgelin and Y. P. Georgelin.
The spiral structure of our Galaxy determined from H II regions.
Astron. Astrophys., 49:57–79, May 1976.

A. M. Ghez, S. Salim, N. N. Weinberg, J. R. Lu, T. Do, J. K. Dunn, K. Matthews, M. R. Morris, S. Yelda, E. E. Becklin, T. Kremenek, M. Milosavljevic, and J. Naiman.
Measuring Distance and Properties of the Milky Way's Central Supermassive Black Hole with Stellar Orbits.
Astrophys. J., 689:1044–1062, December 2008.
doi: 10.1086/592738.

S. Gillessen, F. Eisenhauer, T. K. Fritz, H. Bartko, K. Dodds-Eden, O. Pfuhl, T. Ott, and R. Genzel.
The Orbit of the Star S2 Around SGR A* from Very Large Telescope and Keck Data.
Astrophys. J. Lett., 707:L114–L117, December 2009a.
doi: 10.1088/0004-637X/707/2/L114.

S. Gillessen, F. Eisenhauer, S. Trippe, T. Alexander, R. Genzel, F. Martins, and T. Ott.
Monitoring Stellar Orbits Around the Massive Black Hole in the Galactic Center.
Astrophys. J., 692:1075–1109, February 2009b.
doi: 10.1088/0004-637X/692/2/1075.

G. Gilmore and N. Reid.
New light on faint stars. III - Galactic structure towards the South Pole and the Galactic thick disc.
202:1025–1047, March 1983.
doi: 10.1093/mnras/202.4.1025.

G. Gilmore, R. F. G. Wyse, and K. Kuijken.
Kinematics, chemistry, and structure of the Galaxy.
27:555–627, 1989.
doi: 10.1146/annurev.aa.27.090189.003011.

G. Gilmore, R. F. G. Wyse, and J. B. Jones.
A determination of the thick disk chemical abundance distribution: Implications for galaxy evolution.

Astron. J., 109:1095–1111, March 1995.
doi: 10.1086/117344.

F. A. Gómez, I. Minchev, B. W. O'Shea, T. C. Beers, J. S. Bullock, and C. W. Purcell.
Vertical density waves in the Milky Way disc induced by the Sagittarius dwarf galaxy.
429:159–164, February 2013.
doi: 10.1093/mnras/sts327.

C. J. Grillmair and J. L. Carlin.
Stellar Streams and Clouds in the Galactic Halo.
In H. J. Newberg and J. L. Carlin, editors, *Tidal Streams in the Local Group and Beyond*, volume 420 of *Astrophysics and Space Science Library*, page 87, 2016.
doi: 10.1007/978-3-319-19336-6_4.

A. Guijarro, R. F. Peletier, E. Battaner, J. Jiménez-Vicente, R. de Grijs, and E. Florido.
Near-infrared and optical observations of galactic warps: a common, unexplained feature of most discs.
Astron. Astrophys., 519:A53, September 2010.
doi: 10.1051/0004-6361/201014506.

M. R. Hayden, J. Bovy, J. A. Holtzman, D. L. Nidever, J. C. Bird, D. H. Weinberg, B. H. Andrews, S. R. Majewski, C. Allende Prieto, F. Anders, T. C. Beers, D. Bizyaev, C. Chiappini, K. Cunha, P. Frinchaboy, D. A. García-Herńandez, A. E. García Pérez, L. Girardi, P. Harding, F. R. Hearty, J. A. Johnson, S. Mészáros, I. Minchev, R. O'Connell, K. Pan, A. C. Robin, R. P. Schiavon, D. P. Schneider, M. Schultheis, M. Shetrone, M. Skrutskie, M. Steinmetz, V. Smith, J. C. Wilson, O. Zamora, and G. Zasowski.
Chemical Cartography with APOGEE: Metallicity Distribution Functions and the Chemical Structure of the Milky Way Disk.
Astrophys. J., 808:132, August 2015.
doi: 10.1088/0004-637X/808/2/132.

M. Haywood, P. Di Matteo, M. D. Lehnert, D. Katz, and A. Gómez.
The age structure of stellar populations in the solar vicinity. Clues of a two-phase formation history of the Milky Way disk.
Astron. Astrophys., 560:A109, December 2013.
doi: 10.1051/0004-6361/201321397.

A. Helmi.
The stellar halo of the Galaxy.
15:145–188, June 2008.
doi: 10.1007/s00159-008-0009-6.

A. Helmi and S. D. M. White.
Building up the stellar halo of the Galaxy.
307:495–517, August 1999.
doi: 10.1046/j.1365-8711.1999.02616.x.

E. Høg, C. Fabricius, V. V. Makarov, S. Urban, T. Corbin, G. Wycoff, U. Bastian, P. Schwekendiek, and A. Wicenec.
The Tycho-2 catalogue of the 2.5 million brightest stars.
Astron. Astrophys., 355:L27–L30, March 2000.

N. Houk.
VizieR Online Data Catalog: Michigan Catalogue of HD stars, Vol.2 (Houk, 1978).
VizieR Online Data Catalog, 3051, November 1993.

N. Houk.
VizieR Online Data Catalog: Michigan Catalogue of HD stars, Vol.3 (Houk, 1982).
VizieR Online Data Catalog, 3080, November 1994.

N. Houk and A. P. Cowley.
VizieR Online Data Catalog: Michigan catalogue for the HD stars, vol. 1 (Houk+, 1975).
VizieR Online Data Catalog, 3031, November 1994.

N. Houk and M. Smith-Moore.
VizieR Online Data Catalog: Michigan Catalogue of HD stars, Vol.4 (Houk+, 1988).
VizieR Online Data Catalog, 3133, November 1994.

N. Houk and C. Swift.
VizieR Online Data Catalog: Michigan Catalogue of HD stars, Vol.5 (Houk+, 1999).
VizieR Online Data Catalog, 3214, March 2000.

R. M. Humphreys and D. B. McElroy.
The initial mass function for massive stars in the Galaxy and the Magellanic Clouds.
Astrophys. J., 284:565–577, September 1984.
doi: 10.1086/162439.

C. Hunter and A. Toomre.
Dynamics of the Bending of the Galaxy.
Astrophys. J., 155:747, March 1969.
doi: 10.1086/149908.

I. Hunter, D. J. Lennon, P. L. Dufton, C. Trundle, S. Simón-Díaz, S. J. Smartt, R. S. I. Ryans, and C. J. Evans.

The VLT-FLAMES survey of massive stars: atmospheric parameters and rotational velocity distributions for B-type stars in the Magellanic Clouds.
Astron.Astrophys., 479:541–555, February 2008.
doi: 10.1051/0004-6361:20078511.

R. Ibata, G. F. Lewis, M. Irwin, E. Totten, and T. Quinn.
Great Circle Tidal Streams: Evidence for a Nearly Spherical Massive Dark Halo around the Milky Way.
Astrophys. J., 551:294–311, April 2001.
doi: 10.1086/320060.

R. A. Ibata and A. O. Razoumov.
Archer of the Galactic disk? The effect on the outer HI disk of the Milky Way of collisional encounters with the Sagittarius dwarf galaxy.
Astron. Astrophys., 336:130–136, August 1998.

R. A. Ibata, G. Gilmore, and M. J. Irwin.
A dwarf satellite galaxy in Sagittarius.
Nature, 370:194–196, July 1994.
doi: 10.1038/370194a0.

P. Jofré and A. Weiss.
The age of the Milky Way halo stars from the Sloan Digital Sky Survey.
Astron. Astrophys., 533:A59, September 2011.
doi: 10.1051/0004-6361/201117131.

M. Jurić, Ž. Ivezić, A. Brooks, R. H. Lupton, D. Schlegel, D. Finkbeiner, N. Padmanabhan, N. Bond, B. Sesar, C. M. Rockosi, G. R. Knapp, J. E. Gunn, T. Sumi, D. P. Schneider, J. C. Barentine, H. J. Brewington, J. Brinkmann, M. Fukugita, M. Harvanek, S. J. Kleinman, J. Krzesinski, D. Long, E. H. Neilsen, Jr., A. Nitta, S. A. Snedden, and D. G. York.
The Milky Way Tomography with SDSS. I. Stellar Number Density Distribution.
Astrophys. J., 673:864–914, February 2008.
doi: 10.1086/523619.

F. D. Kahn and L. Woltjer.
Intergalactic Matter and the Galaxy.
Astrophys. J., 130:705, November 1959.
doi: 10.1086/146762.

P. M. W. Kalberla, L. Dedes, J. Kerp, and U. Haud.
Dark matter in the Milky Way. II. The HI gas distribution as a tracer of the gravitational potential.

Astron. Astrophys., 469:511–527, July 2007.
doi: 10.1051/0004-6361:20066362.

D. Katz, P. Sartoretti, M. Cropper, P. Panuzzo, G. M. Seabroke, Y. Viala, K. Benson, R. Blomme, G. Jasniewicz, A. Jean-Antoine, H. Huckle, M. Smith, S. Baker, F. Crifo, Y. Damerdji, M. David, C. Dolding, Y. Frémat, E. Gosset, A. Guerrier, L. P. Guy, R. Haigron, K. Janßen, O. Marchal, G. Plum, C. Soubiran, F. Thévenin, M. Ajaj, C. Allende Prieto, C. Babusiaux, S. Boudreault, L. Chemin, C. Delle Luche, C. Fabre, A. Gueguen, N. C. Hambly, Y. Lasne, F. Meynadier, F. Pailler, C. Panem, F. Royer, G. Tauran, C. Zurbach, T. Zwitter, F. Arenou, D. Bossini, A. Gomez, V. Lemaitre, N. Leclerc, T. Morel, U. Munari, C. Turon, A. Vallenari, and M. Žerjal.
Gaia Data Release 2: Properties and validation of the radial velocities.
ArXiv e-prints, April 2018.

D. Kawata, J. Baba, I. Ciucă, M. Cropper, R. J. J. Grand, J. A. S. Hunt, and G. Seabroke.
Radial Distribution of Stellar Motions in Gaia DR2.
June 2018.
doi: 10.1093/mnrasl/sly107.

F. J. Kerr.
A Magellanic effect on the galaxy.
Astron. J., 62:93–93, May 1957.
doi: 10.1086/107466.

C. S. Kochanek.
The Mass of the Milky Way.
Astrophys. J., 457:228, January 1996.
doi: 10.1086/176724.

J. Kormendy, N. Drory, R. Bender, and M. E. Cornell.
Bulgeless Giant Galaxies Challenge Our Picture of Galaxy Formation by Hierarchical Clustering.
Astrophys. J., 723:54–80, November 2010.
doi: 10.1088/0004-637X/723/1/54.

P. Kroupa.
On the variation of the initial mass function.
322:231–246, April 2001.
doi: 10.1046/j.1365-8711.2001.04022.x.

P. Kroupa.
The Initial Mass Function of Stars: Evidence for Uniformity in Variable Systems.
295:82–91, January 2002.

doi: 10.1126/science.1067524.

K. Kuijken and I. Garcia-Ruiz.
Galactic Disk Warps.
In J. G. Funes and E. M. Corsini, editors, *Galaxy Disks and Disk Galaxies*, volume 230 of *Astronomical Society of the Pacific Conference Series*, pages 401–408, 2001.

C. F. P. Laporte, F. A. Gómez, G. Besla, K. V. Johnston, and N. Garavito-Camargo.
Response of the Milky Way's disc to the Large Magellanic Cloud in a first infall scenario.
ArXiv e-prints, August 2016.

C. F. P. Laporte, F. A. Gómez, G. Besla, K. V. Johnston, and N. Garavito-Camargo.
Response of the Milky Way's disc to the Large Magellanic Cloud in a first infall scenario.
473:1218–1230, January 2018.
doi: 10.1093/mnras/stx2146.

E. S. Levine, L. Blitz, and C. Heiles.
The Vertical Structure of the Outer Milky Way H I Disk.
Astrophys. J., 643:881–896, June 2006.
doi: 10.1086/503091.

C. C. Lin and F. H. Shu.
On the Spiral Structure of Disk Galaxies.
Astrophys. J., 140:646, August 1964.
doi: 10.1086/147955.

P. O. Lindblad.
The development of spiral structure in a galaxy approached by numerical computations.
Stockholms Observatoriums Annaler, 21, 1960.

L. Lindegren.
The Tycho-Gaia Astrometric Solution.
In A. Recio-Blanco, P. de Laverny, A. G. A. Brown, and T. Prusti, editors, *IAU Symposium*, volume 330 of *IAU Symposium*, pages 41–48, April 2018.
doi: 10.1017/S1743921317005919.

L. Lindegren and J. Kovalevsky.
Linking the HIPPARCOS Catalogue to the extragalactic reference system.
Astron. Astrophys., 304:189, December 1995.

L. Lindegren, J. Hernández, A. Bombrun, S. Klioner, U. Bastian, M. Ramos-Lerate, A. de Torres, H. Steidelmüller, C. Stephenson, D. Hobbs, U. Lammers, M. Biermann, R. Geyer, T. Hilger,

D. Michalik, U. Stampa, P. J. McMillan, J. Castañeda, M. Clotet, G. Comoretto, M. Davidson, C. Fabricius, G. Gracia, N. C. Hambly, A. Hutton, A. Mora, J. Portell, F. van Leeuwen, U. Abbas, A. Abreu, M. Altmann, A. Andrei, E. Anglada, L. Balaguer-Núñez, C. Barache, U. Becciani, S. Bertone, L. Bianchi, S. Bouquillon, G. Bourda, T. Brüsemeister, B. Bucciarelli, D. Busonero, R. Buzzi, R. Cancelliere, T. Carlucci, P. Charlot, N. Cheek, M. Crosta, C. Crowley, J. de Bruijne, F. de Felice, R. Drimmel, P. Esquej, A. Fienga, E. Fraile, M. Gai, N. Garralda, J. J. González-Vidal, R. Guerra, M. Hauser, W. Hofmann, B. Holl, S. Jordan, M. G. Lattanzi, H. Lenhardt, S. Liao, E. Licata, T. Lister, W. Löffler, J. Marchant, J.-M. Martin-Fleitas, R. Messineo, F. Mignard, R. Morbidelli, E. Poggio, A. Riva, N. Rowell, E. Salguero, M. Sarasso, E. Sciacca, H. Siddiqui, R. L. Smart, A. Spagna, I. Steele, F. Taris, J. Torra, A. van Elteren, W. van Reeven, and A. Vecchiato.
Gaia Data Release 2. The astrometric solution.
Astron. Astrophys., 616:A2, August 2018a.
doi: 10.1051/0004-6361/201832727.

L. Lindegren, J. Hernandez, A. Bombrun, S. Klioner, U. Bastian, M. Ramos-Lerate, A. de Torres, H. Steidelmuller, C. Stephenson, D. Hobbs, U. Lammers, M. Biermann, R. Geyer, T. Hilger, D. Michalik, U. Stampa, P. J. McMillan, J. Castaneda, M. Clotet, G. Comoretto, M. Davidson, C. Fabricius, G. Gracia, N. C. Hambly, A. Hutton, A. Mora, J. Portell, F. van Leeuwen, U. Abbas, A. Abreu, M. Altmann, A. Andrei, E. Anglada, L. Balaguer-Nunez, C. Barache, U. Becciani, S. Bertone, L. Bianchi, S. Bouquillon, G. Bourda, T. Brusemeister, B. Bucciarelli, D. Busonero, R. Buzzi, R. Cancelliere, T. Carlucci, P. Charlot, N. Cheek, M. Crosta, C. Crowley, J. de Bruijne, F. de Felice, R. Drimmel, P. Esquej, A. Fienga, E. Fraile, M. Gai, N. Garralda, J. J. Gonzalez-Vidal, R. Guerra, M. Hauser, W. Hofmann, B. Holl, S. Jordan, M. G. Lattanzi, H. Lenhardt, S. Liao, E. Licata, T. Lister, W. Loffler, J. Marchant, J.-M. Martin-Fleitas, R. Messineo, F. Mignard, R. Morbidelli, E. Poggio, A. Riva, N. Rowell, E. Salguero, M. Sarasso, E. Sciacca, H. Siddiqui, R. L. Smart, A. Spagna, I. Steele, F. Taris, J. Torra, A. van Elteren, W. van Reeven, and A. Vecchiato.
Gaia Data Release 2: The astrometric solution.
ArXiv e-prints, April 2018b.

Lindegren, L., Lammers, U., Bastian, U., Hernández, J., Klioner, S., Hobbs, D., Bombrun, A., Michalik, D., and et al.
Gaia data release 1. astrometry: one billion positions, two million proper motions, and parallaxes.
Astron. Astrophys., 2016.
doi: 10.1051/0004-6361/201628714.
URL `http://dx.doi.org/10.1051/0004-6361/201628714`.

C. Liu, L.-C. Deng, J. L. Carlin, M. C. Smith, J. Li, H. J. Newberg, S. Gao, F. Yang, X.-X. Xue, Y. Xu, Y.-Y. Zhang, Y. Xin, Y. Wu, and G. Jin.
The K Giant Stars from the LAMOST Survey Data. I. Identification, Metallicity, and Distance.
Astrophys. J., 790:110, August 2014.
doi: 10.1088/0004-637X/790/2/110.

C. Liu, H.-J. Tian, and J.-C. Wan.
The age-kinematical features in the Milky Way outer disk.
In A. Gil de Paz, J. H. Knapen, and J. C. Lee, editors, *Formation and Evolution of Galaxy Outskirts*, volume 321 of *IAU Symposium*, pages 6–9, March 2017.
doi: 10.1017/S1743921316011029.

A. V. Loktin and G. V. Beshenov.
Luminosity calibration for OB stars from Hipparcos trigonometric parallaxes.
Astronomy Reports, 45:711–717, September 2001.
doi: 10.1134/1.1398920.

M. López-Corredoira, J. Betancort-Rijo, and J. E. Beckman.
Generation of galactic disc warps due to intergalactic accretion flows onto the disc.
Astron. Astrophys., 386:169–186, April 2002a.
doi: 10.1051/0004-6361:20020229.

M. López-Corredoira, A. Cabrera-Lavers, F. Garzón, and P. L. Hammersley.
Old stellar Galactic disc in near-plane regions according to 2MASS: Scales, cut-off, flare and warp.
Astron. Astrophys., 394:883–899, November 2002b.
doi: 10.1051/0004-6361:20021175.

M. López-Corredoira, A. Cabrera-Lavers, and O. E. Gerhard.
A boxy bulge in the Milky Way. Inversion of the stellar statistics equation with 2MASS data.
Astron. Astrophys., 439:107–110, August 2005.
doi: 10.1051/0004-6361:20053075.

M. López-Corredoira, H. Abedi, F. Garzón, and F. Figueras.
Vertical velocities from proper motions of red clump giants.
Astron. Astrophys., 572:A101, December 2014.
doi: 10.1051/0004-6361/201424573.

X. Luri, A.G.A. Brown, L. Sarro, F. Arenou, C.A.L. Bailer-Jones, A. Castro-Ginard, J. de Bruijne, T. Prusti, C. Babusiaux, and H.E. Delgado.
On the use of Gaia parallaxes.
Astron. Astrophys., 2018.

D. Lynden-Bell.
Free precession for the galaxy.
129:299, 1965.
doi: 10.1093/mnras/129.3.299.

David J. C. MacKay.
Information Theory, Inference, and Learning Algorithms.
2003.
ISBN 9780521642989.
URL http://www.inference.phy.cam.ac.uk/mackay/itila/.

J. Maíz Apellániz, A. Sota, N. R. Walborn, E. J. Alfaro, R. H. Barbá, N. I. Morrell, R. C. Gamen, and J. I. Arias.
The Galactic O-star spectroscopic survey (GOSSS).
In M. R. Zapatero Osorio, J. Gorgas, J. Maíz Apellániz, J. R. Pardo, and A. Gil de Paz, editors, *Highlights of Spanish Astrophysics VI*, pages 467–472, November 2011.

P. Marrese, S. Marinoni, M. Fabrizio, and G. Altavilla.
Gaia Data Release 2: Cross-match with external catalogues: algorithm and statistics.
Astron. Astrophys., April 2018.

D. J. Marshall, A. C. Robin, C. Reylé, M. Schultheis, and S. Picaud.
Modelling the Galactic interstellar extinction distribution in three dimensions.
Astron. Astrophys., 453:635–651, July 2006.
doi: 10.1051/0004-6361:20053842.

F. Martins and B. Plez.
UBVJHK synthetic photometry of Galactic O stars.
Astron. Astrophys., 457:637–644, October 2006.
doi: 10.1051/0004-6361:20065753.

F. Martins, D. Schaerer, and D.J. Hillier.
A new calibration of stellar parameters of galactic o stars.
Astron.Astrophys., 436:1049–1065, 2005.
URL http://arxiv.org/abs/astro-ph/0503346.

A. McWilliam and M. Zoccali.
Two Red Clumps and the X-shaped Milky Way Bulge.
Astrophys. J., 724:1491–1502, December 2010.
doi: 10.1088/0004-637X/724/2/1491.

D. Michalik, L. Lindegren, D. Hobbs, and U. Lammers.

Joint astrometric solution of HIPPARCOS and Gaia. A recipe for the Hundred Thousand Proper Motions project.
Astron. Astrophys., 571:A85, November 2014.
doi: 10.1051/0004-6361/201424606.

D. Michalik, L. Lindegren, and D. Hobbs.
The Tycho-Gaia astrometric solution . How to get 2.5 million parallaxes with less than one year of Gaia data.
Astron. Astrophys., 574:A115, February 2015.
doi: 10.1051/0004-6361/201425310.

M. Miyamoto, M. Yoshizawa, and S. Suzuki.
1988.

Y. Momany, S. Zaggia, G. Gilmore, G. Piotto, G. Carraro, L. R. Bedin, and F. de Angeli.
Outer structure of the Galactic warp and flare: explaining the Canis Major over-density.
Astron. Astrophys., 451:515–538, May 2006.
doi: 10.1051/0004-6361:20054081.

G. Monari, B. Famaey, and A. Siebert.
The vertical effects of disc non-axisymmetries from perturbation theory: the case of the Galactic bar.
452:747–754, September 2015.
doi: 10.1093/mnras/stv1206.

G. Monari, B. Famaey, A. Siebert, R. J. J. Grand, D. Kawata, and C. Boily.
The effects of bar-spiral coupling on stellar kinematics in the Galaxy.
461:3835–3846, October 2016.
doi: 10.1093/mnras/stw1564.

D. M. Nataf, A. Udalski, A. Gould, P. Fouqué, and K. Z. Stanek.
The Split Red Clump of the Galactic Bulge from OGLE-III.
Astrophys. J. Lett., 721:L28–L32, September 2010.
doi: 10.1088/2041-8205/721/1/L28.

J. F. Navarro, M. G. Abadi, K. A. Venn, K. C. Freeman, and B. Anguiano.
Through thick and thin: kinematic and chemical components in the solar neighbourhood.
412:1203–1209, April 2011.
doi: 10.1111/j.1365-2966.2010.17975.x.

R. W. Nelson and S. Tremaine.
The damping and excitation of galactic warps by dynamical friction.

275:897–920, August 1995.
doi: 10.1093/mnras/275.4.897.

M. Ness, K. Freeman, E. Athanassoula, E. Wylie-De-Boer, J. Bland-Hawthorn, G. F. Lewis, D. Yong, M. Asplund, R. R. Lane, L. L. Kiss, and R. Ibata.
The Origin of the Split Red Clump in the Galactic Bulge of the Milky Way.
Astrophys. J., 756:22, September 2012.
doi: 10.1088/0004-637X/756/1/22.

J. E. O'Donnell.
R_{nu}-dependent optical and near-ultraviolet extinction.
Astrophys. J., 422:158–163, February 1994.
doi: 10.1086/173713.

J. H. Oort, F. J. Kerr, and G. Westerhout.
The galactic system as a spiral nebula (Council Note).
118:379, 1958.
doi: 10.1093/mnras/118.4.379.

S. Ortolani, A. Renzini, R. Gilmozzi, G. Marconi, B. Barbuy, E. Bica, and R. M. Rich.
Near-coeval formation of the Galactic bulge and halo inferred from globular cluster ages.
Nature, 377:701–704, October 1995.
doi: 10.1038/377701a0.

E. C. Ostriker and J. J. Binney.
Warped and tilted galactic discs.
237:785–798, April 1989.
doi: 10.1093/mnras/237.3.785.

J. A. Peacock.
Two-dimensional goodness-of-fit testing in astronomy.
202:615–627, February 1983.
doi: 10.1093/mnras/202.3.615.

E. Poggio, R. Drimmel, R. L. Smart, A. Spagna, and M. G. Lattanzi.
The kinematic signature of the Galactic warp in Gaia DR1. I. The Hipparcos subsample.
Astron. Astrophys., 601:A115, May 2017.
doi: 10.1051/0004-6361/201629916.

E. Poggio, R. Drimmel, M. G. Lattanzi, R. L. Smart, A. Spagna, R. Andrae, C. A. L. Bailer-Jones, M. Fouesneau, T. Antoja, C. Babusiaux, D. W. Evans, F. Figueras, D. Katz, C. Reylé, A. C. Robin, M. Romero-Gómez, and G. M. Seabroke.

The Galactic warp revealed by Gaia DR2 kinematics.
481:L21–L25, November 2018a.
doi: 10.1093/mnrasl/sly148.

E. Poggio, R. Drimmel, R. L. Smart, A. Spagna, and M. G. Lattanzi.
Search for Galactic warp signal in Gaia DR1 proper motions.
In A. Recio-Blanco, P. de Laverny, A. G. A. Brown, and T. Prusti, editors, *Astrometry and Astrophysics in the Gaia Sky*, volume 330 of *IAU Symposium*, pages 185–188, April 2018b.
doi: 10.1017/S1743921317006032.

C. W. Purcell, J. S. Bullock, and S. Kazantzidis.
Heated disc stars in the stellar halo.
404:1711–1718, June 2010.
doi: 10.1111/j.1365-2966.2010.16429.x.

B. C. Reed.
Luminosity Function of Solar-Neighborhood OB Stars.
Publ. Astron. Soc. Pac., 113:537–542, May 2001.
doi: 10.1086/320286.

M. J. Reid.
Micro-arcsecond astrometry with the VLBA.
In W. J. Jin, I. Platais, and M. A. C. Perryman, editors, *A Giant Step: from Milli- to Micro-arcsecond Astrometry*, volume 248 of *IAU Symposium*, pages 141–147, July 2008.
doi: 10.1017/S1743921308018929.

M. J. Reid and A. Brunthaler.
The Proper Motion of Sagittarius A*. II. The Mass of Sagittarius A*.
Astrophys. J., 616:872–884, December 2004.
doi: 10.1086/424960.

M. J. Reid, K. M. Menten, A. Brunthaler, X. W. Zheng, T. M. Dame, Y. Xu, Y. Wu, B. Zhang, A. Sanna, M. Sato, K. Hachisuka, Y. K. Choi, K. Immer, L. Moscadelli, K. L. J. Rygl, and A. Bartkiewicz.
Trigonometric Parallaxes of High Mass Star Forming Regions: The Structure and Kinematics of the Milky Way.
Astrophys. J., 783:130, March 2014.
doi: 10.1088/0004-637X/783/2/130.

V. Reshetnikov and F. Combes.
Statistics of optical WARPS in spiral disks.
Astron. Astrophys., 337:9–16, September 1998.

C. Reylé, D. J. Marshall, A. C. Robin, and M. Schultheis.
The Milky Way's external disc constrained by 2MASS star counts.
Astron. Astrophys., 495:819–826, March 2009.
doi: 10.1051/0004-6361/200811341.

A. C. Robin, C. Reylé, and D. J. Marshall.
The Galactic warp as seen from 2MASS survey.
Astronomische Nachrichten, 329:1012, December 2008.
doi: 10.1002/asna.200811084.

H. J. Rocha-Pinto, S. R. Majewski, M. F. Skrutskie, and J. D. Crane.
Tracing the Galactic Anticenter Stellar Stream with 2MASS M Giants.
Astrophys. J. Lett., 594:L115–L118, September 2003.
doi: 10.1086/378668.

A. Rojas-Arriagada, A. Recio-Blanco, P. de Laverny, Š. Mikolaitis, F. Matteucci, E. Spitoni, M. Schultheis, M. Hayden, V. Hill, M. Zoccali, D. Minniti, O. A. Gonzalez, G. Gilmore, S. Randich, S. Feltzing, E. J. Alfaro, C. Babusiaux, T. Bensby, A. Bragaglia, E. Flaccomio, S. E. Koposov, E. Pancino, A. Bayo, G. Carraro, A. R. Casey, M. T. Costado, F. Damiani, P. Donati, E. Franciosini, A. Hourihane, P. Jofré, C. Lardo, J. Lewis, K. Lind, L. Magrini, L. Morbidelli, G. G. Sacco, C. C. Worley, and S. Zaggia.
The Gaia-ESO Survey: Exploring the complex nature and origins of the Galactic bulge populations.
Astron. Astrophys., 601:A140, May 2017.
doi: 10.1051/0004-6361/201629160.

M. Samland and O. E. Gerhard.
The formation of a disk galaxy within a growing dark halo.
Astron. Astrophys., 399:961–982, March 2003.
doi: 10.1051/0004-6361:20021842.

M. L. Sanchez-Saavedra, E. Battaner, and E. Florido.
Frequency of Warped Spiral Galaxies at Visible Wavelengths.
246:458, October 1990.

P. Sartoretti, D. Katz, M. Cropper, P. Panuzzo, G. M. Seabroke, Y. Viala, K. Benson, R. Blomme, G. Jasniewicz, A. Jean-Antoine, H. Huckle, M. Smith, S. Baker, F. Crifo, Y. Damerdji, M. David, C. Dolding, Y. Frémat, E. Gosset, A. Guerrier, L. P. Guy, R. Haigron, K. Janßen, O. Marchal, G. Plum, C. Soubiran, F. Thévenin, M. Ajaj, C. Allende Prieto, C. Babusiaux, S. Boudreault, L. Chemin, C. Delle Luche, C. Fabre, A. Gueguen, N. C. Hambly, Y. Lasne, F. Meynadier, F. Pailler, C. Panem, F. Riclet, F. Royer, G. Tauran, C. Zurbach, T. Zwitter, F. Arenou, A. Gomez, V. Lemaitre, N. Leclerc, T. Morel, U. Munari, C. Turon, and M. Žerjal.

Gaia Data Release 2. Processing the spectroscopic data.
Astron. Astrophys., 616:A6, August 2018.
doi: 10.1051/0004-6361/201832836.

J. M. Scalo.
The stellar initial mass function.
11:1–278, May 1986.

Aller L. H. Appenzeller I. et al. Schmidt-Kaler, T.
Landolt-Börnstein: Numerical Data and Functional Relationships in Science and Technology – New Series, Group VI: Astronomy and Astrophysics.
1982.

R. Schödel, A. Feldmeier, D. Kunneriath, S. Stolovy, N. Neumayer, P. Amaro-Seoane, and S. Nishiyama.
Surface brightness profile of the Milky Way's nuclear star cluster.
Astron. Astrophys., 566:A47, June 2014.
doi: 10.1051/0004-6361/201423481.

R. Schönrich and M. Aumer.
Assessing distances and consistency of kinematics in Gaia/TGAS.
472:3979–3998, December 2017.
doi: 10.1093/mnras/stx2189.

R. Schönrich and W. Dehnen.
Warp, waves, and wrinkles in the Milky Way.
478:3809–3824, August 2018.
doi: 10.1093/mnras/sty1256.

R. Schönrich, J. Binney, and W. Dehnen.
Local kinematics and the local standard of rest.
403:1829–1833, April 2010.
doi: 10.1111/j.1365-2966.2010.16253.x.

G. M. Seabroke and G. Gilmore.
Revisiting the relations: Galactic thin disc age-velocity dispersion relation.
380:1348–1368, October 2007.
doi: 10.1111/j.1365-2966.2007.12210.x.

L. Searle and R. Zinn.
Compositions of halo clusters and the formation of the galactic halo.
Astrophys. J., 225:357–379, October 1978.
doi: 10.1086/156499.

J. A. Sellwood.
Dynamics of Disks and Warps, page 923.
2013.
doi: 10.1007/978-94-007-5612-0_18.

B. A. Skiff.
VizieR Online Data Catalog: Catalogue of Stellar Spectral Classifications (Skiff, 2009-2014).
VizieR Online Data Catalog, 1, October 2014.

M. F. Skrutskie, S. E. Schneider, R. Stiening, S. E. Strom, M. D. Weinberg, C. Beichman, T. Chester, R. Cutri, C. Lonsdale, J. Elias, R. Elston, R. Capps, J. Carpenter, J. Huchra, J. Liebert, D. Monet, S. Price, and P. Seitzer.
The Two Micron All Sky Survey (2MASS): Overview and Status.
In F. Garzon, N. Epchtein, A. Omont, B. Burton, and P. Persi, editors, *The Impact of Large Scale Near-IR Sky Surveys*, volume 210 of *Astrophysics and Space Science Library*, page 25, 1997.
doi: 10.1007/978-94-011-5784-1_4.

M. F. Skrutskie, R. M. Cutri, R. Stiening, M. D. Weinberg, S. Schneider, J. M. Carpenter, C. Beichman, R. Capps, T. Chester, J. Elias, J. Huchra, J. Liebert, C. Lonsdale, D. G. Monet, S. Price, P. Seitzer, T. Jarrett, J. D. Kirkpatrick, J. E. Gizis, E. Howard, T. Evans, J. Fowler, L. Fullmer, R. Hurt, R. Light, E. L. Kopan, K. A. Marsh, H. L. McCallon, R. Tam, S. Van Dyk, and S. Wheelock.
The Two Micron All Sky Survey (2MASS).
Astron. J., 131:1163–1183, February 2006.
doi: 10.1086/498708.

R. L. Smart, R. Drimmel, and M. G. Lattanzi.
Using HIPPARCOS to Study the Warp of our Galaxy.
In *IAU Joint Discussion*, volume 14 of *IAU Joint Discussion*, page 46, 1997.

R. L. Smart, R. Drimmel, M. G. Lattanzi, and J. J. Binney.
Unexpected stellar velocity distribution in the warped Galactic disk.
Nature, 392:471–473, April 1998.
doi: 10.1038/33096.

A. Sota, J. Maíz Apellániz, N. R. Walborn, E. J. Alfaro, R. H. Barbá, N. I. Morrell, R. C. Gamen, and J. I. Arias.
The Galactic O-Star Spectroscopic Survey. I. Classification System and Bright Northern Stars in the Blue-violet at R ˜ 2500.
Astrophys. Space Science, 193:24, apr 2011.
doi: 10.1088/0067-0049/193/2/24.

A. Sota, J. Maíz Apellániz, N. I. Morrell, R. H. Barbá, N. R. Walborn, R. C. Gamen, J. I. Arias, and E. J. Alfaro.
The Galactic O-Star Spectroscopic Survey (GOSSS). II. Bright Southern Stars.
Astrophys. Space Science, 211:10, mar 2014.
doi: 10.1088/0067-0049/211/1/10.

C. Soubiran, O. Bienaymé, and A. Siebert.
Vertical distribution of Galactic disk stars. I. Kinematics and metallicity.
Astron. Astrophys., 398:141–151, January 2003.
doi: 10.1051/0004-6361:20021615.

L. S. Sparke and S. Casertano.
A model for persistent galactic WARPS.
234:873–898, October 1988.
doi: 10.1093/mnras/234.4.873.

L. S. Sparke and J. S. Gallagher, III.
Galaxies in the Universe - 2nd Edition.
April 2006.
doi: 10.2277/0521855934.

K. Z. Stanek, A. Udalski, M. SzymaŃski, J. KaŁuŻny, Z. M. Kubiak, M. Mateo, and W. KrzemiŃski.
Modeling the Galactic Bar Using Red Clump Giants.
Astrophys. J., 477:163–175, March 1997.
doi: 10.1086/303702.

V. Straižys.
Multicolor stellar photometry.
1992.

V. Straizys and G. Kuriliene.
doi: 10.1007/BF00652936.

J. Tang, A. Bressan, P. Rosenfield, A. Slemer, P. Marigo, L. Girardi, and L. Bianchi.
New PARSEC evolutionary tracks of massive stars at low metallicity: testing canonical stellar evolution in nearby star-forming dwarf galaxies.
445:4287–4305, December 2014.
doi: 10.1093/mnras/stu2029.

J. H. Taylor and J. M. Cordes.
Pulsar distances and the galactic distribution of free electrons.

Astrophys. J., 411:674–684, July 1993.
doi: 10.1086/172870.

W. D. Vacca, C. D. Garmany, and J. M. Shull.
The Lyman-Continuum Fluxes and Stellar Parameters of O and Early B-Type Stars.
Astrophys. J., 460:914, April 1996.
doi: 10.1086/177020.

E. Valenti, M. Zoccali, O. A. Gonzalez, D. Minniti, J. Alonso-García, E. Marchetti, M. Hempel, A. Renzini, and M. Rejkuba.
Stellar density profile and mass of the Milky Way bulge from VVV data.
Astron. Astrophys., 587:L6, March 2016.
doi: 10.1051/0004-6361/201527500.

F. van Leeuwen.
VizieR Online Data Catalog: Hipparcos, the New Reduction (van Leeuwen, 2007).
VizieR Online Data Catalog, 1311, September 2008.

Á. Villalobos and A. Helmi.
Simulations of minor mergers - I. General properties of thick discs.
391:1806–1827, December 2008.
doi: 10.1111/j.1365-2966.2008.13979.x.

N. R. Walborn, H. Sana, S. Simón-Díaz, J. Maíz Apellániz, W. D. Taylor, C. J. Evans, N. Markova, D. J. Lennon, and A. de Koter.
The VLT-FLAMES Tarantula Survey. XIV. The O-type stellar content of 30 Doradus.
Astron. Astrophys., 564:A40, April 2014.
doi: 10.1051/0004-6361/201323082.

L. L. Watkins, N. W. Evans, V. Belokurov, M. C. Smith, P. C. Hewett, D. M. Bramich, G. F. Gilmore, M. J. Irwin, S. Vidrih, Ł. Wyrzykowski, and D. B. Zucker.
Substructure revealed by RRLyraes in SDSS Stripe 82.
398:1757–1770, October 2009.
doi: 10.1111/j.1365-2966.2009.15242.x.

C. Wegg, O. Gerhard, and M. Portail.
The structure of the Milky Way's bar outside the bulge.
450:4050–4069, July 2015.
doi: 10.1093/mnras/stv745.

W. Wegner.
Absolute magnitudes of OB and Be stars based on Hipparcos parallaxes - II.

371:185–192, September 2006.
doi: 10.1111/j.1365-2966.2006.10549.x.

J. L. Weiland, R. G. Arendt, G. B. Berriman, E. Dwek, H. T. Freudenreich, M. G. Hauser, T. Kelsall, C. M. Lisse, M. Mitra, S. H. Moseley, N. P. Odegard, R. F. Silverberg, T. J. Sodroski, W. J. Spiesman, and S. W. Stemwedel.
COBE diffuse infrared background experiment observations of the galactic bulge.
Astrophys. J. Lett., 425:L81–L84, April 1994.
doi: 10.1086/187315.

M. D. Weinberg and L. Blitz.
A Magellanic Origin for the Warp of the Galaxy.
Astrophys. J. Lett., 641:L33–L36, April 2006.
doi: 10.1086/503607.

G. Westerhout.
The distribution of atomic hydrogen in the outer parts of the Galactic System.
13:201, May 1957.

L. M. Widrow, S. Gardner, B. Yanny, S. Dodelson, and H.-Y. Chen.
Galactoseismology: Discovery of Vertical Waves in the Galactic Disk.
Astrophys. J. Lett., 750:L41, May 2012.
doi: 10.1088/2041-8205/750/2/L41.

L. M. Widrow, J. Barber, M. H. Chequers, and E. Cheng.
Bending and breathing modes of the Galactic disc.
440:1971–1981, May 2014.
doi: 10.1093/mnras/stu396.

M. E. K. Williams, M. Steinmetz, J. Binney, A. Siebert, H. Enke, B. Famaey, I. Minchev, R. S. de Jong, C. Boeche, K. C. Freeman, O. Bienaymé, J. Bland-Hawthorn, B. K. Gibson, G. F. Gilmore, E. K. Grebel, A. Helmi, G. Kordopatis, U. Munari, J. F. Navarro, Q. A. Parker, W. Reid, G. M. Seabroke, S. Sharma, A. Siviero, F. G. Watson, R. F. G. Wyse, and T. Zwitter.
The wobbly Galaxy: kinematics north and south with RAVE red-clump giants.
436:101–121, November 2013.
doi: 10.1093/mnras/stt1522.

C. O. Wright, M. P. Egan, K. E. Kraemer, and S. D. Price.
The Tycho-2 Spectral Type Catalog.
Astron. J., 125:359–363, January 2003.
doi: 10.1086/345511.

R. F. G. Wyse.
The Merging History of the Milky Way Disk.
In J. G. Funes and E. M. Corsini, editors, *Galaxy Disks and Disk Galaxies*, volume 230 of *Astronomical Society of the Pacific Conference Series*, pages 71–80, 2001.

R. F. G. Wyse, G. Gilmore, and M. Franx.
Galactic Bulges.
35:637–675, 1997.
doi: 10.1146/annurev.astro.35.1.637.

R. F. G. Wyse, G. Gilmore, J. E. Norris, M. I. Wilkinson, J. T. Kleyna, A. Koch, N. W. Evans, and E. K. Grebel.
Further Evidence of a Merger Origin for the Thick Disk: Galactic Stars along Lines of Sight to Dwarf Spheroidal Galaxies.
Astrophys. J. Lett., 639:L13–L16, March 2006.
doi: 10.1086/501228.

Y. Xu, H. J. Newberg, J. L. Carlin, C. Liu, L. Deng, J. Li, R. Schönrich, and B. Yanny.
Rings and Radial Waves in the Disk of the Milky Way.
Astrophys. J., 801:105, March 2015.
doi: 10.1088/0004-637X/801/2/105.

Y. Yoshii.
1982.

I. Yusifov.
Pulsars and the Warp of the Galaxy.
In B. Uyaniker, W. Reich, and R. Wielebinski, editors, *The Magnetized Interstellar Medium*, pages 165–169, February 2004.

G. Zhao, Y.-H. Zhao, Y.-Q. Chu, Y.-P. Jing, and L.-C. Deng.
Research in Astronomy and Astrophysics, 12:723–734, jul 2012.
doi: 10.1088/1674-4527/12/7/002.

PUBLICATIONS BY ELOISA POGGIO

- **E. Poggio**, R. Drimmel, M. G. Lattanzi, R. L. Smart, A. Spagna, R. Andrae, C. A. L. Bailer-Jones, M. Fouesneau, T. Antoja, C. Babusiaux, D. W. Evans, F. Figueras, D. Katz, C. Reylé, A. C. Robin, M. Romero-Gómez, G. M. Seabroke, The Galactic warp revealed by *Gaia* DR2 kinematics, (2018), *MNRAS*, 481, L21P. *Note*: Chapter 9 of this PhD Thesis is based on this publication.

- T. Antoja, A. Helmi, M. Romero-Gómez, D. Katz, C. Babusiaux, R. Drimmel, D. W. Evans, F. Figueras, **E. Poggio**, C. Reylé, A.C. Robin, G. Seabroke, and C. Soubiran, A dynamically young and perturbed Milky Way disk, (2018), *Nature*, 561, 360

- Gaia Collaboration, D. Katz, T. Antoja, M. Romero-Gómez, R. Drimmel, C. Reylé, G. M. Seabroke, C. Soubiran, C. Babusiaux, P. Di Matteo, F. Figueras, **E. Poggio**, A. C. Robin, D. W. Evans, and 440 co-authors, Gaia Data Release 2: Mapping the Milky Way disc kinematics, (2018), *A&A*, 616, A11. *Note*: Chapter 8 of this PhD Thesis is based on E. Poggio's contribution to this publication.

- L. Lindegren, J. Hern·ndez, A. Bombrun, S. Klioner, U. Bastian, and 85 co-authors (incl. **E. Poggio**), Gaia Data Release 2: The astrometric solution, (2018), *A&A*, 616, A2

- Gaia Collaboration, A. G. A. Brown, A. Vallenari, T. Prusti, and 450 co-authors (incl. **E. Poggio**), Gaia Data Release 2: Summary of the contents and survey properties, (2018), *A&A*, 616, A1

- Gaia Collaboration, C. Babusiaux, F. van Leeuwen, M.A. Barstow, and 449 co-authors (incl. **E. Poggio**), Gaia Data Release 2: Observational Herzsprung-Russel diagrams, (2018), *A&A*, 616, A10

- Gaia Collaboration, A. Helmi, F. van Leeuwen, P.J. McMillan, and 450 co-authors (incl. **E. Poggio**), Gaia Data Release 2: Kinematics of globular clusters and dwarf galaxies around the Milky Way, (2018), *A&A*, 616, A12

- Gaia Collaboration, L. Eyer, L. Rimoldini, M. Audard, R.I. Anderson, and 449 co-authors (incl. **E. Poggio**), Gaia Data Release 2: Variable stars in the colour-absolute magnitude diagram, (2018), *A&A*

- Gaia Collaboration, F. Mignard, S. A. Klioner, L. Lindegren, and 449 co-authors (incl. **E. Poggio**), Gaia Data Release 2: The Celestial reference frame (Gaia-CRF2), (2018), *A&A*, 616, A14

- Gaia Collaboration, F. Spoto, P. Tanga, F. Mignard, J. Berthier, and 450 co-authors (incl. **E. Poggio**), Gaia Data Release 2: Observations of solar system objects, (2018), *A&A*, 616, A13

- **E. Poggio**, R. Drimmel, R. L. Smart, A. Spagna, M. G. Lattanzi, The kinematic signature of the Galactic warp in Gaia DR1. - I. The Hipparcos subsample, (2017), *A&A*, 601, A115. *Note*: Chapter 2, 3 and 4 of this PhD Thesis are partly based on this publication.

Conference proceeding

- **E. Poggio**, R. Drimmel, R. L. Smart, A. Spagna, M. G. Lattanzi, Search for Galactic warp signal in Gaia DR1 proper motions, (2018), *Proceedings of IAU Symposium 330: "Astrometry and Astrophysics in the Gaia sky"*, 330, 185

List of Tables

TABLE **Page**

List of Figures